CHIRAL HALIDE PEROVSKITE FOR MULTIMODAL CHIROPTOELECTRONICS

LIU QI

PhD
The Hong Kong Polytechnic University
2025

The Hong Kong Polytechnic University
Department of Applied Physics

Chiral Halide Perovskite for Multimodal Chiroptoelectronics

LIU Qi

A thesis submitted in partial fulfilment of the requirements for the degree of Doctor of Philosophy

June 2025

CERTIFICATE OF ORIGINALITY

I hereby declare that this thesis is my original work, and that, to the best of my knowledge and belief, it does not contain any previously published or written material, nor material that has been accepted for the attainment of any other degree or diploma, except for instances where proper acknowledgement has been provided within the text.

____________________ (Signed)

LIU Qi (Name of student)

Abstract

Chirality refers to an intrinsic geometric property of an object that possesses non-superimposable mirror-image forms. Notably, chirality gives rise to a spectrum of unique photophysical phenomena, including nonlinear optical responses, chiral-induced spin selectivity, circular dichroism (CD), circularly polarized photoluminescence (PL), and spin-polarized exciton dynamics. The synergistic integration of chirality into halide perovskite yields chiral halide perovskites (CHPs), which manifest enhanced chiroptical-electronic properties by combining the spin-selective transport characteristics of chiral systems with the exceptional optoelectronic performance inherent to halide perovskites. In this thesis, CHPs with different morphologies (e.g., film, nanowire, and quantum well structure) are employed as functional layers to develop high-performance chiroptoelectronics, such as circularly polarized light (CPL) PAS and spin devices.

Firstly, a heterostructure device composed of helical 1D chiral perovskite (H-PVK) and single-wall carbon nanotubes (SWNTs) is presented for circular polarization sensing PAS. The device exhibits excellent polarization sensitivity and photoresponsivity, which could be attributed to the strong light-matter interactions between H-PVK and SWNTs. With the aid of femtosecond pump-probe spectroscopy, we demonstrated the trapping of electrons in H-PVK and the effective collection of holes in the SWNTs. Such carrier dynamics contribute to a series of bioinspired circular polarization-sensitive neuromorphic behaviors including polarization-perceptual excitatory postsynaptic current, paired-pulse facilitation, and learning-forgetting-memory process. In application, a 7 × 7 device array is developed to show the potential application of the PAS in constructing an anti-glare neuromorphic vision system. It is shown that the perception and memory of the circular polarization states can be easily realized through modulating CPL with different spatiotemporal information. More importantly, PAS-based spike neural networks are simulated, and show a high recognition accuracy up to 90% under the advanced encoding way of PAS. The proposed PAS indicates a significant breakthrough toward the next-generation intelligent visual perception systems.

Secondly, we propose a chiral perovskite nanowire-based heterostructure to achieve linear and circular polarization sensitive all-in-one PAS device. The designed PAS device exhibits high CD (400 mdeg) from chiral materials and intrinsic linear dichroism from nanowire morphology, enabling the full-Stokes detection. The PAS exhibits a longer carrier lifetime owing to efficient hole transfer from perovskite nanowire to MXene, which is demonstrated by TA, thereby contributing to a high responsivity (2.2 AW^{-1}) and excellent synaptic behavior (i.e., short-term plasticity, long-term potentiation). More importantly, the PAS device-based reservoir computing is performed and exhibits good prediction (NRMSE = 0.023) in the chaotic system forecasting task. This work provides an innovative design for achieving all-in-one neuromorphic sensing functions of linear and circular polarization, paving the way for the development of advanced visual systems that are capable of polarization-dependent perception.

Thirdly, the quantum well structured CHP superlattice is synthesized and transferred to different substrates for study. Utilizing the micro-area absorption measurement equipment, an ultra-high CD value (>4000 mdeg) is demonstrated. The edge state of the superlattice structure that extremely enlarges the vertical carrier transport ability of the CHP is verified by the PL mapping. Moreover, an obvious current difference is observed between the vertical and planar direction, supporting the vertical transport preference. High spin polarization degree up to 90% is measured by the magnetic conductive atomic force microscope, which underlies the foundation for high-performance spintronics. This work designs a high-quality quantum well-structured CHP superlattice, paving the way for high-density spin memory and spin logic devices.

In summary, this thesis supplies systematic exploration on CHPs for CPL-resolved PAS and spintronic devices, and extends the applicability of CHPs, demonstrating the potential of CHPs for next-generation chiroptoelectronics.

List of Publications

1. **Q. Liu**, P. Wang, Q. Wei, L. Zhou, H. Ren, C. Wang, J. Peng, L. Zhao, M. Li* "Chiral perovskite nanowire optoelectronic synapse for full-stokes polarization-resolved perception and reservoir computing", *Advanced Functional Materials*, 2415551 (2024).
2. **Q. Liu**, Q. Wei, H. Ren, L. Zhou, Y. Zhou, P. Wang, C. Wang, J. Yin, M. Li*, "Circular polarization-resolved ultraviolet photonic artificial synapse based on chiral perovskite", *Nature Communication*, 14, 7179 (2023).
3. **Q. Liu**, H. Ren, Q. Wei, M. Li*, "Chiral Halide Perovskites: Advancing Chiroptical Materials, Chiral-Optoelectronics, and Spintronic Applications", *Advanced Science*, e09155 (2025).
4. C. Wang, Q. Wei, H. Ren, K. L. Wong, **Q. Liu**, L. Zhou, P. Wang, S. Cai, J. Yin, M. Li*, "Efficient gate-tunable hot-carrier photocurrent from perovskite multiple quantum wells", *Advanced Materials*, 2413839 (2024).
5. Q. Wei, H. Ren, J. Liu, **Q. Liu**, C. Wang, T. W. Lau, L. Zhou, T. Bian, Y. Zhou, P. Wang, Q. Lei, M. Li*, "Long-lived hot carriers in two-dimensional perovskites: The role of alternating cations in interlayer space", *ACS Energy Letters*, 8, 4315 (2023).
6. C. Wang, J. Fu, Q. Wei, H. Ren, **Q. Liu**, L. Zhou, P. Wang, M. Li*, "Electric-field-enhanced electroluminescence color tuning of colloidal type-II tetrapods", *Nano Letters*, 23, 5705-5712 (2023).

Acknowledgements

The three-year PhD study at the Hong Kong Polytechnic University is an unforgettable experience in my study career. I enjoy the scientific research under the supervision of Prof. Li Mingjie at the Department of Applied Physics. After finishing this thesis, I would like to express my gratitude to many people who accompanied me during my PhD life.

First, I would like to express my sincere thanks to my supervisor Prof. Li Mingjie, who gave me an offer in 2022. Later in 2023, I was admitted as a PhD student and had the opportunity to study at the Hong Kong Polytechnic University. In the initial semester, I was not familiar with the photo-physical research, and Prof. Li gave me unwavering assistance whenever I encountered difficulties, which supported me in the field of optoelectronic devices. Prof. Li exemplifies commendable academic rigor through his steadfast dedication to scholarly excellence, consistently inspiring students to pioneer novel research frontiers while providing responsive, constructive guidance for students to overcome challenges encountered during investigative processes. Moreover, his dedication and passion inspired me and provided me with valuable insights into further research. I will always keep Prof. Li' instructions and suggestions in my mind.

Then, I would like to express my sincere appreciation to my co-supervisor, Prof. Siu Fung YU. I am grateful for his valuable advice. Prof. Yu's insights and encouragement served an important role in strengthening my determination throughout my study.

I would like to express my heartfelt gratitude to my group members and friends at the Hong Kong Polytechnic University, including Dr. Wei Qi, Dr. Wang Pengzhi, Mr. Dong Xuezhe, Mr. Zhou Luwei, Dr. Ren Hui, Dr. Zhang Xiang, Dr. Kang Chengbin, Mr. Chen Tianren, and Mr. Zhu Xuanyu for their unwavering support and collaboration throughout this endeavor.

At last, I would like to show my deepest gratitude to my parents and family for their firm support. They always stood by my side and respected my choice, which cultivates my independent thinking ability and self-discipline character. Meanwhile, I am deeply grateful to my wife-to-be Zhang Xiuqi, for her long-term steadfast companionship and trust, which extremely encouraged me during the challenging times. I am forever grateful for their love and encouragement.

Table of Contents

List of Figures

Chapter 1 Introduction

1.1 Background

Chirality derived from the Greek word “cheir” describes the property of an object that lacks geometric symmetry with its mirror image and cannot be superimposed onto its mirror counterpart through any combination of symmetry operations (e.g. translation, rotation), and is categorized into two distinct forms: left-handedness and right-handedness. A chiral object features mutually opposite configurations to its mirror image. As shown in **Figure 1.1**, this phenomenon is ubiquitously observed across natural and artificial materials, spanning scales from macroscopic systems (e.g., galactic spiral arms, and planetary rotation) to microscopic entities (e.g., amino acids, DNA, organic polymers, nanomaterials and metasurface). Particularly, chirality induces a series of fascinating photophysical activities containing nonlinear optics, chiral-induced spin selectivity (CISS), circular dichroism (CD), and circularly polarized luminescence, showing profound implications in material science and applied physics.

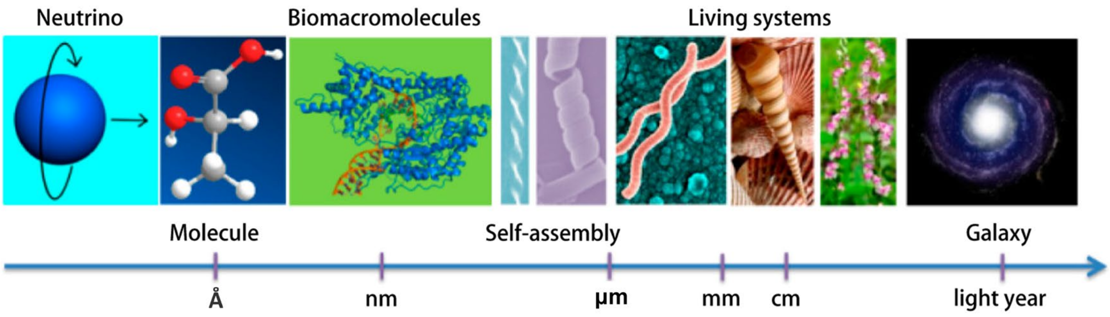

Figure 1.1 Chirality at various scales existing in nature.[1]

In the past decade, halide perovskites in different dimensionalities (crystal structure or morphology definition) were widely studied due to their high absorbance, small exciton binding energy, low trap density, long carrier diffusion lengths and high carrier mobility. In terms of those advantages, halide perovskite exhibits superior performance in different fields such as light-emitting diodes (LEDs), solar cells, photodetector (PD), lasers and photonic artificial synapse (PAS). However, the naturally centrosymmetric crystal structure of halide perovskite without chirality cannot be applied into chiroptical activities.

The incorporation of chiral ligands into halide perovskite breaks the symmetric arrangement of centric perovskite crystal and induces the chirality transfer, contributing to the chiral perovskites that inherit the properties from both chiral molecule and perovskite. Chiral halide perovskites (CHPs) exhibit intriguing optical characteristics, such as CD, Second-Harmonic Generation (SHG), spin-polarized exciton, circularly polarized luminescence, optical Stark effect, and electric properties such as CISS and spin-orbit coupling (SOC), ferroelectricity. The abovementioned features endow CHPs to be candidates for chiroptoelectronics applied in multiple fields including CPL sensing detectors, circularly polarized LEDs, lasers and spintronics. However, the CHPs show poor conductive capability due to the introduction of insulated chiral ligands, which discounts their performance in optoelectronics. It is necessary to improve the carrier transport inside the CHPs by different optimization strategies. As the rapid growth of chiroptoelectronics is posing new demands for the performance and functionality of electronics, CHPs-based devices with innovative behaviors are expected for state-of-the-art applications, which is the other motivation of this thesis.

1.2 Objectives of Research

Recently, chiral perovskite materials have attracted great attention owing to their significant chiroptical properties. Through careful and rigorous investigation, it is found that the number of papers related to chiral perovskite has been increasing rapidly in the past few years (since 2020), which is depicted in **Figure 1.2**. The CD characteristic endows CHPs with CPL distinguishability, which is widely utilized in constructing CPL detectors. The CISS of CHPs enables the spin filter without an external magnetic field, which provides an innovative way for constructing spintronics. However, recent extensive studies are mainly focusing on CHPs-based devices with simple and monotone structures, which hinders the development of diverse electronics. The aim of this project is to explore CHPs with different structure configurations in building high-performance and multifunctional chiroptoelectronics.

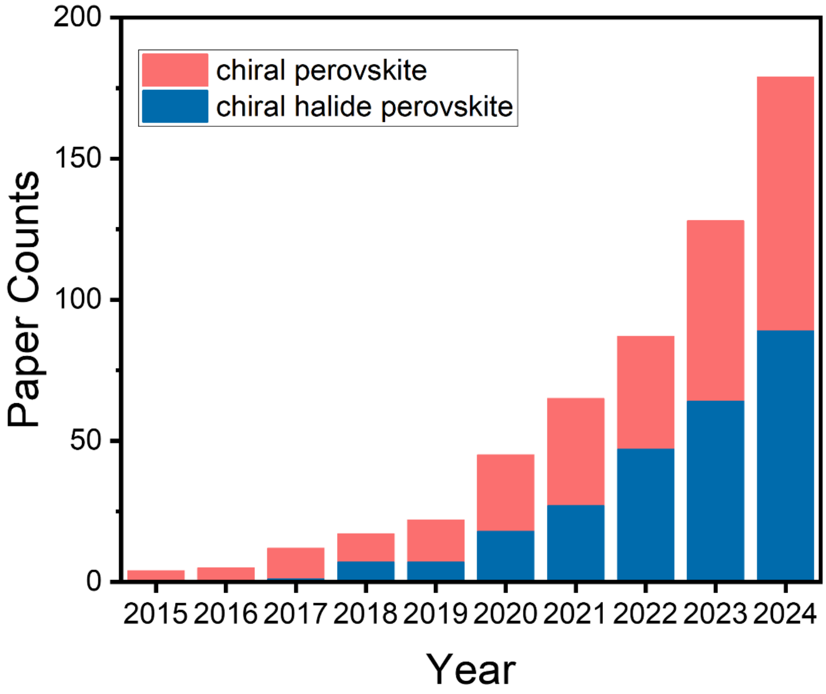

Figure 1.2 Statistical analysis of published papers in relation to chiral perovskites. (The data was collected on Web of Science with the keywords of “chiral perovskite” or “chiral halide perovskite”).

The structure design of CHPs-based devices can be manipulated by the introduction of other layers. For example, heterostructure forms when two functional layers contact, and shows superior behavior in carrier separation and transport. Also, various structures can be achieved via the direct control of CHPs' growth. Nanostructured CHPs exhibit intriguing properties due to the increased surface-to-volume ratio and strong quantum effect. Those methods show obvious optimization for CHPs-based devices.

The thesis explores the application of CHPs-based devices with various structures for CPL-resolved PAS and spin devices. (1) PAS is the basic device of neuromorphic computing and is advantageous in constructing neuromorphic systems owing to its parallel information processing ability, event-driven feature and low-power consumption. Current PAS devices are confined to monotone modulation of light intensity or wavelength but are not capable of responding to polarization containing high-dimensional information. CPL-resolved PAS inherits the rapid-response and energy-efficient features and could be modulated by the circular polarization, which enlarges the applicability of CHPs in complex vision perception systems. Since the CHPs could spontaneously respond to CPL without the optical equipment (e.g., linear polarizer, and quarter-wave plate), the CPL-resolved PAS devices extremely scale down the feature size and show great potential in constructing high-density chiroptoelectronics. (2) In CHPs, the spin orientation of electrons becomes coupled to molecular helicity during transport processes, leading to preferential transmission of electrons with specific spin states (left- or right-handed) and the generation of spin-polarized currents. This phenomenon originates from SOC, which is significantly amplified by the structural asymmetry inherent to chiral systems. We acquire spin-dependent current output by constructing Au/CHPs/NiFe structured device with a ferromagnetic layer that is magnetized to a spin-up or spin-down state.

1.3 Outline of Thesis

The thesis is structured into six chapters, as follows:

Chapter 1: Introduction. This part introduces the background and origin of CHPs. After a short discussion on challenges faced in CHPs-based devices, the significance and outline of this work are shown.

Chapter 2: Literature review. A systematic review of CHPs is presented, including the material preparation methods, chirality optimization strategies, chirality transfer mechanisms, device design, unique features and a broad spectrum of advanced technologies (e.g., circularly polarized light sensing, circularly polarized luminescence, second harmonic generation, spintronics, and memory).

Chapter 3: Chiral halide perovskite film for CPL-resolved UV photonic artificial synapse. In this chapter, a heterostructure composed of single-wall carbon nanotubes and CHP is introduced for developing CPL-resolved PAS for the first time. The carrier dynamics inside the heterostructure are systematically studied with the assistance of ultrafast transient absorption (TA) technology, and effective transport of holes from CHP to single-wall carbon nanotube is demonstrated, enabling the superior CPL-resolved synaptic behavior (240 mA W^{-1}). Further, a PAS sensor array is constructed and achieves the vision, discrimination, and memory of circularly polarized images. Ultimately, the PAS-based spike neural network demonstrates a high recognition accuracy of 93% for the input training images.

Chapter 4: Chiral halide perovskite nanowire for CPL-resolved visible photonic artificial synapse. In this chapter, a CHP nanowire (NW) based PAS is fabricated to achieve full-Stokes polarimeter and polarization-dependent neuromorphic optoelectronics. CHP NW features a high CD value of over 400 millidegree (mdeg) and intrinsic linear dichroism, enabling the effective sensing of polarized light. Moreover, the NW/MXene heterostructure is constructed, and efficient charge separation is observed by TA system, yielding a high responsivity of 2.3 AW^{-1}. Excellent synaptic behavior with a low power consumption of 0.5 pJ per synaptic stimuli is successfully imitated by this PAS. Further, polarization-modulated reservoir computing (RC) is performed on the PAS device and attains a low normalized root mean square error of 0.023 in the chaotic system forecasting task.

Chapter 5: Quantum well structured chiral halide perovskite for spintronics. In this part, quantum well structured CHPs are obtained by the specific fabrication process, and then transferred to different substrates for further study. The edge states of the structure extremely enhance the vertical carrier transport ability of CHP crystal. Moreover, the high carrier mobility and current response difference (planar and vertical direction) verify the conductive features of quantum well structured CHP. Spin-dependent current is measured with the assistance of magnetic conductive atomic force microscope (mc-AFM), and typical CISS behavior is observed. Additionally, the Au/CHP/FeNi structured devices are constructed and exhibit a high spin polarization degree, showing great potential for next-generation spin memory and computing technologies.

Chapter 6: Conclusions and future work. The works in this thesis are summarized. Meanwhile, future research based on CHP is proposed.

Chapter 2 Literature Review

2.1 Overview

The pursuit of chirality in organic-inorganic halide perovskites (OIHPs) has spurred four primary engineering strategies, including the incorporation of chiral cations (direct synthesis and surface modification with chiral ligands), ion doping, chiral template growth, and hybridization with chiral metasurfaces.[2-6] Among these, embedding chiral ligands into OIHPs disrupts their centrosymmetric frameworks, enabling chirality transfer from molecular to lattice levels. This strategy yields CHPs that amalgamate the structural robustness of perovskites with the stereochemical specificity of chiral molecules.[7-9] The interplay between chiral ligands and halide perovskite matrices unlocks a wealth of unprecedented optoelectronic functionalities. On the one hand (optic perspective), CHPs feature CD, enabling polarization-selective photon harvesting. Concurrently, their non-centrosymmetric lattices facilitate efficient second-harmonic generation (SHG), and spin-polarized exciton transport and circularly polarized luminescence emerge from chirality-mediated spin-photon coupling. On the other hand (electric perspective), the chiral ligand framework induces CISS, steering spin-polarized currents with near-unity efficiency, and enhanced SOC and ferroelectric polarization enable electric-field-tunable spin manipulation. Those traits positions CHPs as versatile platforms for next-generation chiroptoelectronics containing polarization-resolved photodetectors (PDs), 3D displays, spin-filtering logic gates and non-volatile memory devices.[10-12]

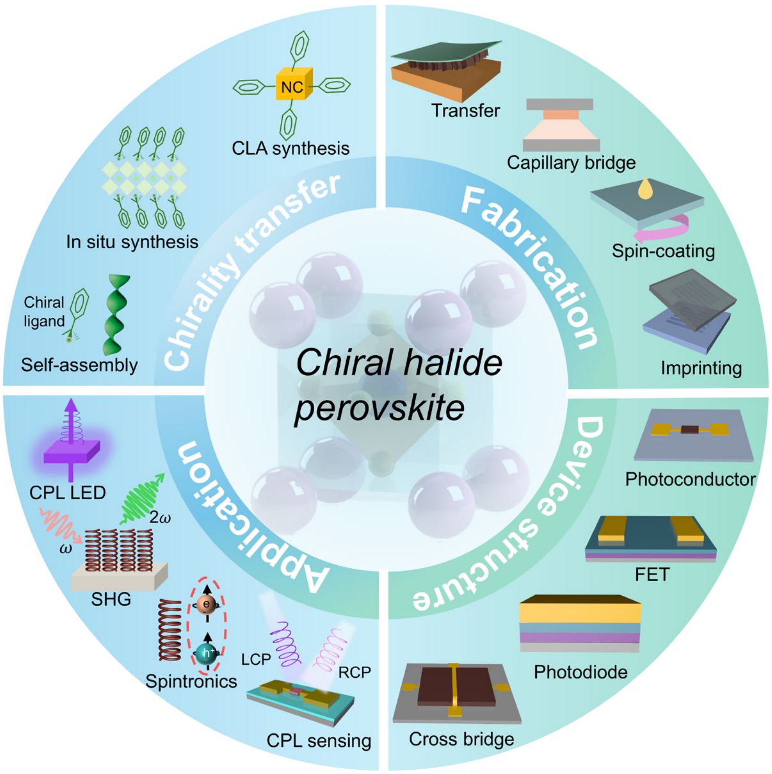

Figure 2.1 Sketch of chirality transfer, device fabrication, structure design, and advanced applications for CHPs.

This review pioneers a systematic exploration of CHPs in interdisciplinary frontiers from a device-centric perspective. The integrated framework spanning chirality transfer mechanisms, micro/nanofabrication, device engineering, and functional applications is shown in **Figure 2.1**. Here, we describe the chirality transfer mechanism of CHPs and highlight the mainstream synthesis strategies including chiral-ligand-assist (CLA) method, in situ synthesis, and direct mixture, clarifying the coupling rules between molecular chirality and the perovskite crystal lattice and band structure across multiple scales. Emerging fabrication strategies developed for CHPs with various morphologies are presented. In detail, the transfer technique for thin-layer CHP single crystal, capillary bridge effect for CHP nanowires (NWs), spin-coating method for film and template-based imprinting for microwires (MWs) are introduced. We analyze architectures, carrier transport, interface effects, and operation of various CHPs-based devices, including two-terminal photoconductors and photodiodes, three-terminal field-effect transistors (FETs), and four-terminal cross-bridge devices. Finally, cutting-edge applications covering CPL sensing PD, PAS, circularly polarized LED, and spintronics based on the CISS effect, which are achieved on CHP-based devices, are recommended.

2.2 Chirality origin

Chirality transfer—the process by which chiral molecules impart their handedness into a material's structure via chemical bonding, spatial arrangement, and electronic interactions—fundamentally alters the optical, electrical, and spin properties of the resulting CHPs.[13-15] Advancing fundamental understanding of CHPs hinges on a comprehensive exploration of their structures, chirality transfer mechanism, synthesis methods, and strategies for optimizing chiral properties. These interconnected research directions will elucidate structure-property relationships within CHPs and establish a framework for their rational design and precise engineering with tailored optoelectronic properties, driving innovation in this dynamic field.

2.2.1 Synthesis methods

Chirality transfer in CHPs is directly governed by their synthesis methodologies, which can be categorized into two dominant approaches based on the sequence of chiral ligand incorporation: CLA post-synthetic modification and direct in situ chiral synthesis. In the

CLA method, pre-synthesized achiral perovskite nanocrystals are functionalized with chiral ligands through surface coordination, where stereospecific ligand–perovskite interactions drive chirality transfer. A representative example by Rogach et al. demonstrated CLA-mediated synthesis of chiral $CsPbBr_3$ nanoplates (NPLs), where chirality originates from ligand-induced lattice screw dislocations **(Figure 2.2a)**.[16] The process involves three stages: (1) RT anti-solvent synthesis of $CsPbBr_3$ NPLs via acetone-driven crystallization of Cs-oleate and $PbBr_2$ precursors; (2) post-synthetic ligand exchange with R-/S-PEABr enantiomers under sonication; (3) centrifugal purification to yield chirally active NPLs. The stereoselective binding of PEABr ligands to bromine-terminated surface sites amplifies lattice distortion, creating helical dislocation networks that couple with quantum-confined excitons. This synergy endows the NPLs with tunable chiroptical responses, including exciton energy splitting and circularly polarized emission, providing a blueprint for designing CHPs with programmable spin-photon interactions.

Direct synthesis of CHPs enables dimensional control (0D-3D) by integrating chiral ligands with perovskite precursors during crystallization under precisely tuned conditions. Emerging techniques, i.e., antisolvent crystallization, cooling crystallization, aqueous synthesis, and evaporation crystallization, offer versatile routes to engineer CHP architecture. For example, Tian et al. synthesized 1D chiral (R/S-NEA)PbI_3 single crystals via cooling crystallization (**Figure 2.2b**).[17] The protocol involves dissolving PbO in hydroiodic acid within a sealed reactor, followed by the controlled addition of chiral NEA ligands. After stirring the precursor at 110°C to form a homogeneous yellow solution, slow cooling at programmed rates induced asymmetric crystallization, yielding millimeter-scale

CHPs crystals.

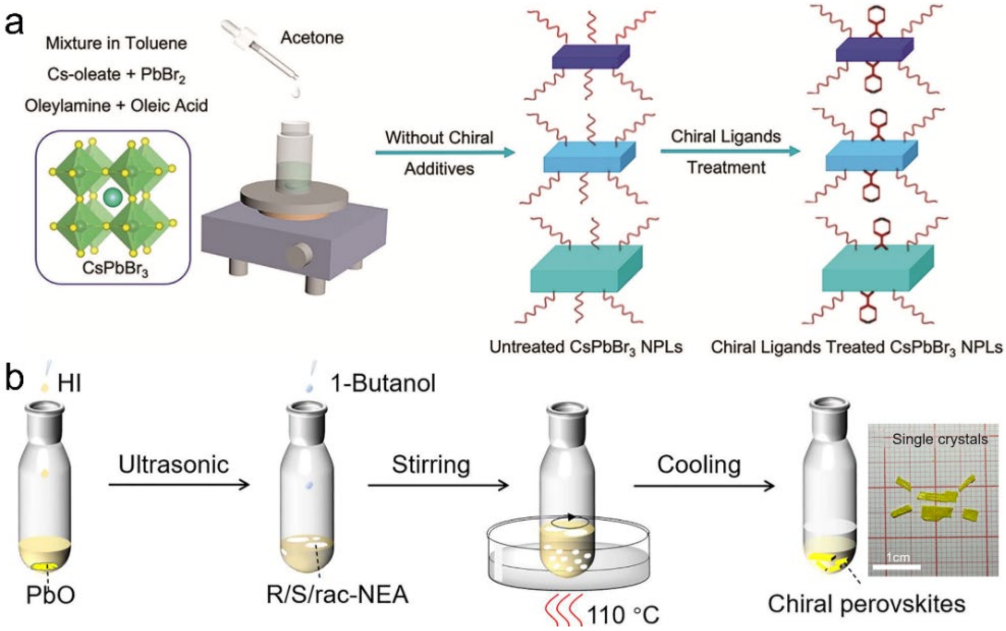

Figure 2.2 Synthesis method for CHPs. (a) Preparation of chiral CsPbBr$_3$ nanoplates capped with R-/S-PEABr ligands.[16] (b) Cooling crystallization method for synthesizing (S/R-NEA)PbI$_3$ and (rac-NEA)$_2$PbI$_4$.[17]

2.2.2 Chirality optimization

The chiroptical properties of CHPs, including CD, circularly polarized luminescence, and spin polarization, are pivotal for their applications in spin-resolved photonics and quantum optoelectronics. Enhancing these chirality-dependent properties is essential to improve the performance of chiral perovskite-based devices. To optimize the chirality, a series of strategies including doping,[18] chemical composition engineering,[19] solvent-mediated crystallization,[20] and dimensional confinement have been proposed.[21-23] For example, targeted doping with specific cations or anions strengthens CD signals by modulating lattice symmetry and spin-orbit interactions. Solvent engineering fine-tunes crystallization kinetics to stabilize chiral phases with reduced defects, while dimensional control in 2D/3D heterostructures enhances CPL intensity via quantum-confined exciton-photon coupling. Additionally, chiral ligand passivation suppresses non-radiative losses to prolong spin-polarized carrier lifetimes. These coordinated efforts collectively address the critical link between chirality enhancement and device performance, enabling breakthroughs in spin-polarized light-emitting diodes (LEDs), polarization-discriminative PDs, and high-density spintronic memory systems.

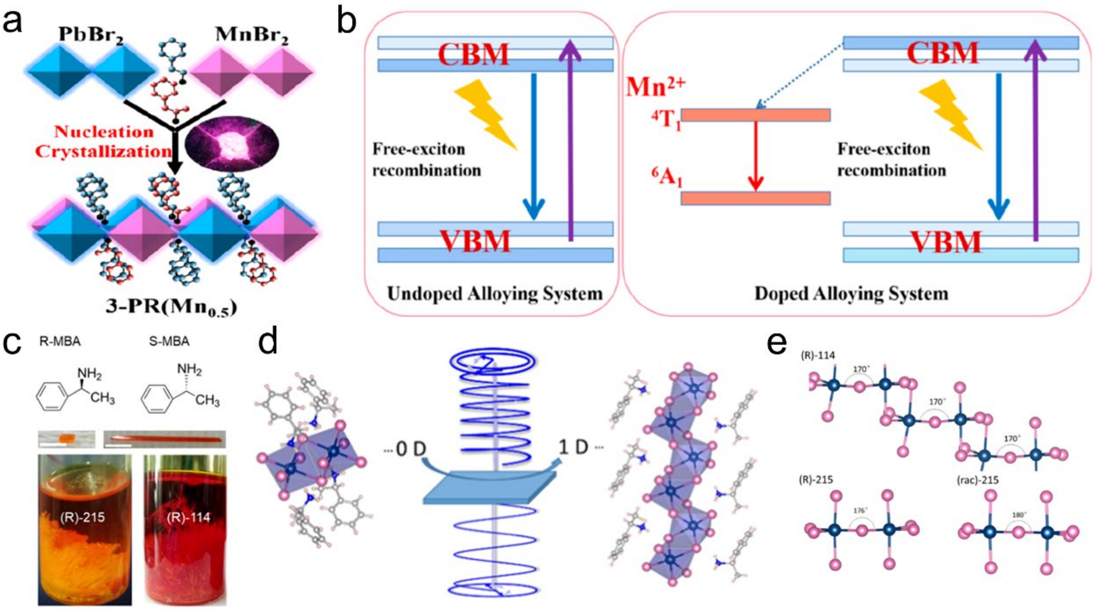

Figure 2.3 Chirality optimization methods. (a) Structure diagram of Mn-doping chiral perovskite. (b) Energy transfer and enhanced PL mechanism of 2D CHP doped with Mn^{2+}.[24] (c) Molecular structures of chiral ligands (up), chiral perovskite crystals (middle), and as-grown 0D (R/S-MBA)$_2$SbI$_5$ and 1D (R/S-MBA)SbI$_4$ (down), namely (R)-215 and (R)-114. (d) Sketch illumination of dimension-enhanced chirality. (e) Inorganic framework of 0D, 1D, and racemic chiral perovskite.[21]

Zhao et al. doped manganese ions (Mn^{2+}) into 2D CHP in which chiral cations and achiral inorganic blocking co-exist, and obtained efficient photoluminescence (PL).[24] As illustrated in **Figure 2.3a**, the crystal structure comprises blue $[PbBr_6]^{4-}$ and pink $[MnBr_6]^{4-}$ octahedra, with the inset showing bright emission under 365 nm UV excitation. To illuminate the enhancement of the PL, the author sketches the bandgap and energy transfer process. Under excitation, the sample is excited from the ground state to the free exciton state followed by a radiation recombination process (free exciton return to the ground state). The doping of Mn^{2+} provides a new radiation path, namely the exciton recombination way, where the energy is transferred from free exciton to the $^4T_1$ state of manganese ions. This energy transfer of light-stimulated exciton from the host to inside Mn^{2+} facilitates the radiation recombination, thereby boosting the PL performance.

Similarly, Lu et al. achieved circularly polarized PL and exciton splitting in Mn^{2+}-doped $(S/R\text{-}MPA)_2PbBr_4$, where increasing Mn^{2+} concentration boosted the PL quantum yield to 24% and dissymmetry factor to 0.11 (**Figure 2.3b**). [18] The enhancement aligns with Zhao's energy transfer model, confirming the universality of Mn^{2+}-mediated chirality amplification. Expanding this strategy, Co^{2+} doping in achiral perovskites was shown to induce a Zeeman effect, breaking spin degeneracy and generating spin-polarized carrier populations. [25] This spin imbalance enhances circularly polarized PL and photoresponse, achieving a 15% improvement in spin polarization efficiency compared to undoped systems. Collectively, these studies validate ion doping as a versatile strategy to engineer chiral activity through tailored spin-photon interactions, offering a scalable route to high-performance chiroptoelectronic devices.

Dimensional engineering of CHPs offers a powerful route to amplify chirality. Tang et al.

systematically compared 0D (R)-215 and 1D (R)-114 CHPs (**Figure 2.3c**), revealing a tenfold enhancement in CD anisotropy factor of (R)-114 (**Figure 2.3d**).[21] Density functional theory (DFT) calculation demonstrates that the fronter orbitals of conduction band minimum (CBM) and valence band maximum (VBM) of (R)-114 and (R)-215 are composed of inorganic sublattices with antimony and lead-derived states, and the optimized chirality may come from the chiral-ligand-improved inorganic configuration. Further, the bending angles of the octahedrons in 1D ($[Sb_2I_8]_n^{2n-}$ loop chain) and 0D ($[Sb_2I_{10}]^{4-}$ dimer) are sketched in **Figure 2.3e** to understand the structure-induced CD difference. The former exhibits a higher bending angle than the latter while the racemic perovskite shows no bending angle, and the author deduced that this structural difference from dimensionality might interpret the CD strength. Complementing this, Choi and co-workers achieved dimensionality-tunable CHPs using three distinct chlorine-substituted ligands.[26] The substitution position of the chlorine atom decided the structural dimensionality and chiroptical properties of CHP. When the chlorine-substituted ligands were shifted to the ortho position, 1D CHP with self-powered sensing mode exhibited the best anisotropy factor of 1.25. The work demonstrates how dimensionality control, guided by substituent positioning, enables CHPs to surpass classical chiroptical limits, opening avenues for self-powered polarization sensors and chiral photonic circuits. A. Ishii et al. pioneered ultrahigh CD in CHP films (> 3000 mdeg) by engineering organic–inorganic interactions in 1D and 2D architectures.[27] In the FTIR (Figure 4g), the N-H stretch band emerges at 3120 and 3050 cm^{-1} for 1D and 2D CHPs, respectively, which indicates the hydrogen ion of $-NH_3^+$ group in NEA^+ intensively interacts with iodide ion in $(PbI_6)^{4-}$. It can be seen that the 1D

CHP shows a stronger interaction indicated by the peak intensity. Further, the relationship between the dimension of CHP and chiroptical properties is explored and plotted in Figure 4h, and the CHP exhibits a higher anisotropy factor of CD (g_{CD}, calculated by CD/(32980 × absorbance)) in 1D structure. In addition to the strong bonding interaction, another key factor is the addition of methylammonium iodide (MAI) in the synthesis process of (R/S-NEA)PbI_3. The $MAPbI_3$ coexists with the 1D phase CHP in the film. Under the synergistic effect of the $MAPbI_3$ and (R/S-NEA)PbI_3, the fabricated film exhibits an extremely high CD signal, about an order of magnitude higher than that without the addition of MAI. The crystallinity and the surface smoothness of the 1D CHP film are dominated by the coexistence of $MAPbI_3$. The CHPs without the addition of $MAPbI_3$ exhibit amorphous states, which significantly discounts the chiroptical properties. This work underscores dimensional control and phase engineering as dual levers for maximizing chirality in hybrid perovskites.

2.3 Device design and fabrication

The structural design of CHPs-based devices serves as a foundational determinant of their operational performance and application boundaries, governing both fundamental photophysical processes and practical functionality. By strategically engineering device architectures, researchers can modulate critical operational parameters such as carrier transport trajectories, photon harvesting efficiency, and interfacial stability.[28-30] Those factors collectively dictate the ultimate photoconversion quantum yield, temporal response characteristics, environmental tolerance, and spectral operating ranges of the resulting devices. Emerging architectural paradigms have crystallized into several dominant configurations, and each exhibits distinct structure-property relationships tailored for specific optoelectronic functionalities. Two-terminal planar architectures, including photoconductors and photodiodes, leverage in-plane carrier transport mechanisms to achieve polarization-discriminative photodetection with sub-nanosecond response times, making them particularly suitable for high-speed chiroptical sensing applications. Three-terminal field-effect transistor (FET) configurations feature gate-tunable capabilities, enabling dynamic modulation of spin-polarized charge injections. Four-terminal cross-point architectures employ orthogonal electrode arrangements to measure the magnetoresistance (MR) of CHPs.

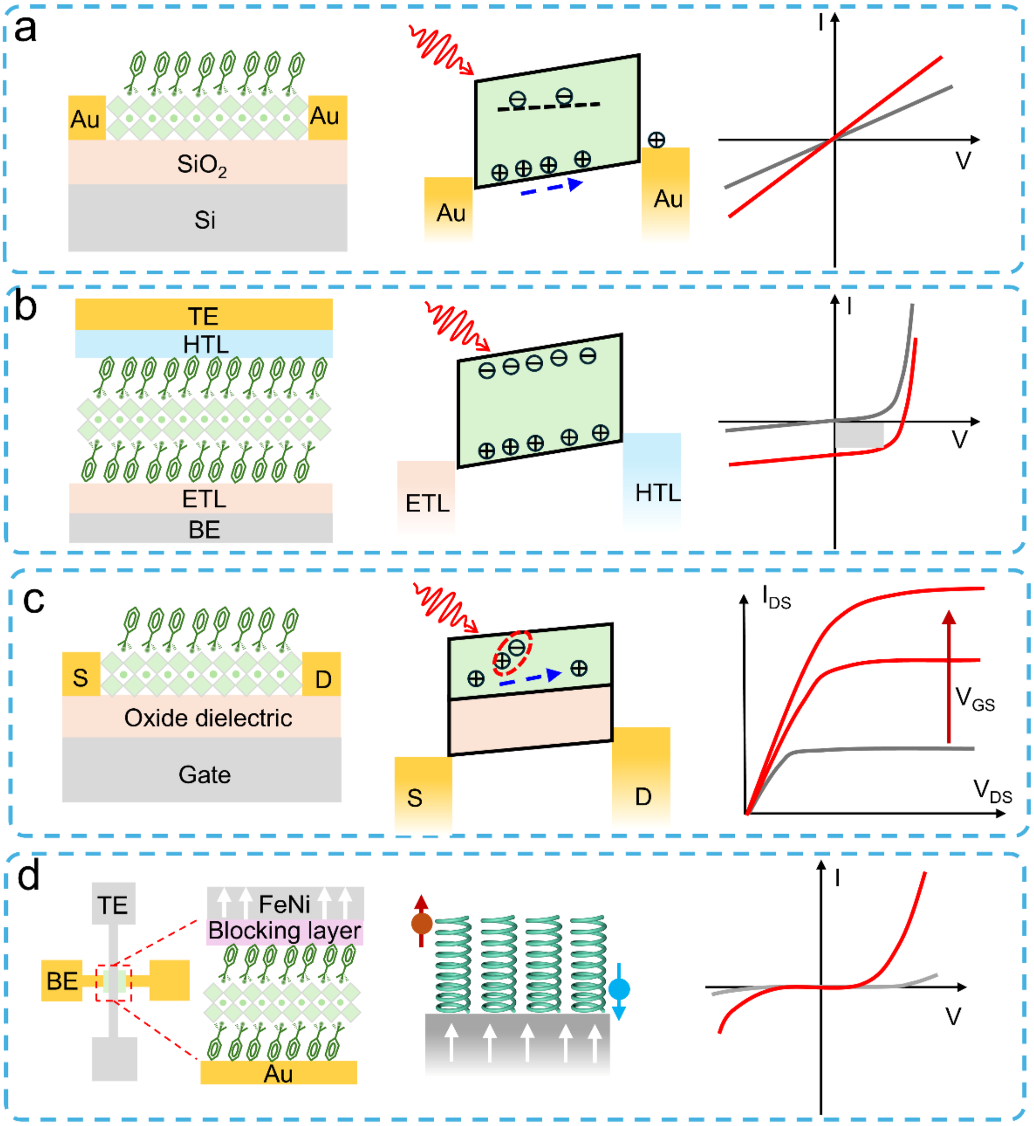

Figure 2.4 Summarized device structures, carrier transport mechanism and I-V characterization. (a) Two-terminal photoconductor. (b) Two-terminal photodiode. (c) Three-terminal FET. (d) Cross bridge structure with four terminals.

Photoconductors employ simple planar architecture where CHP films are directly sandwiched between two metal electrodes (**Figure 2.4a**, left). In this configuration, interfacial properties between electrode and CHP critically govern charge transport dynamics. The inherent defect-rich nature of CHPs introduces a high density of mid-gap states, which elevates dark current levels but simultaneously enables substantial photoconductive gain. Under an applied electric field, photogenerated carriers undergo multiple transits through the device before recombination, a mechanism where a single photon triggers numerous carrier circulation events, thereby achieving high photoresponsivity. However, these defects also act as charge traps, prolonging carrier lifetimes and consequently slowing response speeds to microsecond-millisecond timescales (**Figure 2.4a**, middle). Operationally, photoconductors require external bias to sustain Ohmic conduction, with current-voltage characteristics showing a linear dependence on the applied voltage. Under illumination (red curve), conductivity surges dramatically due to photogenerated carriers, while the baseline dark current (black curve) remains relatively low but exhibits defect-mediated leakage (**Figure 2.4a**, right).

In contrast, photodiodes adopt p-n or p-i-n junction architectures (**Figure 2.4b**, left), integrating CHP as the photoactive layer interfaced with charge-selective transport layers. Typically, TiO_2 serves as the electron transport layer (ETL) and Spiro-OMeTAD is utilized as the hole transport layer (HTL).[31-33] The built-in electric field at the heterojunction rapidly separates photogenerated electron-hole pairs, directing carriers through their respective transport layers to electrodes (**Figure 2.4b**, middle). This engineered charge extraction pathway suppresses bulk and interfacial recombination, enabling ultrafast nanosecond-scale response times and approaching Shockley-Queisser efficiency limits. The optimized energy-level alignment manifests in characteristic photovoltaic behavior under illumination, producing measurable short-circuit currents and finite open-circuit voltages (**Figure 2.4b**, right).

The structure of a CHP FET (**Figure 2.4c**, left) closely resembles that of a conventional FET, comprising a semiconductor layer, source (S), drain (D), gate electrode, and dielectric layer.[34-35] In this configuration, CHPs act as the conductive channel, where crystal quality critically influences charge transport efficiency and overall device performance. The dielectric layer, typically SiO_2, Al_2O_3, or polymers like PMMA, serves to electrically isolate the gate electrode from the perovskite channel. CHP-based FETs exhibit ambipolar charge transport, enabling concurrent electron and hole conduction. Their carrier type dominance (n-type or p-type) can be engineered through compositional tuning, such as modifying A-site cations or adjusting halide ratios. A key advantage of chiral perovskites lies in their strong photon absorption, which generates abundant electron-hole pairs under illumination. An external gate bias facilitates the separation of these photogenerated carriers: electrons migrate toward the drain electrode, while holes drift to the source, collectively producing a measurable photocurrent (**Figure 2.4c**, middle). The current-voltage (IV) characteristics of CHP-FETs are captured through transfer curves (ambipolar behavior) and output curves (**Figure 2.4c**, right). In the linear regime, the drain-source current (I_{DS}) scales linearly with drain-source voltage (V_{DS}), governed primarily by channel resistance. In the saturation regime, I_{DS} plateaus and becomes controlled by the gate-source voltage (V_{GS}). Through strategic structural design, material optimization (e.g., defect passivation), and interface engineering, CHP-FETs demonstrate significant potential for next-generation optoelectronic and spin-selective devices. However, their commercialization faces persistent challenges, including long-term environmental stability, scalable fabrication methods, and manufacturing reproducibility. Addressing these hurdles will be critical to unlocking their practical applications.

When spin-unpolarized carriers traverse CHPs, they acquire a chirality-dependent spin polarization via the CISS effect. This phenomenon, which enables spin-filtering charge transport, holds transformative potential for spin-based memory and other spintronic devices. To quantify the CISS effect, a four-terminal cross-point device (**Figure 2.4d**, left) is employed. The vertical heterostructure comprises an inert bottom electrode (BE; e.g., Au, Pt), a CHP layer, a blocking layer (e.g., oxide or organic insulator), and a ferromagnetic top electrode (TE; e.g., Ni, Co, FeNi).[36-39] Unlike magnetic conductive atomic force microscopy (mc-AFM), which probes nanoscale regions, this architecture enables macroscopic measurements of spin-selective transport across bulk chiral perovskite films, aligning with practical device requirements.[40-41] In this configuration, charge carriers spontaneously develop spin polarization at the termini of the chiral perovskite's helical structure (**Figure 2.4d**, middle). Spin-polarized electrons injected from the magnetized ferromagnetic TE propagate through the CHP layer, exhibiting markedly distinct conductance for spin-up and spin-down currents due to the material's spin-selective filtering properties (**Figure 2.4d**, right). MR measurements further elucidate spin transport dynamics. Using a four-probe vertical cross-bridge structure, a constant DC bias is applied between the TE and BE, while the voltage drop across the junction is monitored via a separate electrode pair. By sweeping an external magnetic field perpendicular to the device plane, the MR, defined as the relative change in resistance with magnetization direction, reflects spin injection efficiency. Notably, this four-terminal design enables efficient spin injection into nonmagnetic semiconductors or metals without requiring external magnetic fields, a breakthrough for spin applications such as spin filters, spin-FETs, and nonvolatile spin memories.

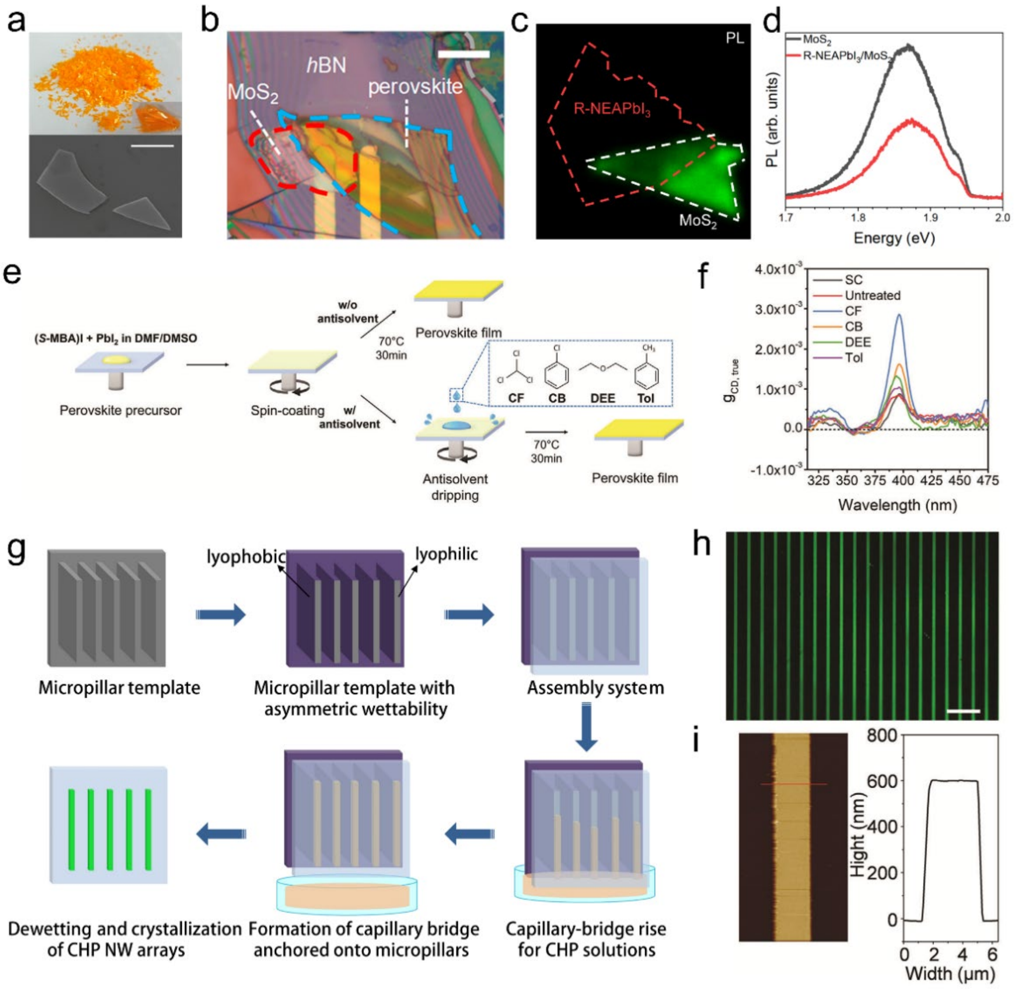

Figure 2.5 Summarized methods for chiral perovskite-based devices. (a) Optical and SEM images of (R- and S-MBA)$_2$PbI$_4$ crystal. The scale bar is 5 μm. (b). Image of the MoS$_2$/chiral perovskite heterostructure.[42] (c) PL mapping of MoS$_2$/R-NEAPbI$_3$. (d) PL of MoS$_2$/R-NEAPbI$_3$.[43] (e) Schematic diagram of the fabrication of chiral perovskite film. (f) Anisotropy factor of chiral perovskite by different treatments.[20] (g) schematic diagram of fabrication of chiral perovskite microwires by CBA method. (h) Fluorescence microscopy image of microwire array. (i) AFM of the single microwire.[44]

Dry transfer methods using polydimethylsiloxane (PDMS) stamps and wet transfer techniques (e.g., PMMA-assisted transfer) are widely employed for assembling 2D crystal materials such as graphene and transition metal dichalcogenides.[45-47] However, transferring CHPs presents unique challenges due to their environmental sensitivity (degradation under humidity/temperature fluctuations) and mechanical fragility. Recent advancements in modified transfer protocols have enabled the integration of CHPs with 2D materials, opening avenues for high-performance optoelectronic devices. In a notable study, Li et al. synthesized millimeter-scale needle-like (R/S-MBA)$_2$PbI$_4$ crystals with distinct orange coloration **(Figure 2.5a)** and constructed a MoS$_2$/CHP heterostructure to achieve circularly polarized luminescence CPL.[42] Exfoliated thin layer of (R-MBA)$_2$PbI$_4$ crystal, which was checked by scanning electron microscopy (SEM), demonstrated a flat surface owing to the layered properties of 2D chiral perovskites. To fabricate the device, the Au electrode with a channel of 10 μm was defined by photolithography, followed by thermal evaporation and lift-off. The few-layer MoS$_2$ sheet was aligned and transferred onto one side of Au electrode with the assistance of microscope and manipulator. The perovskite sheet was exfoliated from synthesized bulk crystal by Scotch tape, and then was transferred to the other side of the predefined Au electrode. Ultimately, a hexagonal boron nitride (*h*-BN) flake as an encapsulation layer was transferred onto the top area of the as-prepared heterostructure (**Figure 2.5b**) to protect it from being damaged by the air. This CHP/MoS$_2$ design achieved circularly polarized luminescence with a dissymmetry factor of 17%, demonstrating significant potential for miniaturized CPL devices.

Another study by Colet et al. explored valley polarization in R/S-NEAPbI$_3$/MoS$_2$

heterostructures using dry transfer methodology.[43] Monolayer MoS_2 was prepared utilizing a typical mechanical exfoliation method. Briefly, the few-layer MoS_2 bulk on the tape was further folded and peeled several times to thin the flake. The as-exfoliated monolayer was confirmed by the optical microscope (from color level), Raman spectroscopy (peak intensity), and atomic force microscope (thickness). For the transfer of the 1D chiral perovskite. the R/S-$NEAPbI_3$ crystal was exfoliated on the PDMS stamp, and then the sample was aligned on the top of the monolayer MoS_2 by transfer stage equipment. The stamp was down slowly and finally contacted the MoS_2. With the release of the PDMS stamp, the chiral perovskite was left on the MoS_2. **Figure 2.5c** exhibits the PL mapping of the R-$NEAPbI_3$/MoS_2 heterostructure. The overlap area exhibits an obvious quench signal compared with the MoS_2-only region (**Figure 2.5d**), indicating a photo-excited electron transfer from the conduction band of MoS_2 to R-$NEAPbI_3$. The transfer method in this work demonstrates an innovative way to explore valleytronics. Despite these successes, CHP transfer remains inherently more complex than conventional 2D material assembly. Key challenges include susceptibility to lattice distortion during mechanical exfoliation, solvent-induced degradation in wet transfer processes, and interfacial contamination from residual polymers (e.g., PDMS/PMMA). Addressing these limitations through controlled-environment protocols, advanced encapsulation strategies, and solvent-resistant CHP formulations will be critical for advancing scalable device fabrication.

Spin-coating, a widely adopted thin-film deposition technique in perovskite optoelectronics (e.g., solar cells, LEDs, PDs), utilizes centrifugal force to achieve uniform solution distribution.[48-51] The quality of the resulting perovskite film critically depends on multiple parameters: spin speed/duration, solution composition (concentration, solvent selection, and antisolvent treatment), annealing conditions, and ambient environment. Yang et al. enhanced the chiroptical properties of polycrystalline CHP films through antisolvent-assisted spin-coating optimization (**Figure 2.5e**).[20] They synthesized 1D S-MBAPbI_3 by dissolving S-MBAI and PbI_2 in a mixed solution of dimethyl sulfoxide (DMSO)/DMF (30 wt%). During spin-coating on substrates, antisolvents including chloroform (CF), chlorobenzene (CB), diethyl ether (DEE), and toluene (Tol), were dripped to modulate crystallization, followed by thermal annealing at 70°C for 30 min. The CF-treated films exhibited the highest circular dichroism (g_{CD}) factor (**Figure 2.5f**), attributed to CF’s strong polarity enabling hydrogen bonding with DMSO. This interaction suppressed parasitic phase formation, accelerated 1D perovskite crystallization, and reduced iodine vacancy density. The resultant structural homogeneity enhanced asymmetric distortion in inorganic frameworks, amplifying overall film chirality.

In terms of the CBA approach, Zhao et al. synthesized (R/S-MBA)$_2$PbI_4 NWs with high crystallinity and ordered crystallographic alignment,[44] and the assembly system is sketched in **Figure 2.5g** in detail. The micropillar templates were selectively functionalized by heptadecafluorodecyltrimethoxysilane (FAS) to create lyophobic sidewalls and lyophilic bottoms. The assembly system containing the template and flat substrate was perpendicularly placed on the CHP precursor. Subsequently, the solution rises into the gaps between the micropillar tops and the substrate under the combined action of capillary forces and Laplace pressure, forming discrete capillary bridges anchored at the micropillar surface. Single-crystal NWs arrays were defined on the substrate after the dewetting process. The uniform and bright green fluorescence of the array (**Figure 2.5h**) indicates that homogenous and high-crystallinity CHP NWs are obtained. For clear observation of the NWs profile, AFM measurement was implemented, and the NWs exhibit a uniform height of 600 nm (**Figure 2.5i**). This approach leverages capillary force-mediated precursor confinement and crystallization kinetics modulation, enabling scalable fabrication of CHP NWs arrays with tunable optoelectronic properties.

2.4 Advanced applications based on chiral halide perovskites

Chiral perovskites have emerged as a cornerstone material system for next-generation chiroptoelectronic and spintronic technologies, capitalizing on their unique helical crystallographic frameworks, CISS, and intrinsic nonlinear optical properties. These materials are driving transformative applications across diverse cutting-edge domains, including CPL-resolved PD, PAS, circularly polarized luminescence, spin-polarized charge transport, and SHG. The synergistic interplay of chirality-mediated optical, electrical, magnetic, and spin degrees of freedom enables unprecedented device functionalities characterized by ultracompact integration, ultralow power consumption, and dynamic reconfigurability. By transcending the performance limitations of conventional optoelectronic materials through tailored multiaxial physical field coupling, CHPs establish a versatile platform for next-generation intelligent systems spanning quantum photonics, neuromorphic computing, and adaptive opto-spintronic architectures.

2.4.1 CPL sensing detector and photonic artificial synapse

In PD devices, photogenerated electron-hole pairs undergo rapid separation at the perovskite layer or heterojunction interface, followed by efficient collection at electrodes to generate transient photocurrent. The system exhibits reversible behavior, returning to its baseline state immediately upon illumination removal, with no inherent memory functionality. In contrast, PAS utilizes defect-mediated carrier dynamics within perovskites, and photoinduced charges become trapped at intrinsic defect sites, inducing persistent modifications in device conductivity. These conductivity states demonstrate nonvolatile retention over extended durations, effectively emulating the memory characteristics of biological synapses. Crucially, synaptic weight modulation can be dynamically programmed through temporally coded light pulse sequences, enabling sophisticated spatiotemporal information processing capabilities.

The helical structure of CHPs breaks spatial symmetry, endowing them with CD values far exceeding those of traditional chiral organic materials (<10 mdeg). This strong asymmetry enables CHPs to exhibit markedly distinct absorption of left- and right-circularly polarized light (LCP/RCP). Figures of merit for evaluating optical detection performance include responsivity(R), detectivity(D^*), and response time, among others. R reflects the capability of the detector in converting optical signals into electrical signals, and a large R value indicates a high sensitivity toward weak light. R is calculated by $R = \Delta I/(P \times S)$, where ΔI is the difference between photocurrent and dark current (i.e., $I_{light} - I_{dark}$), P is power of incident light and S is effective area. D^* is utilized to characterize the performance of detectors with different sizes and bandwidths, which represents the response resolution of the PDs. D^* is expressed as $D^* = (S \times \Delta f)^{1/2}/NEP$, where S is the exposed area, Δf is operating bandwidth, and NEP (I_{noise}/R, I_{noise} is the noise current) is noise equivalent power. Response time (μ) is usually characterized by subjecting the detector to a pulsed light source and recording the time it takes for the output signal to rise from a low level to its steady state (rise time) or decay back to the baseline (fall time). It shows the response speed of detector toward variation of external signals. Tang et al. capitalized on this property by developing a planar (R/S-α-PEA)PbI_3-based PD with exceptional responsivity of 797 mA W^{-1} and detectivity of 7.1×10^{11} Jones (**Figure 2.6a**).[52] The α-PEA ligand, featuring conjugated π bonds, enhances Coulomb interactions between chiral cations and $[PbI_6]^{4-}$ octahedra, amplifying CPL discrimination. Wavelength-dependent responsivity and photoconductor gain of the PD toward various wavelengths (365, 395, 430, and 530 nm) are summarized in **Figure 2.6b**. Responsivity peak (0.12 A W^{-1}) could be observed at 395 nm, indicating the best distinguishing ability for 395 nm LCP and RCP. However, the difference in other wavelengths is not obvious and the difference disappears at 530 nm, which is identical to the absorption and CD spectra. In addition to excellent CPL response behavior, the proposed CHP-based PD also exhibits superior stability. A comparison between the fresh device and the old device (in ambient conditions after one month) is performed, and the consistent response toward 395 nm CPL indicates that the device shows no degradation. This work demonstrates a CPL PD with remarkable optoelectronic performance and strong stability, establishing a pathway for miniaturized polarization-resolved imaging systems with robust operational longevity.

Recent advances in neuromorphic engineering have yielded chiral perovskite-based PAS devices that emulate synaptic plasticity through polarization-encoded optical stimuli. Pal et al. developed a bio-inspired ITO/CHP/PMMA/Al structured PAS (**Figure 2.6c**), where the CHP layer functions as a polarization-sensitive synaptic cleft.[53] Excitatory postsynaptic current (EPSC) triggered by a single LCP/RCP spike was successfully imitated by the R-type and S-type devices (**Figure 2.6d**), respectively. For an R-type device, a higher EPSC peak is observed under the stimulation of the LCP beam, and the response gap indicates that the PAS device is capable of discriminating the circular polarization states. The S-type PAS exhibits similar CPL distinguishing ability but an opposite response preference. Short-term plasticity (STP) could be converted to long-term plasticity (LTP) by increasing the stimuli CPL spikes. The EPSC response of the PAS device depends on both the current input stimuli and historical state and generally exhibits an ascending trend with the increase of CPL spikes.[54-55] To elucidate the synaptic behavior, a charge trapping-detrapping mechanism was proposed and verified by Kelvin probe force microscopy (KPFM). In detail, the photoinduced holes can escape the CHP layer and leave the electrons in the conduction band, which decreases the Schottky barrier at the ITO/CHP interface, leading to the potentiation behavior (conductivity enhancement). Without illumination, the quantum wells in the CHP trapping the carriers delay the electron-hole recombination and induce a slow decay of the EPSC behavior.

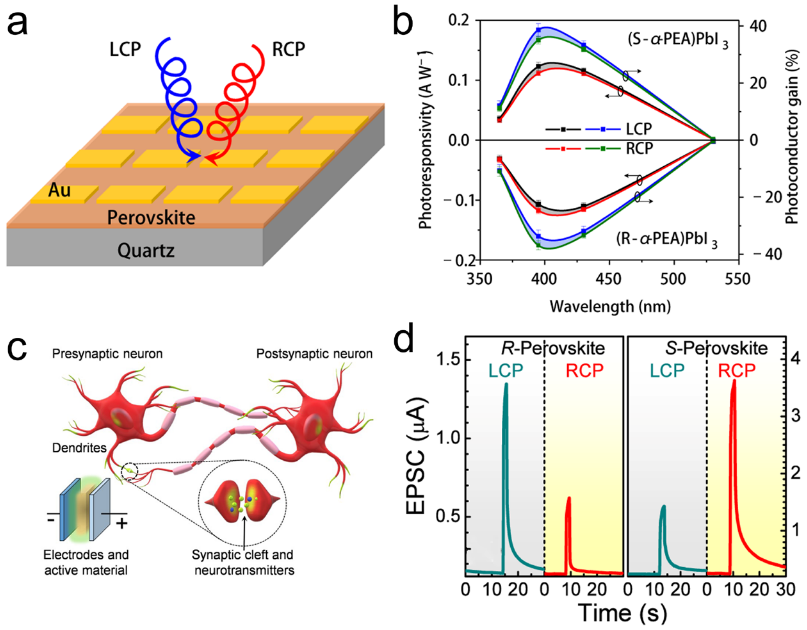

Figure 2.6 CPL resolved PD and PAS. (a) Sketch of (R-and S-α-PEA)PbI_3 film PD. (b) Responsivity and photoconductor gain under different wavelengths.[52] (c) Sketch of the biological and artificial synapse. (d) EPSC of R-type and S-type PAS in response to LCP and RCP stimulation.[53]

2.4.2 Circularly polarized LEDs

Circularly polarized luminescence devices based on CHPs typically employ a multilayer heterostructure design comprising a transparent conductive substrate (ITO), ETL (PCBM, TiO_2, and SnO_2), CHP luminescent layer, HTL (Spiro-OMeTAD and PEDOT: PSS), and metal electrodes. The exceptional CPL performance originates from the intrinsic spin-orbit coupling within the chiral perovskite lattice. Here, symmetry breaking, induced by chiral organic ligands or distorted inorganic frameworks, generates a pronounced Rashba band splitting. This splitting produces spin-polarized charge carriers during exciton recombination, while the CISS effect directly converts electron spin angular momentum into photon circular polarization. Strong photon-exciton coupling further amplifies the luminescence dissymmetry factor (g_{lum}), enabling devices to achieve external-optics-free, wavelength-tunable, and high-efficiency CPL emission.

This unique structure-property interplay positions CHP-based CPL devices as transformative light sources for next-generation technologies. Their ability to intrinsically generate and modulate circularly polarized light, without relying on bulky optical components, makes them ideal for applications demanding compact, tunable, and high-purity CPL, including quantum information encryption, ultrahigh-resolution 3D displays, and chirality-sensitive biosensing. By unifying chiral photonic control with perovskite optoelectronics, these systems open pathways for multifunctional, miniaturized photonic platforms that bridge quantum optics, spintronics, and bio-inspired sensing.

Two-dimensional CHPs exhibit strong CD signals, however, their optoelectronic utility is limited by severe non-radiative recombination, which quenches PL and circularly polarized luminescence activity. Addressing this challenge, Wang et al. pioneered an innovative heterostructure design that synergizes 2D CHP with $CsPbBr_3$ quantum dots (QDs), unlocking unprecedented CPL performance.[56] The team synthesized 2D CHP by intercalating chiral organic molecules (R/S-MBA) into a lead iodide perovskite lattice, inducing a chiral arrangement in the inorganic framework. Concurrently, cubic-phase $CsPbBr_3$ QDs (~10 nm diameter) were prepared via solution processing. The heterostructure was fabricated by spin-coating a $CsPbBr_3$ QDs layer (dissolved in n-hexane) onto the 2D CHP film, forming a vertically stacked architecture (**Figure 2.7a**). Halogen anion exchange at the interface (I^- with Br^-) transformed the QDs into mixed-halide $CsPbBr_{3x}I_{3(1-x)}$, red shifting the PL emission from 515 nm (pristine QDs) to 540 nm (heterostructure). By modulating the CHP layer thickness or halide composition (e.g., R/S-MBA)$_2$PbBr$_x$I$_{4(1-x)}$), the team achieved precise tuning of emission wavelengths (550-647 nm) and CPL asymmetry factors ($|g_{lum}|$ up to 6×10^{-3}). The spin polarization imbalance leads to the emission of circularly polarized light during the radiative recombination of the QDs layer, with the intensity positively correlated to the thickness of the CHP layer. **Figure 2.7b** shows the circularly polarized luminescence with the concentration of CHP precursor reaching 50 wt%. TA spectroscopy revealed excitation energy transfer from the 2D CHP to QDs, generating spin-polarized excitons. Interface coupling between CHP and QDs extended exciton spin lifetimes from 3.4 ps to 14.4 ps, suppressing spin decoherence and amplifying CPL emission. This work ingeniously repurposes the inherent non-radiative recombination of 2D CHPs, traditionally a drawback, into a spin-control mechanism that enhances CPL efficiency of QDs. By elucidating the roles of energy transfer and interfacial spin manipulation, the study not only broadens the optoelectronic applicability of CHPs but also establishes a blueprint for high-performance, CPL-active devices. These advances pave the way for spin-optoelectronic systems in quantum communication, chiral photonics, and energy-efficient displays.

Beard et al. successfully realized RT spin light-emitting diodes (spin-LEDs) operating without external magnetic fields by harnessing the CISS effect in CHPs.[57] Utilizing the self-assembled structure of (R/S-MBA)$_2$PbI$_4$, they achieved a spin-polarized hole current exceeding 80%. In the constructed spin-LEDs (**Figure 2.7c**), the chiral organic molecules are oriented perpendicular to the substrate, with their helical axes aligned with the charge transport direction. This configuration selectively filters charge carriers of specific spin orientations through the CISS effect, eliminating the reliance of traditional spin-LEDs on ferromagnetic materials or magnetic fields. The device emits CPL at RT, achieving a polarization degree of ±2.6% at 688 nm, the highest reported value for pure $CsPbI_3$ QDs systems. This mechanism arises from the radiative recombination of spin-polarized holes and unpolarized electrons in the QDs layer, while interface coupling suppresses spin relaxation, extending the spin lifetime to 14 ps and significantly enhancing the CP-EL efficiency. Electrically driven halide exchange (e.g., Br^-/I^- dynamic substitution) enables continuous tuning of emission wavelengths from red (688 nm) to green (515 nm). Mixed-halide QDs ($CsPbBr_{3x}I_{3(1-x)}$) exhibit a spin coherence lifetime of 14 ps, a 3.5-fold increase over pure $CsPbI_3$ QDs (4 ps), validating spin dynamics optimization through compositional engineering. This work represents a profound integration of spintronics and perovskite optoelectronics, offering a foundation for advancing spin-photonics as a critical post-Moore-era technology.

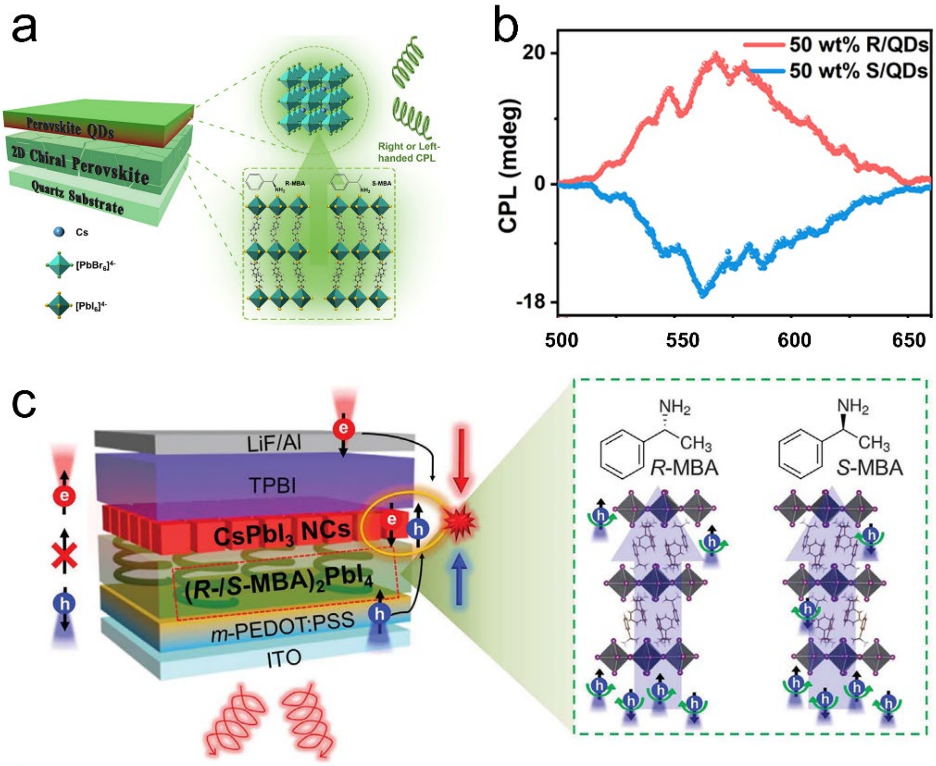

Figure 2.7 Circularly polarized luminescence. (a) Sketch for the structure of $CsPbBr_3$ QDs and 2D CHP heterostructure. (b) Circularly polarized luminescence spectra of R-type and S-type heterostructure.[56] (c) CP-EL in CHP-based spin-LEDs.[57]

2.4.3 Chiral lasing

For halide perovskite, lasing is an attractive application which represents a milestone in modern photonics. Chiral perovskites have emerged as a groundbreaking class of materials for chiral lasing. The unique structural and optoelectronic properties position CHPs as frontrunners in advancing chiral lasing, a technology that generates coherent CPL with controlled spin states. Intrinsic properties of CHPs such as strong SOC, exceptional optical gain, tunable bandgap and spin-dependent amplification are advantageous in building chiral lasing systems. In detail, the chiral crystal lattice enhances spin-polarized carrier recombination, directly coupling photon spin to material chirality, which results in direct generation of CPL lasing without post-emission filtering. This eliminates the need for external polarizers or complex optical setups, simplifying device design. Efficient light emission of CHPs reduces lasing thresholds. Compositional engineering (e.g., adjusting halides like Br, I, or Cl) allows wavelength-specific laser applications.

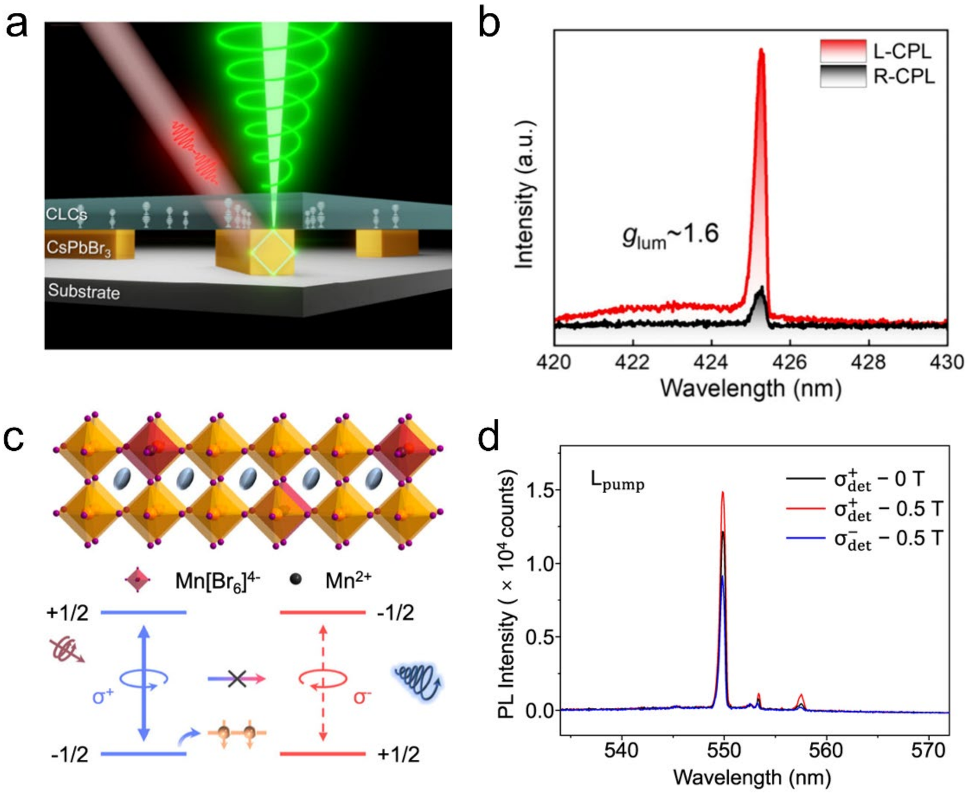

Figure 2.8 Chiral lasing. (a) Sketch of chiral micro-laser device. (b) CPL lasing.[58] (c) Sketch diagram exhibiting suppression of spin relaxation by Mn^{2+} doping. (d) Laser emission under a magnetic field.[59]

Currently, different strategies are explored to achieve chiral lasing, but most are based on halide perovskite, including doping, chiral metasurface coupling, and liquid crystal insertion.[60-63] To attain chiral lasing, Jiang et al. prepared $CsPbCl_xBr_{3-x}$ MW using a one-step rapid anti-solvent induced recrystallization method.[58] The rectangular cross-section of halide perovskite MW supports whispering gallery mode (WGM) microcavities, achieving a Q factor of up to 3017, enabling low-threshold (81.8 μJ cm^{-2}) single-mode lasing. Further, the MW is assembled with the encapsulated cholesteric liquid crystal (CLC) layer (**Figure 2.8a**) for achieving chiral lasing. By utilizing the helical photonic crystal structure of CLC, the linearly polarized laser can be converted to circularly polarized laser. By adjusting the photonic bandgap (PBG) of CLC to match the emission wavelength of halide perovskites, a significant enhancement in the dissymmetry factor ($g_{lum}\approx1.62$) is achieved as shown in **Figure 2.8b**. This work utilizes the high quality (Q) factor of WGM microcavities and the selective reflection mechanism of CLC to establish a new paradigm for chiral lasing devices. Meanwhile, it addresses key challenges in chiral laser technology, such as high g_{lum}, tunability, and stability, through the innovative combination of perovskite MW with CLC layers. Under high pump conditions generated by lasers, the electron-hole exchange interaction (Bir-Aronov-Pikus, BAP mechanism) becomes the dominant factor in spin relaxation in perovskites, making it difficult to maintain spin polarization. Zhao et al. utilize Mn^{2+} doping to suppress the electron-hole exchange interaction (**Figure 2.8c**), achieving spin-polarized laser emission for the first time in halide perovskites with a circular polarization degree (DCP) of 27.3%.[59] Moreover, utilizing the magnetism of Mn^{2+}, the CPL laser emission can be modulated by an external magnetic field (**Figure 2.8d**), and DCP (10%-40%) can be dynamically regulated through an magnetic field (±0.5 T). This work reveals the photophysical mechanisms of spin relaxation in perovskites and proposes a universal ion doping strategy (such as Mn^{2+}, Co^{2+}, etc.) to regulate spin properties for obtaining chiral lasing. Direct CHP amplified spontaneous emission (ASE) represents a promising pathway toward low-threshold, spin-polarized lasing due to its intrinsic chirality and high optical gain. The fabrication of CHP nanostructures further enhances this potential by leveraging advanced optical cavities, such as WGM, Fabry-Perot (FP), and distributed feedback (DFB) configurations, to achieve efficient light confinement and feedback. For example, WGM cavities exploit the ultrahigh Q factors of CHP microdisks or microspheres to enable ultralow threshold lasing with circularly polarized outputs. FP cavities allow wavelength-tunable chiral lasing through cavity-length modulation, though requiring additional chiral mirrors for polarization selectivity. DFB cavities integrate periodic nanostructures (e.g., chiral gratings) to directly couple CHP’s spin-dependent gain with resonant modes, achieving high polarization purity. Despite these theoretical advantages, experimental demonstrations of CHP-based chiral lasers remain limited. Key challenges include optimizing material stability under optical/electrical pumping, enhancing the dissymmetry factor of ASE, and achieving scalable integration of chiral nanostructures with photonic cavities.

2.4.4 Second harmonic generation

SHG technology with frequency conversion and polarization sensitivity features finds widespread applications in various fields such as imaging, communication, and energy. The generation of SHG depends on materials with a non-centrosymmetric crystal structure. CHPs fulfill the requirement by incorporating chiral organic molecules, such as R/S-MBA or chiral amines, which disrupt the lattice symmetry. This disruption induces helical or layered chiral arrangements that satisfy the phase-matching conditions essential for efficient SHG. A synergistic interaction between these chiral ligands and inorganic frameworks, such as lead halide $[PbX_6]^{4-}$ octahedra, enhances the asymmetric distribution of electron clouds, thereby amplifying the second-order nonlinear polarization. Furthermore, chiral structures enable circularly polarized second harmonic generation (CP-SHG), where the asymmetry factor is determined by the spatial arrangement of chiral molecules and their exciton-photon coupling strength. This phenomenon unlocks novel opportunities in advanced applications like chiroptical encoding and quantum communication technologies.

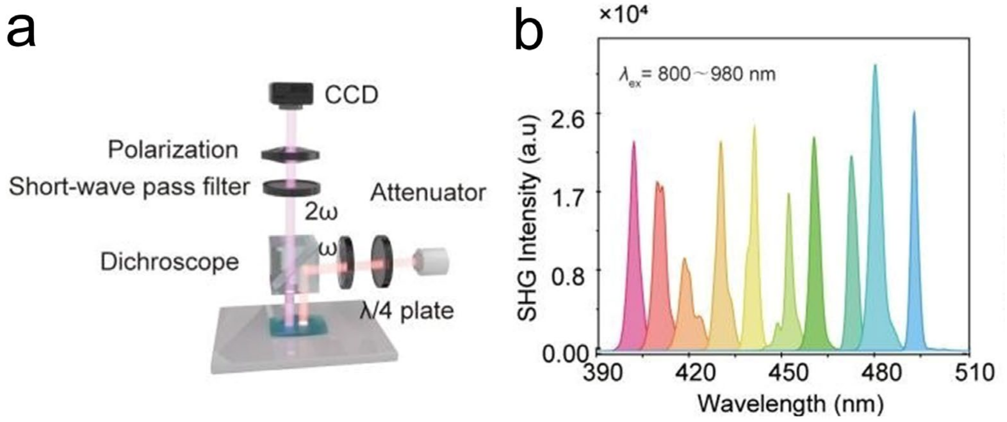

Figure 2.9 Emerging SHG application based on CHP. (a) Micro-area nonlinear optical characterization system. (b) SHG intensity of CHP at different wavelengths.[64]

Long and coworkers pioneered the first chiral non-metallic perovskite, (R/S-MBA)$_6$Cl(NH$_4$Cl$_6$), where chirality arises from the helical stacking of α-methylbenzyl ammonium (MBA$^+$).[64] This inverse perovskite architecture, featuring anionic A/B sites and a cationic X site, overcomes limitations inherent to conventional perovskites such as metal ion toxicity, high production costs, and low laser damage thresholds (LDTs). A custom-built micro-area nonlinear optical (NLO) characterization system employing reflective collection mode (**Figure 2.9a**) revealed a broadband SHG response across 800-980 nm excitation wavelengths (**Figure 2.9b**), achieving a second-order nonlinear coefficient (deff) of 0.89

pm/V. This performance exceeds commercial Y-cut quartz (0.3-0.5 pm/V) and numerous Cd/Cu-containing chiral perovskite systems. The material demonstrates remarkable SHG circular dichroism asymmetry ($g_{SHG-CD} = 0.60$), signifying pronounced nonlinear chiroptical activity suitable for polarization modulation and chiral sensing. Moreover, the LDT reaches 71 mJ/cm^2, surpassing that of most reported CHP, attributed to the wide transparent optical window (300-1000 nm) of the material and the low optical absorption of its organic components, positioning it for high-power laser and quantum optics applications.

2.4.5 Spintronics

Spintronic applications depend critically on precise control of electron spin states, necessitating materials capable of efficient spin injection, transport, and detection. The CISS effect observed in CHPs provides a novel mechanism for achieving spin polarization without requiring external magnetic fields. Furthermore, CHPs can be processed via solution-based methods, enabling compatibility with flexible electronics and large-scale device integration.

To investigate the magneto-optical activities in CHP, Maiti et al. synthesized (R/S-MBA)$_4$Bi$_2$Br$_{10}$, where the inorganic [Bi$_2$Br$_{10}$]$^{4-}$ dimer coordinates with chiral organic cations to form a non-centrosymmetric 0D structure (space group P2$_1$).[65] The dimension increases the density of chiral ligands, thereby boosting the CISS effect. Substituting bismuth for lead reduces environmental toxicity while retaining SOC. The synergistic effect of CISS and the optical selection rule was inspected for spin carrier dynamics. Vertical transport measurements by mc-AFM (**Figure 2.10a**) demonstrate spin-selective behavior: R-perovskite exhibits higher current under an up-magnetized probe (spin polarization degree = 78%, **Figure 2.10b**), while S-perovskite shows the opposite trend (84% polarization), directly confirming chirality-dependent spin filtering.

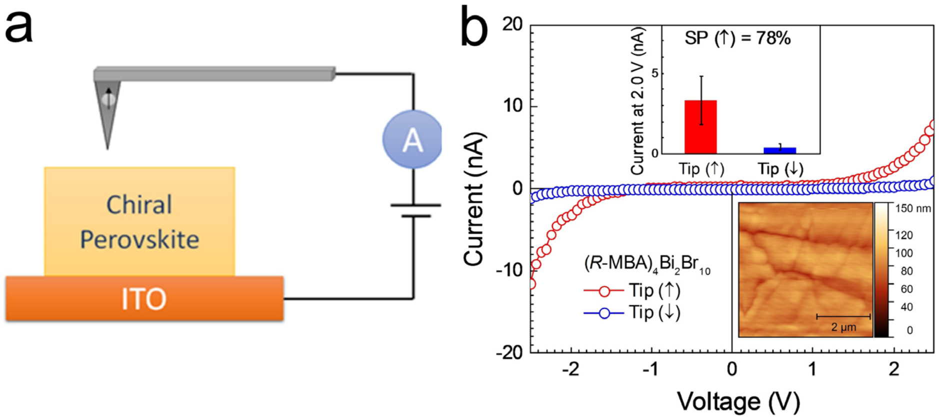

Figure 2.10 Spintronics. (a) Sketch for the mc-AFM measurement of CHP. (b) Current response of CHP/ITO under different tip magnetization.[65]

According to the optical selection rule, LCP transfers angular momentum (Jz=−*ħ*) to electrons, exciting 67% spin-up (m_j=+1/2) and 33% spin-down (mj=−1/2) carriers in the conduction band. Conversely, RCP (Jz=+*ħ*) generates 67% spin-down and 33% spin-up populations. In this work, CISS enhances the anisotropy, and serves as an important role for achieving efficient CPL detection. Optical selection rules ensure the generation of charge carriers with different spin polarizations under CPL irradiation. CHP acts as a spin filter, permitting only charge carriers with specific spin orientations (such as R-type perovskite transmitting spin-up and S-type perovskite transmitting spin-down) to pass through. This mechanism lays a theoretical foundation for the development of efficient and eco-friendly spin-optoelectronic devices.

Chapter 3 Chiral Halide Perovskite Film for CPL-resolved UV Photonic Artificial Synapse

3.1 Introduction

More than 80% of the intellectual information input to the human brain is acquired by vision, which makes the visual system one of the most important sensory modalities. Typical visual systems consist of the retina for receiving light signals and the visual cortex for parallel visual cognition.[66-68] In the visual system, the retina performs preliminary processing of visual information by simplifying the image through a temporal encoding method before transmitting the signals to the visual cortex, and this neuromorphic feature contributes to high efficiency and low power consumption.[69-71] Inspired by the human visual system, photonic artificial synapse (PAS) devices with intrinsic neuromorphic characteristics trigger considerable research interest and are widely investigated in the field of machine vision.[72-74] However, most PAS devices are only sensitive to color (wavelengths) and intensity of light while lacking the capability of detecting circular polarization which has great potential in remote sensing, substance screening, optical communication, and object identification[27, 75]. Hybrid integration techniques that combine the polarizers with photosensitive devices have been developed to solve this problem, but this solution suffers from high hardware costs and bulkiness.[11, 76-77] Developing CPL-sensitive PAS devices shows great significance in simplifying the polarization-dependent vision systems.

Chiral materials with CD, such as chiral perovskites, chiral organic molecules, and metal-organic frameworks construct the material foundation for directly detecting CPL and identifying its handedness, including LCP and RCP.[78-80] Among those chiral materials, chiral perovskites inherit chirality from intentionally introduced chiral molecules, such as α-Methylbenzylamine enantiomers (α-MBA), β-Methylphenethylammonium (β-MPA), 1-Cyclohexylethylammonium (CHEA), etc., and show superior chiroptical properties[81-83]. Specifically, helical one-dimensional chiral perovskite (H-PVK) exhibits relatively high circular dichroic response owing to the strong light-matter interaction between chiral ligands and BX_6^{4-} matrix (B = Pb, Sn, Ge; X = I, Br, Cl).[17, 84-85] However, the H-PVK materials suffer low conductivity, which discounts their chiroptical performance in CPL sensing applications. Combining H-PVK with high-mobility semiconductors can promote the transfer of photoinduced carriers and circumvent poor carrier transport.[86-87] Exploration of H-PVK-based heterostructure and underlying carrier dynamics shows great significance in constructing circular polarization sensing PAS devices.

In this work, we showcase two kinds of heterobilayer composed of H-PVKs (1D-R and 1D-S) and single-wall carbon nanotubes (SWNTs) and utilize the heterostructure to build CPL-modulated PAS devices. The heterostructures exhibit excellent polarization-dependent photoresponsivity, and are capable of distinguishing LCP and RCP. To study the carrier dynamics and chiroptical properties, the TA of H-PVK/SWNTs is investigated using femtosecond pump-probe spectroscopy, and the detected fast decay process combined with energy band analysis demonstrates the hole transfer existing in the heterostructure, which contributes to a bioinspired PAS. A series of synaptic activities is demonstrated on the PAS device. More importantly, the PAS-based spike neural networks (SNNs) are simulated and exhibit a high accuracy up to 93%. The proposed heterobilayer PAS exhibits great potentiality in building CPL-modulated neuromorphic vision systems with high visual contrast, giving rise to new paradigms in object identification, autonomous navigation, and machine vision.

3.2 Experimental section

Materials

R-(+)-α-Methylbenzylamine (≥ 99.0%), S-(-)-α-Methylbenzylamine (≥ 99.0%), N, N-dimethylformamide (DMF, 99.5%), Toluene (anhydrous, 99.8%), Fifty-seven percent aqueous and hydriodic acid (HI) solution (99.95%) were purchased from Sigma-Aldrich. Lead oxide (PbO, 99.9%) was purchased from Alfa Aesar. The raw arc-discharge CNT (AP-SWNT, ≥ 60%) was purchased from Carbon Solution Inc. The dispersant 9-(1-octylonoyl)-9H-carbazole-2,7-diyl (PCz) was prepared by Suzuki polycondensation in a relatively high yield.

Synthesis of (R- and S-α-MBA)I precursors: The precursors (*R*-*α*-MBA)PbI and (S-*α*-MBA)PbI were synthesized by mixing HI with the chiral amines (*R*- and *S*-MBA) in 1:1 molar ratio. First, 5.3 ml (0.0416 mol) ammine was dissolved in 20 ml methanol, to which the 5 ml (0.0416 mol) HI was added dropwise within 15 min, and the mixture was stirred at 0 °C for 2 hours. Then the solvent was removed by rotary evaporation to yield the (*R*- and *S*-α-MBA)PbI white powder. Finally, the powder was collected and washed by diethyl ether followed by drying in the vacuum overnight.

Synthesis of H-VPK: The (*R*- and *S*-*α*-MBA)I templated by different α-methylbenzylamine enantiomers and PbI_2 with an equal molar ratio were dissolved into DMF to obtain the 1D-

R/1D-S, and the solution concentration is controlled at 0.3 mol L^{-1}.

Sample characterization

X-ray diffraction characterization was performed by Rigaku SmartLab with monochromatized Cu Kα radiation ($\lambda = 1.54$ Å). The surface morphology of the PAS device was characterized by a field-emission scanning electron microscope (Tescan MAIA3) and Scanning Probe Microscope (Asylum MFP-3D Infinity). The thickness of the H-PVK was measured by Bruker DektakXT Surface Profiler. The ultraviolet photoelectron spectroscopy data was measured by a Thermo Scientific Nexsa instrument.

Device measurement

The electrical measurement of PAS devices was performed in the Lake Shore probe station equipped with a semiconductor analyzer (Keithley 4200-SCS). Chiroptic measurement was performed using the polarizers and LEDs with different wavelengths purchased from Thorlabs. The intensity of CPL was calibrated by a standard optical power meter (Newport 843-R with a PD300-UV optical power detector) before each measurement. All the measurements were performed in an air atmosphere at room temperature.

Simulation of neural networks

The SNNs were composed of 748 input neurons, 200 hidden neurons and 10 output neurons. Before the training, the MNIST dataset was converted into a time-varying sequence of spikes by transforming the image pixel as a discrete value $X_{i,j} \in \{0, 1\}$. In the training, the weighted sum contributed to the neuron membrane potential $U(t)$. When the neuron was sufficiently excited by the weighted sum, the membrane potential reached a threshold θ, and then the neuron emitted a spike to its subsequent connections. The training utilized 60000 training and 10000 test images with a batch size of 200 at each epoch. After 300 epochs, the recognition accuracy was calculated for evaluation.

Optical spectroscopy

TA spectroscopy was measured with an amplified titanium: sapphire femtosecond laser (50 fs, Coherent Libra) with a wavelength of 800 nm and repetition of 1 kHz and a Helios pump-probe setup (Ultrafast Systems) which has a minimum step feature of 2.8 fs. Raman spectra pattern was obtained using the WITEC alpha300 R- Raman imaging microscope. The CD was characterized by a CD spectrometer (JASCO J-1500 Easton, MD, USA) at room temperature. The data pitch was 1 nm, and the scan rate was 100 nm per minute.

3.3 Result and discussion

3.3.1 Device fabrication

As shown in **Figure 3.1**, the wafer with a 300 nm thick oxide layer was utilized as substrate, and was washed ultrasonically by acetone, ethanol, and distilled water for 15 min in turn. After that, the substrate was treated with UV-ozone plasma for 10 min. The SWNTs film was deposited by soaking the substrate in the semiconducting SWNTs solution for 24 h, followed by heating at 120 °C for 15 min. The electrodes (5 nm Ti/45 nm Au) were defined by typical photolithography, electron-beam evaporation, and a lift-off process. Thin chiral perovskite film was obtained by spin coating the H-PVK solution onto the patterned substrate with a spin rate of 4000 rpm for 30 s, followed by annealing at 95 °C for 15 min.

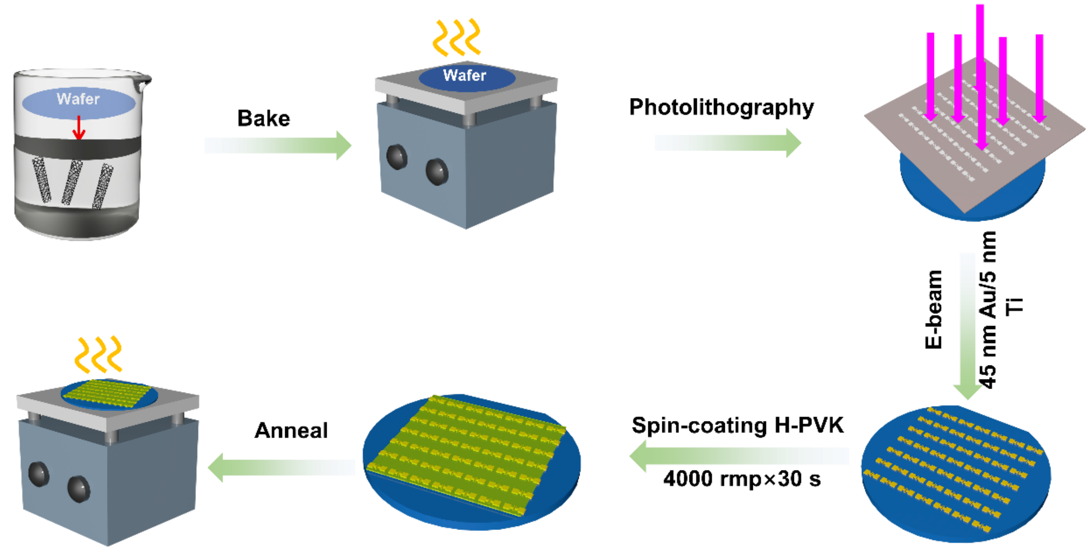

Figure 3.1 Sketch process for the preparation of two-terminal H-PVK/SWNTs heterobilayer devices.

3.3.2 Characterization of H-PVK/SWNT heterostructure

To create a CPL-sensitive absorber in our PAS device, we fabricated chiral perovskite H-PVKs and their heterostructures with a SWNTs layer. The choice of a 1D chiral halide perovskite was motivated by its excellent chiroptical performance in the UV region. SWNTs, known for their high mobility and widespread use as hole extraction layers in perovskite solar cells, were selected as the charge-transporting layer in our devices. We synthesized chiral 1D (S-α-MBA)PbI_3 (referred to as 1D-S) and (R-α-MBA)PbI_3 (referred to as 1D-R) using left-handed (S-α-MBA) and right-handed (R-α-MBA) enantiomers, respectively. The crystal structures of the 1D-S and 1D-R perovskites, illustrated in **Figure 3.2a**, exhibit chiral properties. X-ray diffraction measurements confirmed the high quality of the thin films of H-PVK, with a thickness of approximately 70 nm. Surface profiler and atomic force microscope (AFM) measurements further confirmed the desirable morphology of the films

(**Figure 3.2b–c**). Both 1D-R and 1D-S perovskites demonstrated intense excitonic absorption at 375 nm (**Figure 3.2d**), but with opposite CD signals at the same wavelength. This observation indicates that the distinction between the two heterojunctions arises from the corresponding S and R enantiomers of MBA. The 1D-R and 1D-S films displayed high discrimination, characterized by optical anisotropy factors of CD (g_{CD}) reaching 0.01 at transitions around 340 nm (**Figure 3.2e**). Clear observation of G bands (G^+ and G^-) and D bands from Raman spectroscopy (**Figure 3.2f**) suggests the successful transfer of semiconducting SWNTs onto the Si substrate. Overall, our fabrication process successfully produced the CPL-sensitive absorber in the PAS device, utilizing chiral perovskite H-PVKs and their heterostructures with SWNTs. The high-quality films and the distinctive optical properties of the 1D-R and 1D-S perovskites lay a solid foundation for the enhanced CPL-modulated performance of our devices.

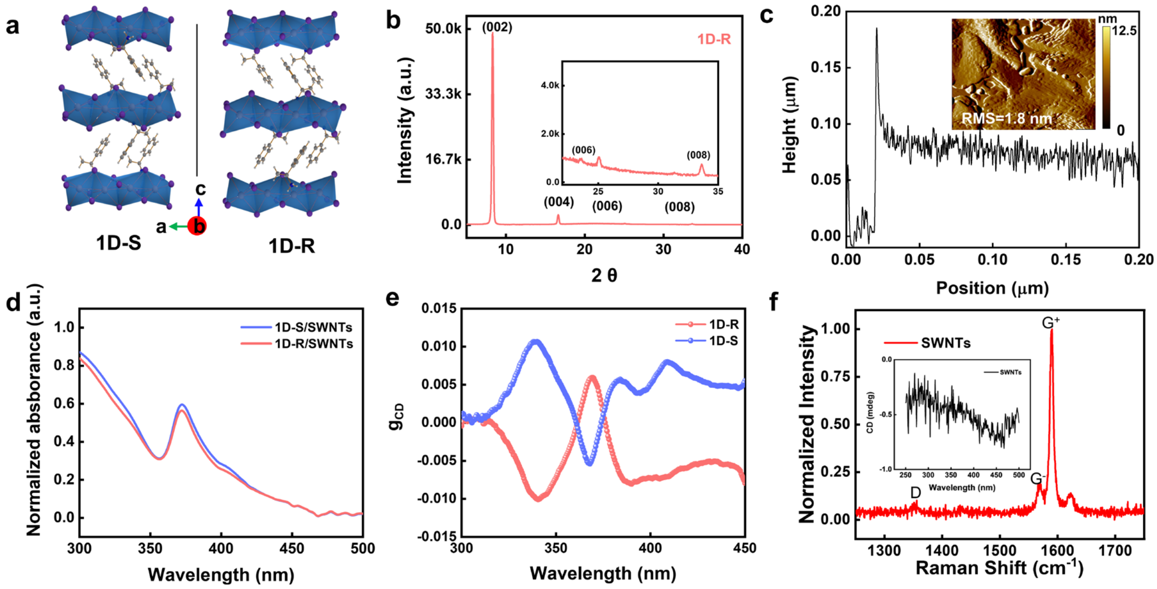

Figure 3.2 (a) Crystal structure of 1D-S and 1D-R from the view along the *b* direction. (b) XRD patterns of 1D-R film. (c) Thickness of H-PVK measured by surface profiler. Inset shows the AFM image of spin-coating H-PVK. (d) Absorbance spectra of H-PVK/SWNTs.

(e) The g_{CD} spectra of 1D-R and 1D-S films. (f) Raman spectra of SWNT. Inset is the CD spectra of SWNT.

3.3.3 Circular polarization-resolved UV photodetection

Figure 3.3a illustrates the schematic of the two-terminal PAS device. Generally, the SWNTs film is deposited by immersing the SiO_2/Si substrate in a solution of semiconducting SWNTs, followed by a heating process. The electrodes (consisting of a 45 nm layer of gold and a 5 nm layer of titanium) are then patterned using photolithography, electron-beam evaporation, and a lift-off process. Optical and SEM images demonstrate the uniformity of the patterned electrodes with sparsely distributed SWNTs in the channel. After the electrode deposition, the H-PVK film is spin-coated onto the patterned substrate, followed by an annealing process. The band alignments of the materials are determined using ultraviolet photoelectron spectroscopy and UV-Vis measurements. Upon contact between H-PVK and SWNTs, an interfacial band bending occurs, resulting in a potential barrier of 0.7 eV (**Figure 3.3b**). This potential barrier facilitates the transfer of photoexcited holes from H-PVK to SWNTs, while repelling the photoexcited electrons. Importantly, the 1D-R/SWNTs and 1D-S/SWNTs heterostructures exhibit symmetrical CD signals in the UV region (**Figure 3.3c**). Pristine SWNT networks, on the other hand, do not display any CD signal. These observations indicate that the chirality primarily originates from the 1D-S and 1D-R components. Consequently, these chiral heterostructures, 1D-R/SWNTs, and 1D-S/SWNTs, are employed as CPL-sensitive materials in the subsequent development of chiroptoelectronic and neuromorphic vision devices.

To assess the chiroptoelectronic performance, we conducted photoresponse measurements on the heterostructure under CPL illumination with varying handedness, wavelengths, and intensities. As depicted in **Figure 3.3d**, the 1D-S/SWNTs device exhibited a distinct photoresponse under both types of CPL illumination, surpassing the performance of previously reported chiral perovskite-based photodetectors. This superior photoresponse contributes to the development of high-performance chiroptical electronics. **Figure 3.3e** presents the photoresponsivity of the device under CPL illumination at different wavelengths. The results reveal a relatively higher responsivity, peaking at around 400 nm, consistent with the chiroptical absorption characteristics of the H-PVK layer. In **Figure 3.3f**, we display the light intensity-photoresponse relationship, demonstrating that the 1D-S/SWNTs device exhibits a remarkable responsivity exceeding 240 mA W^{-1} under LCP illumination with an incident power of 1 μW cm^{-2}. This indicates its exceptional sensitivity in detecting weak CPL. Similarly, the 1D-R/SWNTs device demonstrates comparable photoelectric performance but displays higher responsivity under RCP illumination. Furthermore, the constructed heterostructures exhibit outstanding stability, showing negligible degradation even after over one month of ambient storage. The chiroptoelectronic characteristics observed in our chiral perovskite heterostructure device highlight its immense potential for applications in CPL-resolved vision.

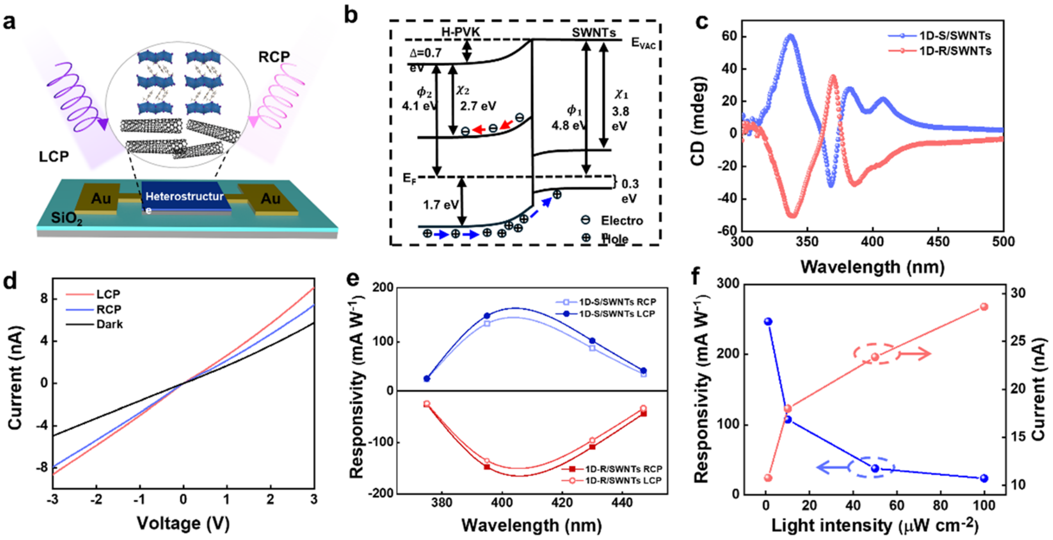

Figure 3.3 Chiral optoelectronic characterization of perovskite heterostructure. (a) Structural scheme of the in-plane 1D-S/SWNTs heterostructure device. (b) Energy band diagrams of H-PVK and SWNTs. (c) CD spectra of H-PVK (1D-R, 1D-S)/SWNTs heterostructure. (d) Current-voltage curves of 1D-S/SWNTs heterostructure under dark, LCP and RCP (395 nm, 10 μW cm^{-2}) illumination. (e) Responsivity of H-PVK/SWNTs under RCP and LCP at the wavelengths of 375 nm, 395 nm, 430 nm and 447 nm (10 μW cm^{-2}). (f) Dependence of photocurrent and responsivity versus incident LCP of different intensities at 395 nm.

3.3.4 Mechanism of CPL-dependent photocurrent generation

To gain a deeper understanding of the photophysical mechanism of the CPL-sensitive H-PVK/SWNTs heterostructure device and its potential for use in optical synaptic activity, we conducted polarization-dependent carrier dynamics measurement with the assistance of ultrafast TA system (**Figure 3.4a**) and performed DFT calculations. The schematic diagram in **Figure 3.4b** illustrates the experimental setup where CPL serves as the pump signal, and linear polarized light is used to probe the carrier population dynamics. Under pump excitation, photoexcited holes can transfer from H-PVK to the surface-attached SWNTs. For DFT calculations, we established a molecule model of the 1D-S/SWNTs heterostructure, as shown in **Figure 3.4c**. The calculated projected density of states (PDOS) of SWNTs and 1D-S perovskite is presented in **Figure 3.4d**. The highest occupied molecular orbital (HOMO) of SWNTs is higher than the VBM of 1D-S, consistent with **Figure 3.3c**. This alignment promotes the transfer of holes toward the SWNTs layer. A similar charge transfer process is observed in the 1D-R/SWNTs heterostructure.

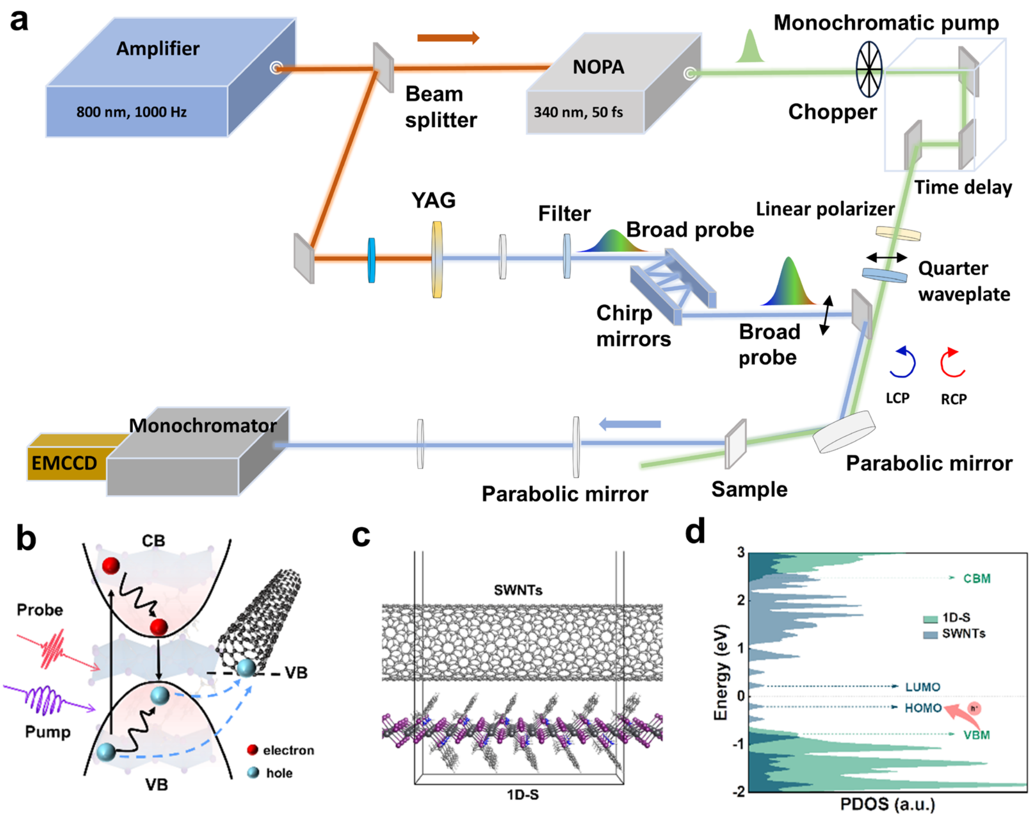

Figure 3.4 CPL-dependent charge transfer dynamics and storage. (a). Ultrafast TA system. noncollinear optical parametric amplifier (NOPA), electron-multiplying charge-coupled device (EMCCD). (b) Sketch illustration of carrier relaxation dynamics in SWNTs/H-PVK heterojunction. CB, conduction band; VB, valence band. (c), (d) Optimized interfacial

structures, and corresponding PDOS for SWNTs/1D-S.

Figure 3.5a displays the pseudo-color plot of TA spectra of 1D-S and 1D-S/SWNTs excited by a 340 nm LCP femtosecond (fs) laser beam. Under CPL excitation, a photobleaching (PB) band at around 375 nm is observed, resulting from the state filling of excitonic states in H-PVK. The 1D-S perovskite exhibits a long exciton lifetime ($\tau_{1D\text{-}S}$) of more than 16 ns. In the 1D-S/SWNTs heterostructure, a noticeable PB quenching is observed, along with an additional fast decay with a lifetime ($\tau_{1D\text{-}S/SWNTs}$) of around 2 ns (**Figure 3.5b**). The reduction in PB signal is attributed to the transfer of photoexcited holes from 1D-S into the SWNTs network. The hole injection efficiency (η_i) from 1D-S to SWNTs is estimated to be approximately 72% (using η_i=1- $\tau_{1D\text{-}S/SWNTs}/\tau_{1D\text{-}S}$) under LCP illumination. Compared to LCP excitation, RCP light results in a smaller η_i of 60% due to the lower photoresponse of RCP by 1D-S perovskite. **Figure 3.5c** illustrates the energy band variation of H-PVK and the heterostructure under multiple CPL pulse illuminations. For H-PVK alone, when the CPL beam is off, the excited excitons rapidly recombine within its lifetime of tens of ns (upper panel left). Therefore, there is no difference when the next CPL pulse arrives (upper panel right). In the heterostructure (lower panel left), the excitons can effectively dissociate at the interface after excitation, with electrons captured by trap states inside H-PVK and holes transferred into SWNTs, reducing the possibility of recombination. As a result, the hole density in SWNTs can increase after multiple pulse excitation, leading to an increased photocurrent for PAS applications.

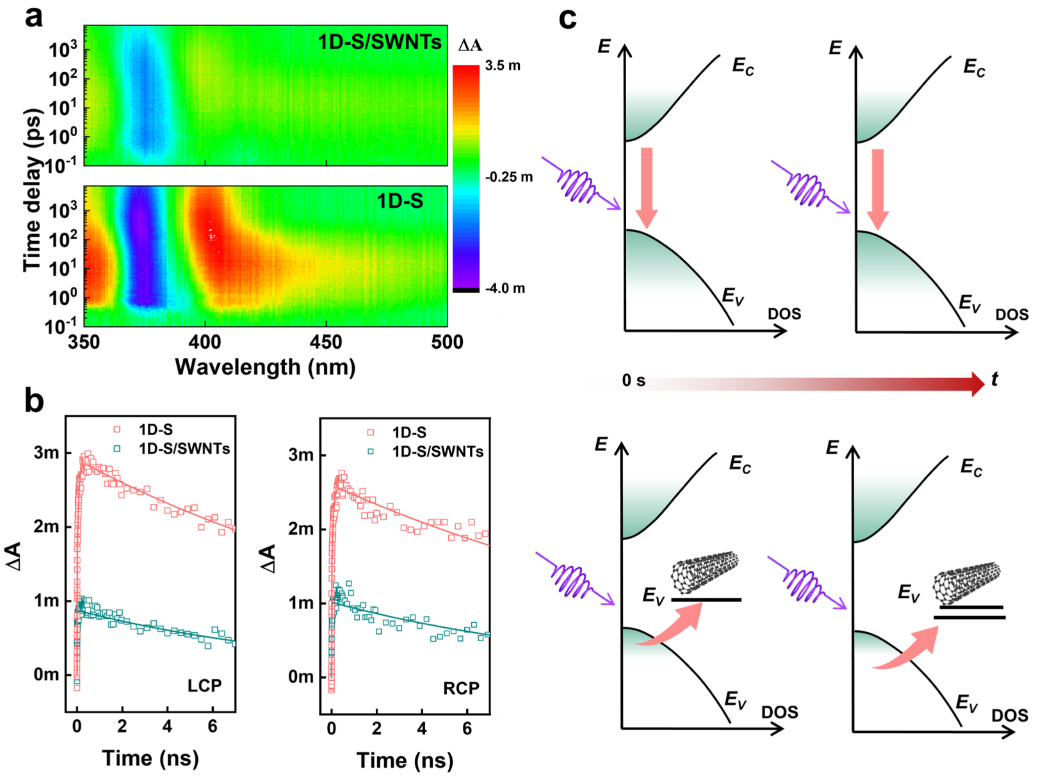

Figure 3.5 TA carrier dynamics and energy band analysis. (a) Time-resolved TA mapping of H-PVK and 1D-S/SWNTs measured with LCP pump beam. The pump power intensity is 90 uW cm^{-2} (b) Ground-state bleaching (GSB) dynamics of 1D-S and 1D-S/SWNTs under 395 nm LCP, RCP excitation pump beam. (c) The variation of the band structure versus CPL illumination time.

To validate the above assumption, we monitored the change in TA signal (ΔΔA) as a function of laser pulse numbers. The initial TA signal was set at around 5 ns when the holes had transferred into SWNTs. As shown in **Figures 3.6a** and **3.6b**, during the stimuli with 1 kHz fs laser pulse spikes, the ΔΔA signal, which reflects the carrier population, remained almost unchanged over time for 1D-S alone, consistent with the optoelectronic performance of the 1D-S-based device. In contrast, the ΔΔA of the 1D-S/SWNTs heterostructure (lower panel) exhibited an increasing trend with the increasing pump pulse numbers, indicating the effective separation of electrons and holes at the heterostructure interface. This characteristic contributes to the construction of artificial synapses with high biological plausibility. Additionally, the 1D-R/SWNTs heterostructure demonstrated a higher response under RCP pump illumination. These results highlight the CPL polarization preference features and memory functions in the heterostructure for PAS devices.

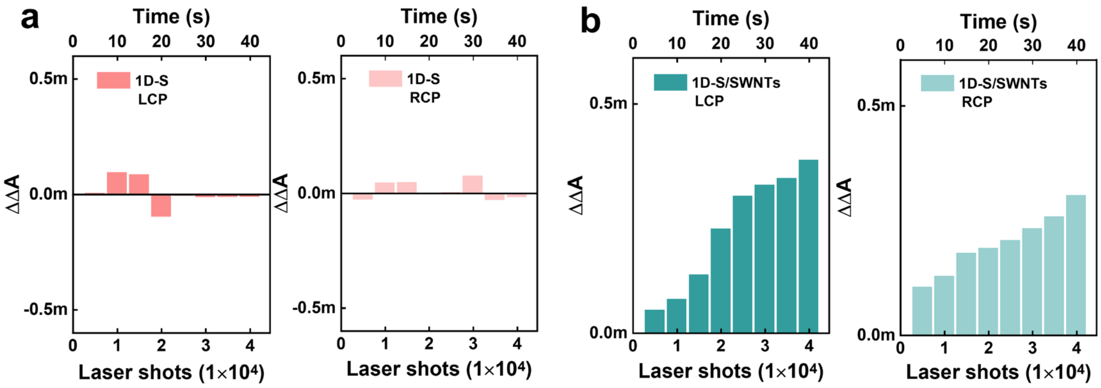

Figure 3.6 TA signals pumped by laser spikes. (a) Spike-timing dependent carrier dynamics of 1D-S around 5 ns observed by ultrafast femtosecond pump-probe spectroscopy. (b) Carrier dynamic of 1D-S/SWNTs.

3.3.5 Circular polarization-dependent synaptic activities

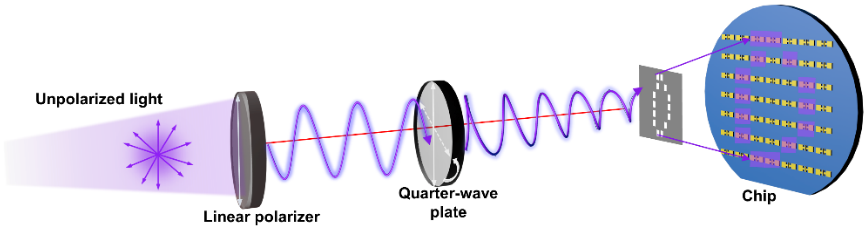

Figure 3.7 Schematic diagram of optical setups for the CPL sensing measurement.

The PAS device accurately imitates a series of synaptic plasticity in the retina in response to CPL stimuli. **Figure 3.7** illustrates the optical setup used to test. After passing through the linear polarizer and quarter waveplate, the light spikes result in the generation of CPL spikes.

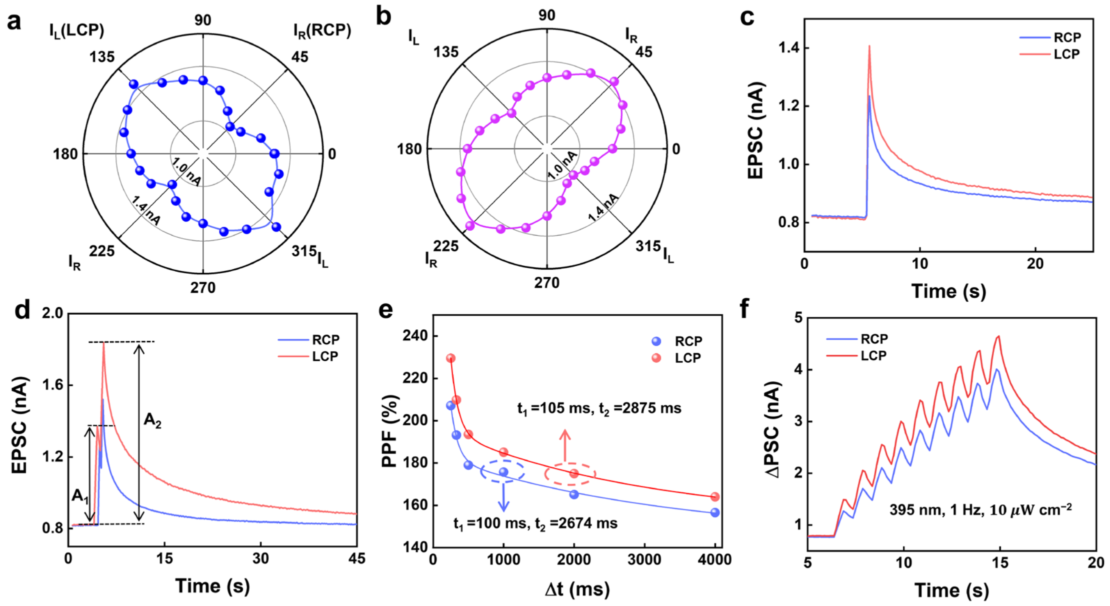

Figure 3.8 Circular polarization-dependent synapse activities. (a), (b) Polar plots of the polarization dependence of the response current of 1D-S/SWNTs and 1D-R/SWNTs based PAS. (c) Transient EPSC of PAS device in response to single LCP and RCP (395 nm, 10 μW cm^{-2}). (d) EPSC induced by a pair of LCP/RCP spikes (395 nm, 10 μW cm^{-2}) with the interval of 1 s. (e) Variation of PPF index with the increase of excitatory stimuli interval. (f) EPSC of 1D-S based PAS excited by consecutive LCP and RCP spikes.

The photocurrent of the 1D-S/SWNTs (**Figure 3.8a**) and 1D-R/SWNTs (**Figure 3.8b**) heterostructure PAS devices exhibits a clear relationship with the ellipticity of the incident beam. This enables precise differentiation of incident CPL (395 nm, 10 μW cm^{-2}) and allows for the modulation of synaptic plasticity in the PAS device based on the degree of circular polarization. Due to the chiroptic symmetry features of 1D-S/SWNTs and 1D-R/SWNTs, we focus on presenting the CPL-induced synaptic activities of the 1D-S/SWNTs-based PAS device in detail. **Figure 3.8c** demonstrates that a single LCP/RCP spike triggers an EPSC, and the gap between the peak EPSC values indicates that the PAS device can respond differently to CPL stimuli with opposite circular polarizations, generating corresponding EPSC responses. The 1D-S/SWNTs PAS device exhibits a 1.2 times higher EPSC response under the modulation of LCP spikes compared to RCP excitation, demonstrating the CPL-resolved synaptic behavior. Furthermore, the PAS device imitates paired-pulse facilitation (PPF), a critical characteristic of STP. PPF is related to the temporal encoding/decoding of visual information, as reflected by an increase in the postsynaptic response A_2 after the second spike compared to the initial response A_1. **Figure 3.8d** shows the PPF behavior triggered by two CPL spikes with a duration of 500 ms and intensity of 10 μW cm^{-2}. The increment of A_2 typically depends on the time interval (Δt) between the two spikes, which can be described by the PPF index of A_2/A_1. A larger PPF index leads to higher temporal resolution for efficient and accurate processing of temporal information. As depicted in **Figure 3.8e**, the PPF index decays slowly with increasing Δt, and LCP-induced PPF exhibits a higher PPF index of up to approximately 230% with a slightly longer lifetime ($PPF = C_1 e^{\frac{-\Delta t}{t_1}} + C_2 e^{\frac{-\Delta t}{t_2}}$). This could be attributed to the suppressed generation of electron-hole pairs under RCP illumination in 1D-S. In addition to STP, the LTP characteristic is investigated by applying consecutive CPL spikes to the PAS device in a train of nine CPL spikes (**Figure 3.8f**). Evidently, the 1D-S/SWNTs PAS device exhibits a step-by-step increase in EPSC values under consecutive CPL spikes, indicating an enhanced strength of synaptic plasticity with repeated learning. Furthermore, CPL at other wavelengths (375 nm, 430 nm, and 447 nm) can also induce LTP behaviors, albeit with smaller differences under different polarization spikes, which align with their lower CD signals.

Our PAS device offers flexible tuning of synaptic plasticity strength by encoding CPL spikes with various parameters such as the number of spikes, wavelength, intensity, frequency, and polarization. This enables the device to support multiple learning and memory functions. In **Figure 3.9a**, we observe that applying two LCP spikes (1 Hz, 10 μW cm^{-2}) to the 1D-S/SWNTs-based PAS results in the decay of EPSC strength to 1 nA within 60 seconds, indicating short-term potentiation (STP). When the number of stimuli spikes is increased to nine, the decay of EPSC response takes a longer time (120 seconds), indicative of long-term potentiation (LTP) behavior. **Figure 3.9b** summarizes the CPL spike number-dependent EPSC ratio (A_n/A_1). The rate of growth of A_n/A_1 slows down and eventually reaches a maximum value of 648%, indicating a transition from STP to LTP. This transition may be attributed to the limited hole-trapping sites in SWNTs and carrier lifetimes. In **Figure 3.9c**, we observe that the PAS device exhibits peak current responses of 1.75, 2.64, and 4.18 nA under three different wavelengths, while it does not respond to 532 nm, indicating superior UV plasticity behavior. **Figure 3.9d** demonstrates the CPL intensity-dependent EPSC behavior, showing a stronger EPSC response with slower decay at higher intensity. Furthermore, in spike-frequency-dependent plasticity (SFDP) as shown in **Figure 3.9e**, a larger EPSC value with slower decay can be observed at high spike frequencies. This observation aligns with the concept that multiple stimuli in a short time can enhance learning and memory in organisms. The relationship between memory retention and time follows the Ebbinghaus forgetting curves.

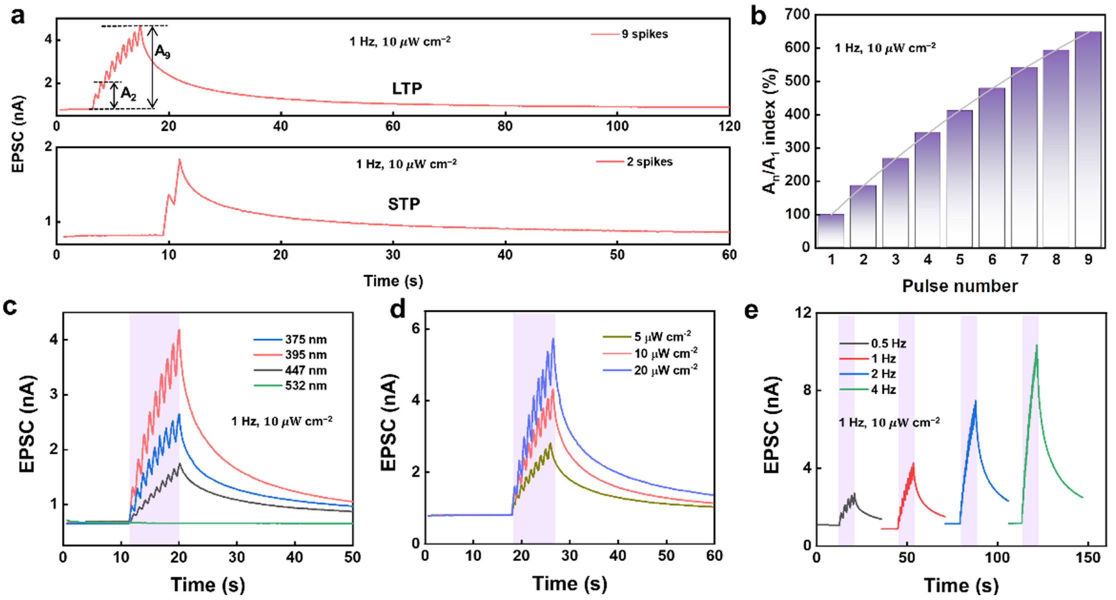

Figure 3.9 Tunable CPL synaptic characteristics. (a) LTP and STP under 9 and 2 spikes. (b) Variation of A_n/A_1 index with increasing LCP pulse number. (c) EPSCs in response to multiple LCP pulses under 375, 395, 430 and 447 nm. (d) EPSC in response to 395 nm LCP with different power intensities and a fixed frequency of 1 Hz. (e) Spike-frequency-dependent EPSC triggered by a sequence of nine LCP spikes.

Repeating the learning process accompanied by forgetting experiences (**Figure 3.10a**) can lead to the conversion of short-term memory (STM) into long-term memory (LTM). In this experiment (**Figure 3.10b**), the gray dashed line represents the target level of learning, and the PAS device is exposed to two types of 395 nm CPL to study polarization-dependent learnability. Under LCP illumination, it takes 9.4 seconds for the 1D-S/SWNTs PAS device to initially reach the target level, while subsequent re-learning processes only require 5.4 seconds to recover all the cognition. However, under RCP with the same intensity and Δt, the PAS device exhibits a relatively low EPSC value (green dashed line) and weak learnability.

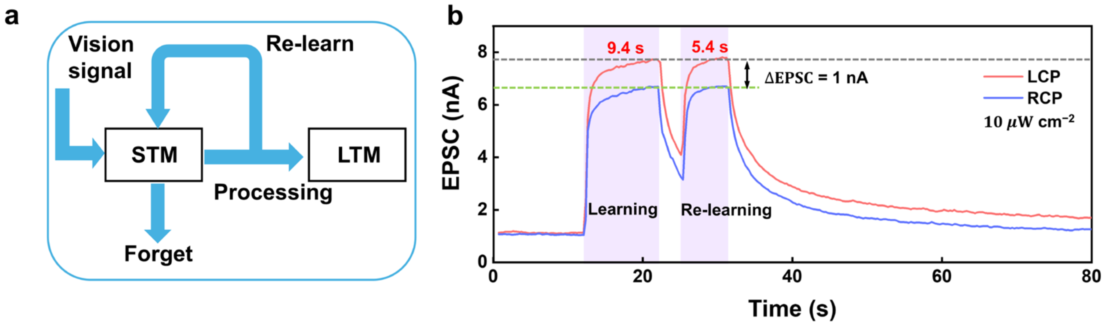

Figure 3.10 Memory process. (a) Learning and memory process in neuromorphic vision system. (b) Learning-experience behavior imitated by this PAS device under LCP and RCP illumination.

3.3.6 Image recognition and memory

The PAS device, equipped with CPL-resolved perception, learning, and memory capabilities, opens up possibilities for image recognition and spiking neural networks (SNNs) in artificial neuromorphic vision systems. The vision signals, represented by the outline of the telson keel in a 7 x 7 pixel format, are encoded as CPL spikes with varying spatiotemporal information to program the developed array. The EPSC values measured in each PAS device in the array correspond to the color intensity of each pixel. Image recognition involves the variation of color levels for each pixel across different numbers of LCP, and RCP pulses in the mapping process (**Figure 3.11a**). The synaptic weights, represented by the EPSC values in the PAS array, exhibit enhanced sharpness after applying a sequence of stimuli (3, 5, and 7 spikes), resulting in progressively clearer memorization. Notably, the LCP-induced memorized graphics demonstrate higher EPSC values and a recognizable likeness to the input pattern, indicating that this mode is the most effective visual perception method among the three image recognition processes. Overall, these perception results highlight the great potential of our PAS device in constructing polarization-dependent neuromorphic vision systems.

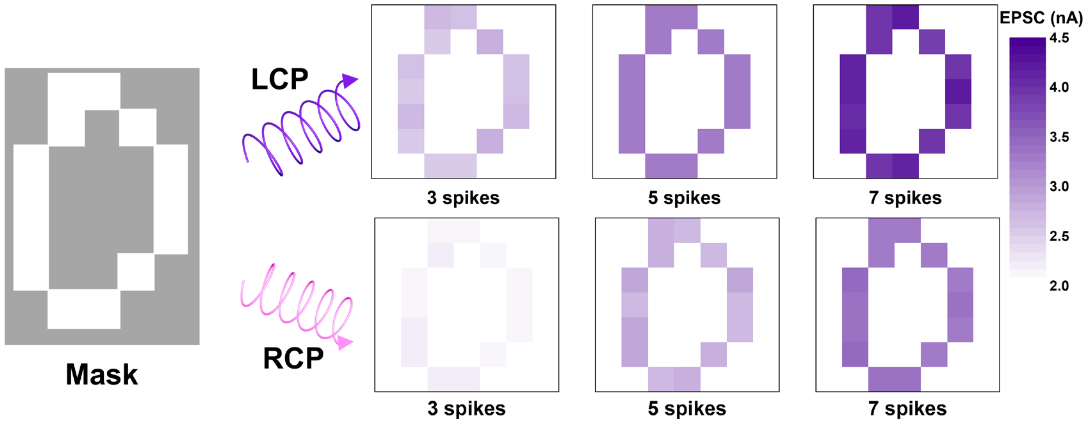

Figure 3.11 Measured weights of the object image in the initial state after a sequence of 395 nm LCP spikes and RCP spikes (10 μW cm^{-2}, 1 Hz).

Finally, to further assess the potential of the PAS device in large-scale image recognition tasks, we simulate SNNs using PAS modeling. As depicted in **Figure 3.12a**, the SNN architecture comprises 784 input neurons, 200 hidden neurons, and 10 output neurons. Before the training, the MNIST dataset was converted into a time-varying sequence of spikes by transforming the image pixel as a discrete value $X_{i,j} \in \{0, 1\}$. In the training, the weighted sum contributed to the neuron membrane potential $U(t)$. When the neuron was sufficiently excited by the weighted sum, the membrane potential reached a threshold θ, and then the neuron emitted a spike to its subsequent connections. The training utilized 60000 training and 10000 test images with a batch size of 200 at each epoch. After 300 epochs, the recognition accuracy was calculated for evaluation..

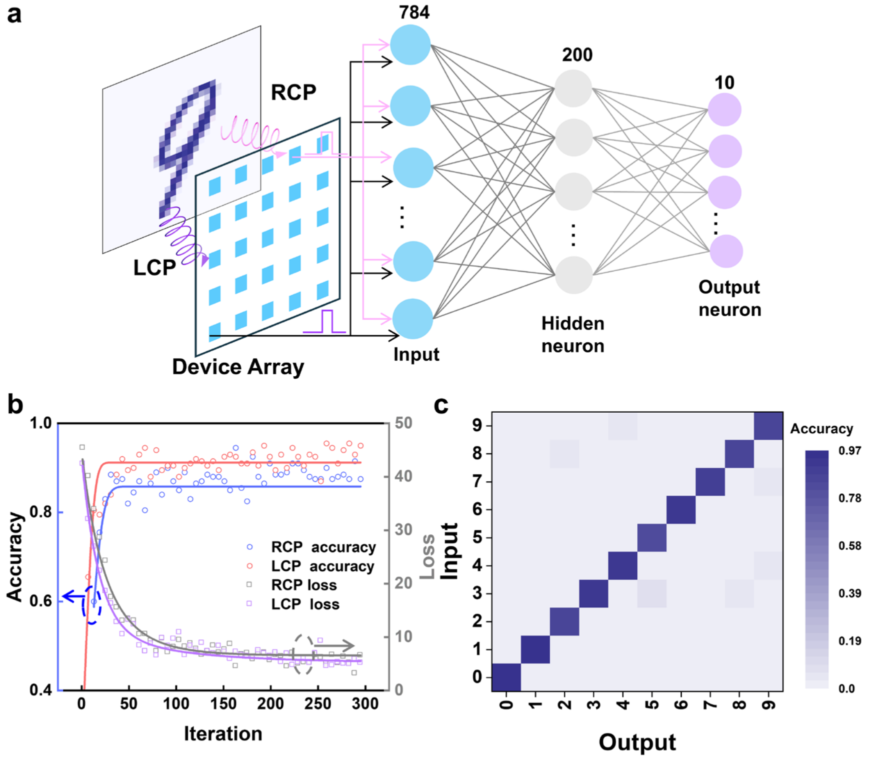

Figure 3.12 CPL image recognition. (a) Sketch structure of PAS device-based neural network. (b) Recognition accuracy and loss variation of the SNNs during 300 training epochs. (c) Recognition accuracy for every target after the training of SNNs.

For the evaluation, we select the Modified National Institute of Standards and Technology (MNIST) database as the training and test target. The SNN model's recognition accuracy is assessed using 60000 training and 10000 test images, with a batch size of 200 at each epoch. Before training, each dataset is encoded as a spike train that conforms to the Poisson equation, and then input to the neurons. The fire rate of neurons relies on the intensity of the corresponding pixel in the dataset image. For an MNIST image, if the spiking probability of a white pixel is 100%, and a black pixel never generates a spike. In the training process, the membrane potential of each output neuron accumulates by the input spikes and weight from other connecting synapses. When the membrane potential value of one output neuron exceeds the threshold, the neuron fires and releases a spike to its next connections, and its membrane potential are reset. The fired neuron will also prevent other neurons from firing by lateral inhabitation. Within a period, the neuron keeps refractory state and cannot be fired. Moreover, the corresponding synapses that contribute to the firing result will be strengthened while synapses without contribution for the fire will be weakened. After the training, every category dataset is labeled with fixed threshold and training weights. In the test process, the images are input to the trained network, the output neurons are labeled to the pattern categories in terms of their most firing times to the corresponding input dataset. **Figure 3.12b** illustrates the test results, showcasing an increasing recognition accuracy and decreasing loss value over iteration times. After 300 epochs, the SNNs modulated with LCP and RCP achieve recognition accuracies of approximately 0.93 and 0.88, respectively, demonstrating polarization-dependent learning efficiency. Furthermore, the recognition results for the LCP-based test are summarized in **Figure 3.12c**. Each test set achieves high accuracy, indicating that the PAS-based SNNs possess exceptional cognitive and classification capabilities for test data after training. To the best of our knowledge, these PAS devices demonstrate the first efficient UV-CPL-dependent synaptic behaviors and optical imaging, contributing to the development of artificial neuromorphic vision systems.

3.4 Summary

In summary, we demonstrate a CPL-sensitive heterostructure and utilize it as a chiroptoelectronic converter for polarization-dependent neuromorphic electronics. The heterostructure is composed of H-PVK with circular dichroic response ability and SNWTs with good conductivity, and exhibits a high photoresponsivity above 0.24 A/W at 395 nm.

With the superior chiroptic performance, this heterostructure can be utilized as a special PAS for the simulation of the mantis shrimp neural vision system. A series of synapse activities such as EPSC, PPF, SFDP, STP, and LTP, are successfully implemented on the PAS device under the CPL spikes encoded with different spatiotemporal information. According to the excellent temporal information encoding/decoding features, the PAS device array is developed and capable of circular polarization-dependent perception as well as memory, which exhibits great potential in enhancing image contrast. Further, the PAS is utilized to assemble the SNNs and achieves a high recognition accuracy up to 93% in pattern recognition. The H-PVK/SWNTs heterostructure as circular polarization-sensitive prototypes shows great prospects in constructing intelligent neuromorphic vision systems.

Chapter 4 Chiral Halide Perovskite Nanowire for CPL-resolved Visible Photonic Artificial Synapse

4.1 Introduction

Polarization of light describes the vibrational direction of electromagnetic waves along light propagation direction during transmission.[88-90] Polarized light arises from common scenes such as surface reflection or refraction, biological polarizers and scattered skylight in the natural environment.[91-92] Compared to color properties (intensity and wavelength), polarization offers distinct advantages by providing multi-dimensional information, including polarization degree, polarization ellipticity, and rotation direction, which enrich the characterization of light and contribute to a more comprehensive understanding of the optical environment such as surface topography, structural composition and three-dimensional geometry.[93] The human vision system primarily relies on color-based processing and is insensitive to polarized light. Yet certain animals (i.e., bees, ants and mantis shrimps) have evolved specialized visual systems that allow them to effectively detect polarization and utilize it as a crucial source of survival information.[94-95] PAS devices with high biological plausibility could faithfully imitate the visual activities of animals, which facilitates the construction of in-sensor computing systems.[96-97] Currently, there is extensive research on color-dependent PAS devices.[72, 98-99] But there is a scarcity of reported PAS devices capable of sensing both linearly polarized light (LPL) and CPL. Full-Stokes parameters sensitive PAS devices show great significance for advanced visual tasks (i.e., multimode perception, encrypted communication and fast feature extraction) and photonic computing such as physical reservoir computing (RC). To achieve the full-Stokes polarization-resolved PAS device, the light absorber in such devices should have linear dichroism, handedness-sensitive optical absorption, efficient charge transport, and synaptic behaviors simultaneously, which has not yet been reported.

Traditionally, the detection of polarized light relies on additional optical elements such as linear polarizer, half-wave plate (λ/2), and quarter-wave plate (λ/4), which introduces high complexity and cost of system.[100-101] To address those challenges, several strategies have been proposed for distinguishing LPL and CPL. For example, 1D NWs or 2D transition metal dichalcogenide materials with asymmetric crystal structures are employed in detecting LPL owing to their intrinsic linear dichroism (LD).[102-105] For CPL sensing, chiral perovskites have garnered significant attention due to their high CD and anisotropy, which arises from the inherited chirality from chiral ligands and excellent absorbance ability of inorganic components (BX_6^{4-}, B = Pb, Sn; X = I, Br, Cl).[11, 106-107] Despite the widespread development of LPL or CPL-sensitive optoelectronics, the research on full-Stokes polarization-resolved PAS devices with high biological plausibility is limited, which depresses the development of polarization-dependent neuromorphic devices and RC systems. Chiral perovskite (PVK) NW inherits the LD property of 1D nanostructure and CD property of chiral material, exhibiting significant promise in sensing Stokes parameters. Compared with film-type chiroptoelectronics, chiral PVK NW exhibits energy-efficient characteristics in terms of power consumption due to the reduced size and improved absorption induced by the increased surface-to-volume ratio, which are advantageous in constructing neuromorphic devices and nanoscale RC systems. However, chiral PVK typically exhibits low conductivity and fast carrier recombination.[86, 108] It is necessary to combine the nanostructured chiral PVK with an appropriate carrier extraction layer for exploring the full-Stokes polarization-dependent PAS devices.

In this work, we achieve for the first time the PAS device based on a single chiral PVK NW for full-Stokes polarization sensing, memory and computing. The synthesized chiral PVK NW demonstrates intrinsic LD and high CD (> 400 mdeg), which enable the PAS device to effectively distinguish LPL and CPL. The efficient hole transfer from chiral PVK NW to the hole-transporting layer MXene, as verified by ultrafast TA, contributes to a high responsivity (2.3 AW^{-1}) and a series of synaptic behaviors, including STP and LTP with power consumption per synaptic as low as 0.5 pJ. Importantly, the PAS-based RC system is developed with a low normalized root mean square error (NRMSE) of about 0.023 in the Mackey-Glass time series forecasting task. Our NW-PAS with high biological plausibility facilitates the development of full polarization-resolved nanoscale neuromorphic optoelectronics, exhibiting great potentiality for remote sensing, neuromorphic computing, and advanced energy-saving vision systems

4.2 Experimental section

Materials: R-(+)-α-Methylbenzylamine (⩾ 99.0%), S-(-)-α-Methylbenzylamine (⩾ 99.0%), N, N-dimethylformamide (DMF, 99.5%), dimethyl sulfoxide (DMSO, ⩾99.9%) and lead iodide (PbI_2, 99.999%) were purchased from Sigma-Aldrich. Multi-layer MXene powder and few-layer $Ti_3C_2T_x$ MXene (5mg ml^{-1}) solution were purchased from Jilin 11 Technology Co., Ltd.

Synthesis of (R-/S-MBA)$_2$PbI$_4$ nanowire: The chiral PVK NWs were synthesized via an antisolvent-assisted solution method. First, the R-(+)-α-Methylbenzylamine/S-(-)-α-Methylbenzylamine hydroiodide, (*R*-MBA)PbI/(*S*-MBA)PbI, was synthesized according to previously reported method[9]. Then, (*R*-MBA)PbI/(*S*-MBA)PbI and PbI$_2$ (molar ratio 2:1) were dissolved in a mixture of DMF and DMSO (volume ratio 7:3) to obtain the (*R*-MBA)$_2$PbI$_4$/(*S*-MBA)$_2$PbI$_4$ precursor with a concentration of 0.02 M. Subsequently, 5 µl precursor was dropped on the substrate placed in a glass bottle with 1 ml isopropyl alcohol (IPA) in glove box, and the glass bottle was sealed immediately, followed by heating up to 60 °C. After tens of minutes, the chiral perovskite nanowires were synthesized on the substrate.

Optical spectroscopy: For absorption and CD spectra, a fiber-coupled light source (EQ-77-fc, Energetiq) was utilized to generate broadband white light. For CD measurement, the white light is collimated and passes through a linear polarizer (WP25M-UB) and a quarter-wave plate (AQWP10M-580) for generating CPL. LCP and RCP can be generated by rotating the quarter-wave plate through 90°. The CPL beam is focused on the as-prepared sample and collected by an optical spectrometer (Spectra Pro 2300i, Acton) equipped with a CCD camera (Pixis 256BR, Princeton Instruments). For absorption measurement, the white light is directly focused onto the sample and then captured by the spectrometer. The absorbance (A) was defined as $A=\log_{10}\frac{I_0}{I}$, where I_0 and I are the transmitted light intensity through quartz and chiral PVK NW, respectively. TA spectroscopy was obtained using an amplified titanium: sapphire femtosecond laser (central wavelength 800 nm, pulse width 50 fs, repetition rate 1 kHz, Coherent Libra) equipped with an optical parametric amplifier (pump wavelength tunable from UV to IR, OPerA Solo) and a Helios pump-probe setup (probe wavelength tunable from UV to NIR, Ultrafast Systems). Raman spectra was measured by the WITEC alpha300 R Raman imaging microscope system.

Device fabrication: The wafer with a 300 nm oxide layer was selected as the substrate and was cleaned ultrasonically with acetone, IPA, and distilled water in turn. Then, the substrate was treated with UV-ozone for more than 15 minutes. The MXene was diluted to 0.5 mg/ml, followed by a centrifugation (4500 rpm for 15 min). After that, the MXene layer was fabricated by soaking the substrate in diluted MXene solution, followed by an annealing process (80 °C) for 30 minutes in nitrogen condition. After that, the chiral perovskite nanowires were prepared on the MXene by antisolvent-assisted solution method. The electrodes (5 nm Cr/45 nm Au) were deposited by electron beam lithography, thermal evaporation, and a lift-off process in turn.

Device measurement: The electrical test of PAS devices was completed using a semiconductor analyzer (Keithley 4200-SCS), which is connected to the Lake Shore probe station, and the reading bias is 0.5 V. The LPL was generated by using a linear polarizer and half-wave plate while the CPL was defined using a linear polarizer and quarter waveplate. The intensity of LPL/CPL was calibrated by a standard optical power meter (Newport 843-R with a PD300-UV optical power detector) before measurement. All the tests were implemented in an air atmosphere at room temperature.

Sample characterization: The surface morphology was observed by field-emission scanning electron microscope (Tescan MAIA3) and Scanning Probe Microscope (Asylum MFP-3D Infinity). X-ray diffraction (XRD) was performed by Bruker D8 Advance instrument (Cu Kα radiation, λ=1.5418 Å operating at 40 kV and 40 mA). The ultraviolet photoelectron spectroscopy (UPS) analysis was performed by the Thermo Scientific Nexsa instrument. The diameter of the chiral perovskite nanowire was measured by Bruker DektakXT Surface Profiler.

4.3 Result and discussion

4.3.1 Device fabrication

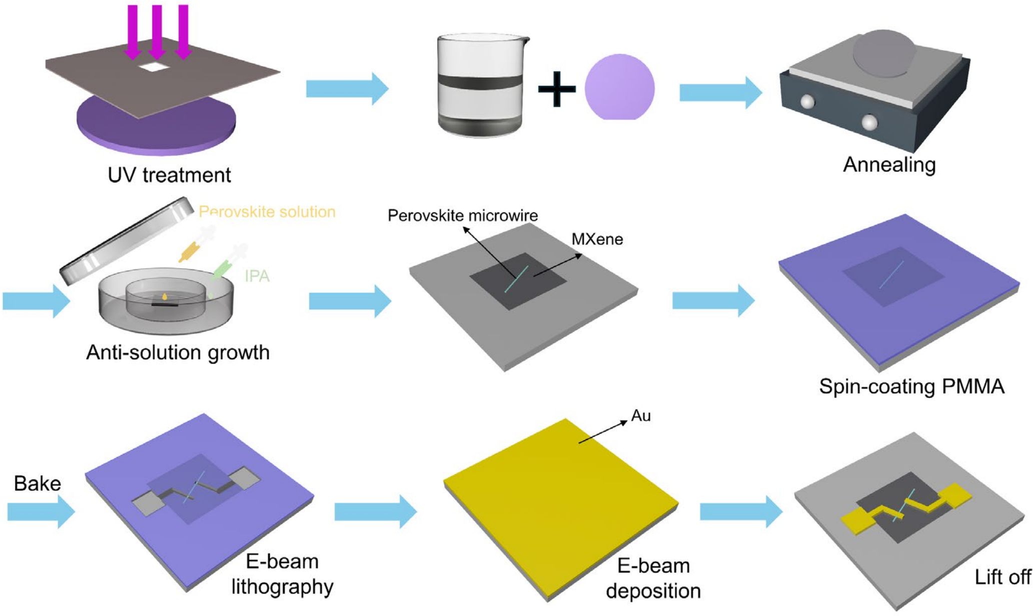

Figure 4.1 Sketch diagram for the fabrication of the PAS device.

As pictured in **Figure 4.1**, the substrate was treated by the UV-ozone plasma for more than 15 minutes, and then the substrate was immersed in the few-layer MXene solution overnight to deposit the hole extraction layer followed by an annealing process in the nitrogen atmosphere. To synthesize the chiral perovskite nanowire, the as-prepared chiral perovskite solution (5 μl, 0.02 M) was dropped on the substrate placed in a glass bottle with 1 ml isopropyl alcohol (IPA) in a glove box, and the glass bottle was sealed immediately, followed by heating up to 60 °C. After twenty minutes, the chiral perovskite nanowires were obtained. Finally, the electrode (45 nm Au/ 5 nm Cr) was defined by typical E-beam lithography, thermal evaporation (nitrogen atmosphere), and lift-off process.

4.3.2 Characterization of chiral halide perovskite nanowire and MXene

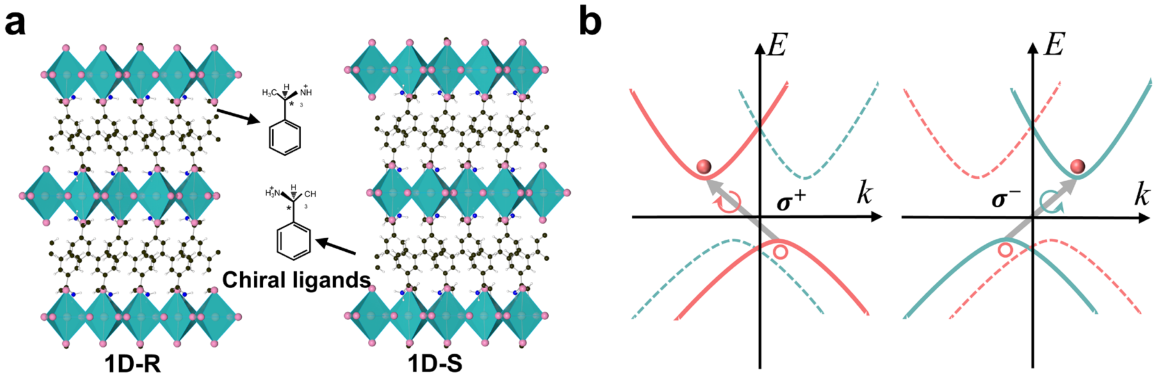

Figure 4.2 Chiral perovskite structure and bang energy. (a) Crystal structure of chiral perovskites modulated by *R*-α-MBA (left) and *S*-α-MBA (right). (b) Energy band perturbation by chirality for asymmetric CD spectra (σ^+ is RCP, and σ^- is LCP).

Introducing the chiral organic molecules at the A site of Ruddlesden-Popper PVK (A_2BX_4, where A is a bulky ammonium cation and $(BX_6)^{4-}$ is inorganic frameworks) induces the formation of chiral crystal structures. For example, enantiomers R- and S-α-Methylbenzylamine (*R*-MBA and *S*-MBA) with different handedness could serve as the organic part for synthesizing chiral 1D-R and 1D-S (**Figure 4.2a**), which shows CD with opposite signs near the first excitonic band edge. To understand the CD of chiral perovskite, the energy band of 1D-S and 1D-R that is perturbed by chirality is sketched (**Figure 4.2b**) and the related mechanism is illuminated.[109-110] The states of electrons in the VB and CB can be described by the angular momentum quantum number ($J = 1/2$) and magnetic quantum number ($m_j = \pm 1/2$). The spin angular momentum (SAM) in CPL beams interacts with chiral materials and different SAM in LCP/RCP could excite the electrons with an angular momentum from |+1/2> (|-1/2>) to |-1/2> (+1/2>) state, respectively.[111-112] This excitation selection rule illustrates the absorption difference between chiral perovskites with different handedness and the shape of CD spectra.

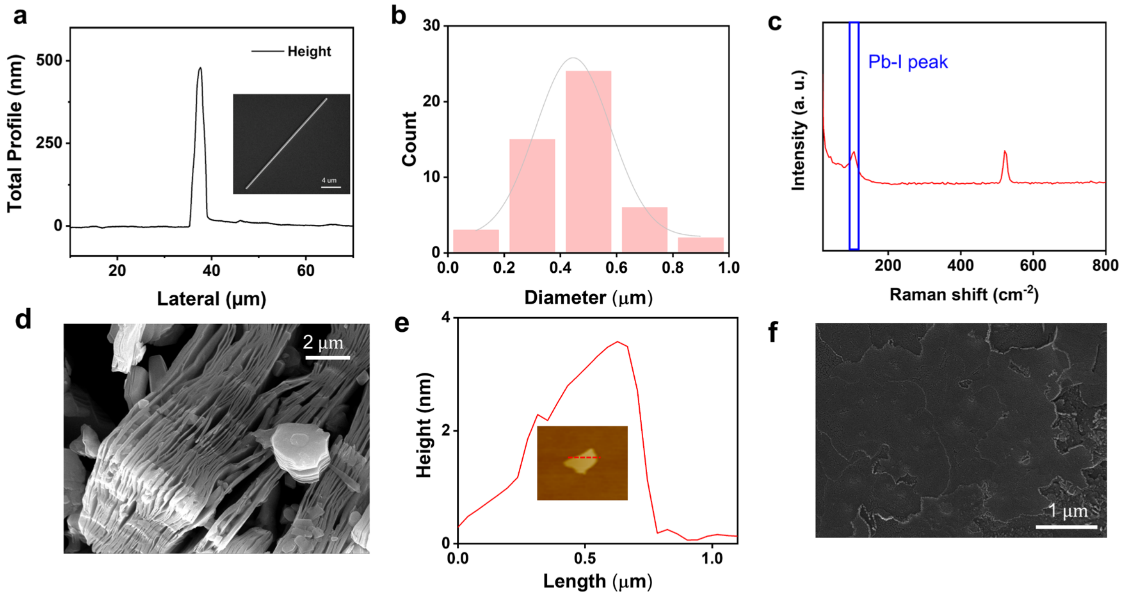

Figure 4. 3 Height measurement, diameter count, Raman and PL spectra of chiral PVK NW. (a) Diameter of single chiral PVK NW measured by step profiler. Inset shows the image of the measured chiral perovskite nanowire. (b) Diameter distribution (Sample number = 50) of antisolvent-assisted method synthesized chiral perovskite nanowires. (c) Raman spectra of chiral perovskite nanowire and the peak around 100 indicate the Pb-I bonding. (d) SEM image of multilayer MXene. (e) AFM characterization of few-layer MXene. (f) Few-layer MXene film.

The morphology, crystal structure, diameter and other properties of synthesized nanowires are characterized by SEM, surface profiler, Raman and PL spectra, respectively. The nanowire exhibits a height of approximately 500 nm as shown in **Figure 4.3a**, and the inset image shows the SEM image of a single nanowire with a length of tens of micrometers. A statistic (**Figure 4.3b**) demonstrates the diameter of the prepared nanowires is concentrated around 400-500 nm, and this uniform size underlies the foundation for constructing high-performance optoelectronics. To confirm the component of the nanowire, Raman and PL spectra are measured. The peak at 100 in Raman (**Figure 4.3c**) is identical to the characteristic of bonding between lead and iodine. To obtain the few-layer MXene, multi-layer MXene (**Figure 4.3d**) was diluted to 0.5 mg ml^{-1} followed by a centrifugation (4500 rpm for 15 min). After that, the few-layer MXene (**Figure 4.3e-f**) was fabricated by soaking the substrate in diluted MXene solution, followed by an annealing process (80 °C) for 30 minutes in nitrogen condition.

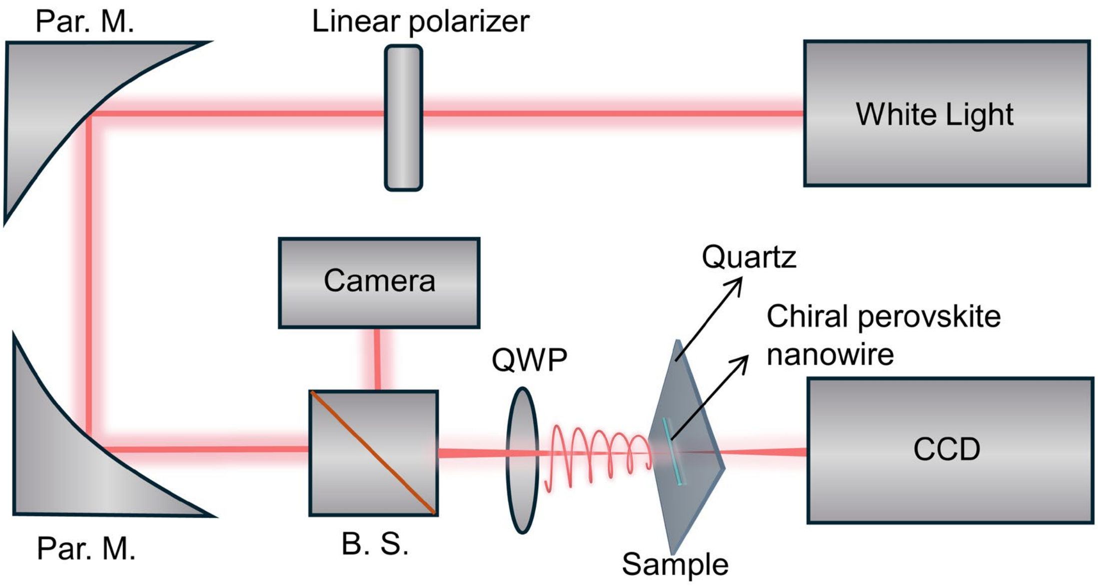

Figure 4.4 Optical setup for micro-CD measurement.

To measure the absorption and CD spectra of a single NW, a microscopic transmission measurement (**Figure 4.4**) is applied.[113] The broadband white light through the linear polarizer is reflected by two paraboloidal mirror (Par. M.) elements, and then passes through the beam splitter (B. S.) and a quarter-wave plate followed by focusing on the sample. Ultimately, the transmitted signal is collected by the spectrometer.

In the time-resolved TA experiments (**Figure 4.5**), two femtosecond laser beams are utilized. One is a monochromatic and energetic pump beam, which triggers the specific photoreaction for investigation. The second one is a weak and broad probe beam. The pump beam (400 nm) passes through a linear polarizer and a quarter waveplate, generating a CPL pump beam. Subsequently, the pump beam interacts with a certain volume of the sample, inducing the transition of a specific number of molecules to their excited states. After a defined time, delay following the pump pulse, the probe pulse passes through the same sample volume and measures the resultant variations in absorption. Ultimately, the probe beam is collected by the charge-coupled device (CCD).

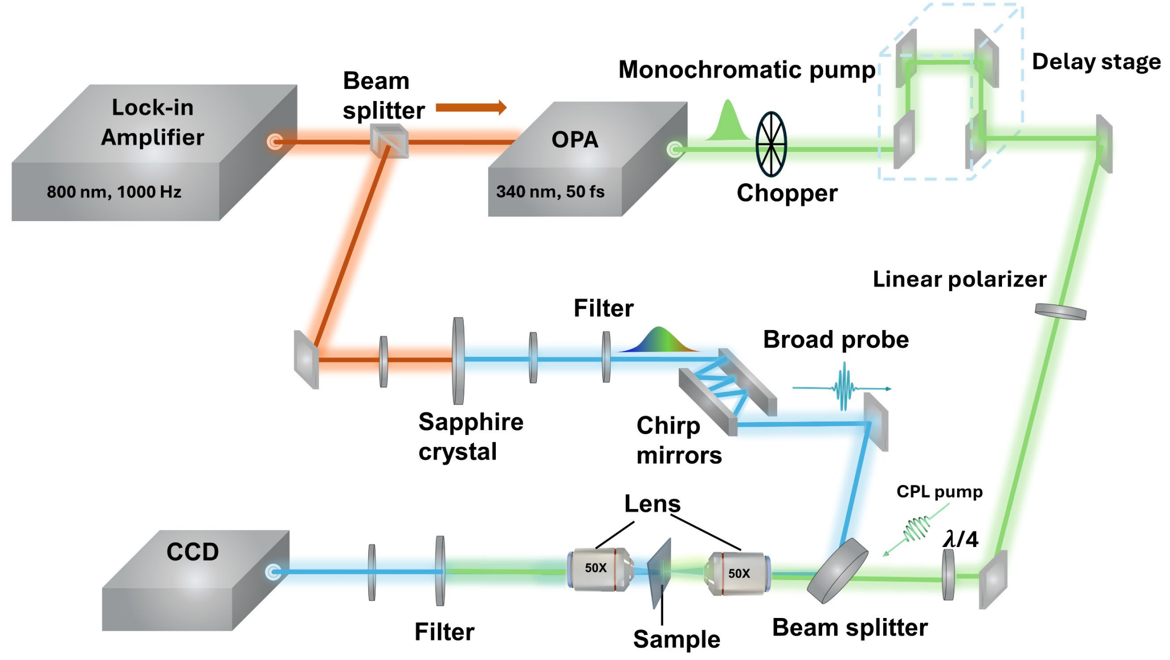

Figure 4.5 Sketch of the ultrafast micro-TA measurement system.

The sample exhibits an absorbance peak around 500 nm in the visible region (**Figure 4.6a**). In the CD measurement, the CPL with different handedness is generated by rotating the quarter-wave plate with respect to the fast-axis and incident linear polarization direction. The CD value is calculated according to the equation (4.1),

$$\mathrm{CD} = 32980 \times \log_{10}(I_R/I_L) \tag{4.1}$$

where I_R and I_L are the transmitted intensities of RCP and LCP, respectively.[114] The 1D-R and 1D-S exhibit symmetrical CD signals at the same position but slightly different in intensity (**Figure 4.6b**). In particular, the 1D-R NW shows a high CD value over 400 mdeg, which is 1-2 orders of magnitude higher than the reported chiral PVK film.[65, 115] The large CD ensures that our single-NW photodetector can clearly distinguish the handedness of CPL. COMSOL simulation is performed to verify the LD of the synthesized chiral PVK NW. In this analysis, the periodic boundary conditions are implemented on the x-axis, and the perfectly matched layer boundary conditions are applied in the other axes (y and z). Light absorption is described by the square of electric field amplitude within the chiral PVK NW, and the polarization angle (θ) is defined by the angle between the light polarization axis and NW direction (**Figure 4.6c**). The plane wave source with different polarization states illuminates on the chiral PVK NW along the z-axis. As shown in **Figure 4.6d**, the simulated mapping has a high absorption of around 500 nm and the absorption strength of the LPL gradually decreases with θ changing from 0 to 90 degrees. These CPL and LPL optical results demonstrate the full-polarization detection capability of our chiral PVK NW, opening exciting possibilities for the development of full-Stokes polarization PAS optoelectronics. Moreover, the large CD ensures that our single-NW photodetector can clearly distinguish the handedness of CPL (**Figure 4.6e and f**).

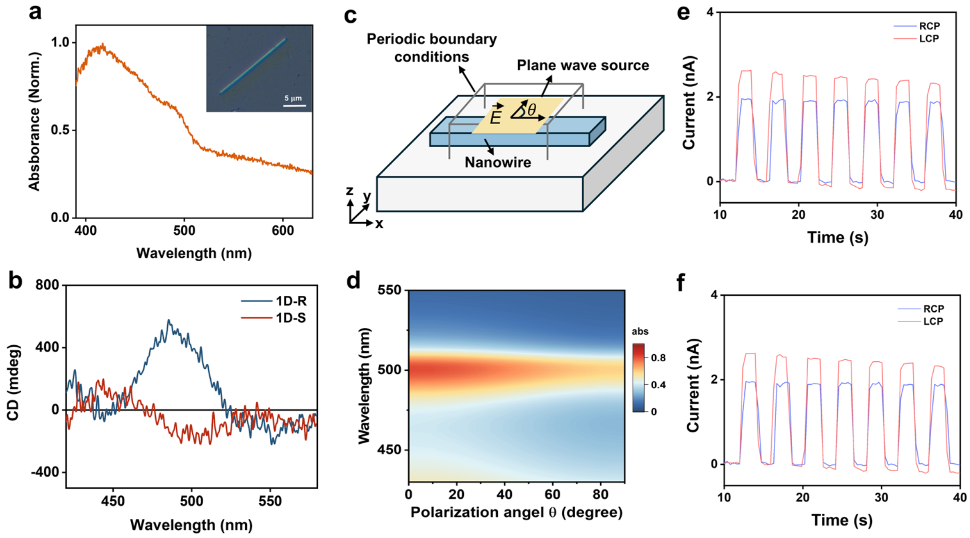

Figure 4.6 Chiroptical properties. (a) Absorbance of single chiral PVK NW. (b) Micro-CD spectra of 1D-S and 1D-R NWs. (c) Simulation model of PVK NW constructed by COMSOL. (d) Absorbance of NW under LPL with different polarization angles. (e) Current-time (I-t) response of R-type NW. (f) I-t response of S-type NW. The wavelength of the CPL is 505 nm, and the intensity of the CPL is 50 μW cm^{-2}.

4.3.3 Mechanism of polarization-dependent carrier dynamics

The single-NW system alone does not exhibit synaptic behavior. To achieve the desired polarization-resolved PAS device, considering the low electric conductivity and strong excitonic property of chiral perovskite, few-layer 2D $Ti_3C_2T_x$ MXene is deposited on the substrate to not only enhance the photoexcited charge transport property, but also to ensure the PAS functionality of our PVK NW device (**Figure 4.7a**). 2D MXene with outstanding electronic conductivity, excellent optical transparency, and high mobility has been recently utilized as a hole extraction layer in optoelectronic devices (e.g., perovskite solar cells, PDs).[116-118] The height of monolayer $Ti_3C_2T_x$ MXene is approximately 4 nm, and the deposited MXene layer is less than 30 nm thick. The synthesized chiral PVK NW is further developed on the MXene via an antisolvent-assisted method, followed by a typical electrode fabrication process for device fabrication for PAS application.

To utilize the PVK NW in the PAS device, the photoexcited charge carriers should be separated for charge transport and storage. The band energy analysis (**Figure 4.7b**) indicates that holes in PVK NW can be transferred to the VB of MXene for transportation while the electrons are left in the CB of the PVK for charge storage. The photoexcited carrier dynamics in chiral PVK NW with and without MXene are further verified using the ultrafast micro-TA system. The few-layer MXene exhibits a broad excited absorption (ESA, i.e., positive ΔA) band in the visible range (**Figure 4.7c, left**), which is similar to the previous reports[119-120] and due to the further excitation of pump-generated electrons to the higher energy levels by the probe beam. A short-lived PB (i.e., negative ΔA) band is observed at around 500 nm resulting from the state filling of band-edge excitonic states in chiral PVK NW (**Figure 4.7c, middle**). In contrast, it is obvious that the chiral PVK NW on MXene shows a broad and long-lived PB spectrum with additional long tail states below the band edge (**Figure 4.7c, right**). The signal below the band edge could be ascribed to the introduced trap states of the photoexcited electrons. The heterostructure also shows higher PB signals under the same pump condition compared to PVK NW alone (**Figure 4.7d**), which would be due to the electron transfer from MXene. The neat PVK NW exhibits an average exciton lifetime of about 36 ps, while the heterostructure shows a relatively longer carrier lifetime of 68 ps (**Figure 4.7e**). The slower decay of the heterostructure suggests the dissociated exciton in PVK prevents the fast electron-hole recombination. The emergence of the long-lived states in PVK NW on MXene are thus favorable for photoexcited carrier storage. Those carrier dynamics demonstrate the charge storage capability of the heterostructure, which contributes to the construction of a polarimeter with synaptic behavior.

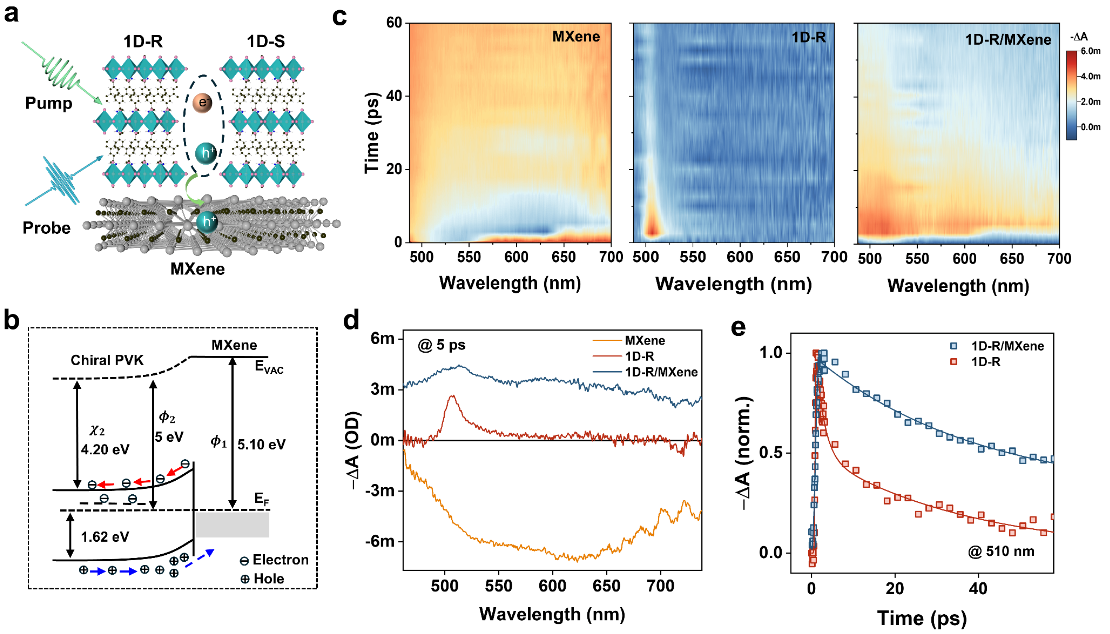

Figure 4.7 Carrier dynamics in single chiral PVK NW/MXene heterostructure. (a) Pump-probe process and carrier dynamics of the heterostructure. (b) Energy band diagram at chiral PVK NW and MXene interface (E_{vac} is the vacuum energy level, E_F is the Fermi energy level). (c) 2D mapping TA spectra of MXene, 1D-R, and 1D-R/MXene measured under 400 nm laser excitation. (d) TA spectra (at 5 ps) of Mxene, PVK NW and heterostructure measured under 400 nm LCP pump with intensity of 165 μJ cm^{-2}. (e) Normalized band-edge GSB dynamics of 1D-R and 1D-R/MXene under 400 nm LCP excitation.

4.3.4 Full-Stokes polarization-resolved photodetection

To verify the polarization-resolved optoelectronic performance, the photoresponse of the

PAS device based on a single PVK NW on MXene is measured under polarized light with different handedness, wavelengths, and intensities. The photocurrent of heterostructure is much larger than that of PVK NW alone, indicating the enhanced charge transportation. The photocurrent difference under CPL illumination demonstrates that the constructed PAS device can effectively discriminate between LCP and RCP light (**Figure 4.8a**). The PAS device achieves a high responsivity of 2.3 AW^{-1} at a low power density (**Figure 4.8b**), indicating an excellent detection capability under weak polarized light conditions compared with other reported PDs and PAS devices. The responsivities of the PAS to CPL at different wavelengths (460 nm, 480 nm, 505 nm, and 532 nm) demonstrate a peak at around 505 nm with a larger current under LCP (RCP) for 1D-S (1D-R) devices, consistent with the chiroptical properties of the chiral PVK NWs (**Figure 4.8c**).

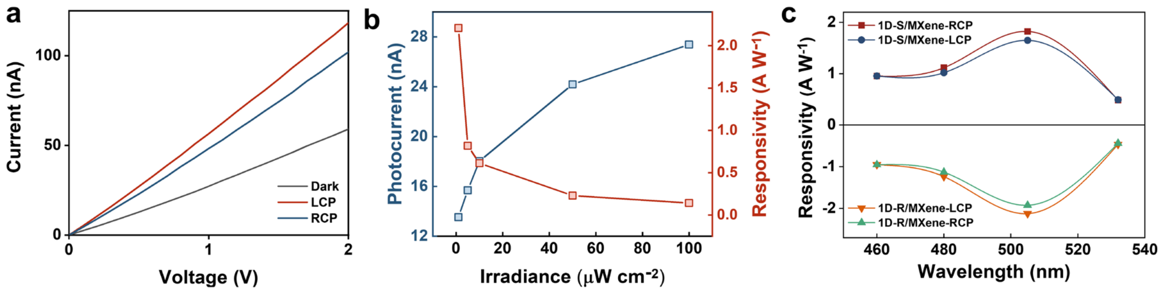

Figure 4.8 CPL response ability. (a) Current-voltage characteristic of the 1D-R NW-based PAS device under the LCP/RCP illumination (505 nm, 50 μW cm^{-2}) and dark conditions. (b) Photocurrent and responsivity of the PAS device under 505 nm LCP with different intensities. (c) Responsivity of PAS device under LCP and RCP at different wavelengths (50 μW cm^{-2}).

Polarized light can be accurately described by Stokes parameters including the total intensity S_0, the horizontal/vertical linear polarization component S_1/S_2, and the circular component S_3.[121] A Poincaré sphere (**Figure 4.9a**) is sketched to intuitively show the states of polarization (SoP), and the orientation of arbitrary types of elliptically and linearly polarized light is visualized. Conventional detection of Stokes vectors S_0-S_2 can be realized by measuring the light intensity after the polarized light passes through the polarizer at different angles (0°, 45°, and 90°) while the judgment of S_3 should measure the light intensity after adding a quarter-waveplate in front of the polarizer at an angle of 45°. This method relies on optical components, which extremely increase the volume and complexity of detection systems. The proposed single chiral PVK NW-based PAS device with scale-down size perfectly overcomes these problems by measuring photo-induced current rather than light intensity. A series of SoP on the Poincaré sphere are illuminated to the rotated NW PAS device to determine its Stokes parameters. In this rotation measurement, the NW direction that is parallel to the polarized light (0°) is defined as zero degree, and the included angle can be controlled by rotating the stage. The photocurrents (I_0, I_{45}, I_{135}, and I_{180}) correspond to the NW at different rotation angles (0°, 45°, 90°, 135°, and 180°). **Figures 4.9b** and **4.9c** plot the photocurrent of the PAS device under different linear and helical beams, respectively. The response is fitted by a sine function, suggesting typical polarization-dependent detection ability.[122] For an ideal linear polarization detector, the dichroic ratio (I_{Max}:I_{Min}, I_{Max} and I_{Min} are the maximum and minimum photocurrent of the PAS device under the LPL) is close to an infinite value. Since the response of the PAS device hardly meets this requirement, a subtraction of subtracting I_{Min} from all the measured photocurrent is performed as calibration and then to calculate S_0-S_2. Owing to the CPL response preference of the PAS device, the parameter S_3 can be obtained from the circular polarization-induced difference (ΔI_V), which has different signs and amplitudes. In detail, the calculation process of Stokes parameters can be obtained from the previous report.[123] As shown in **Figure 4.9d**, the Stokes parameters ($S_{0\text{-}3}$) are in close agreement with the input values. The average errors ($\frac{\sum_{i=1}^{n}|x_{input}\text{-}x_{output}|}{n}$) for the Stokes parameters $S_{1\text{-}3}$ are calculated to be ΔS_1 = 3.4%, ΔS_2 = 5.9%, and ΔS_3 = 9.0% (**Figure 4.9e**), which demonstrates a high-performance full-Stokes polarimeter.

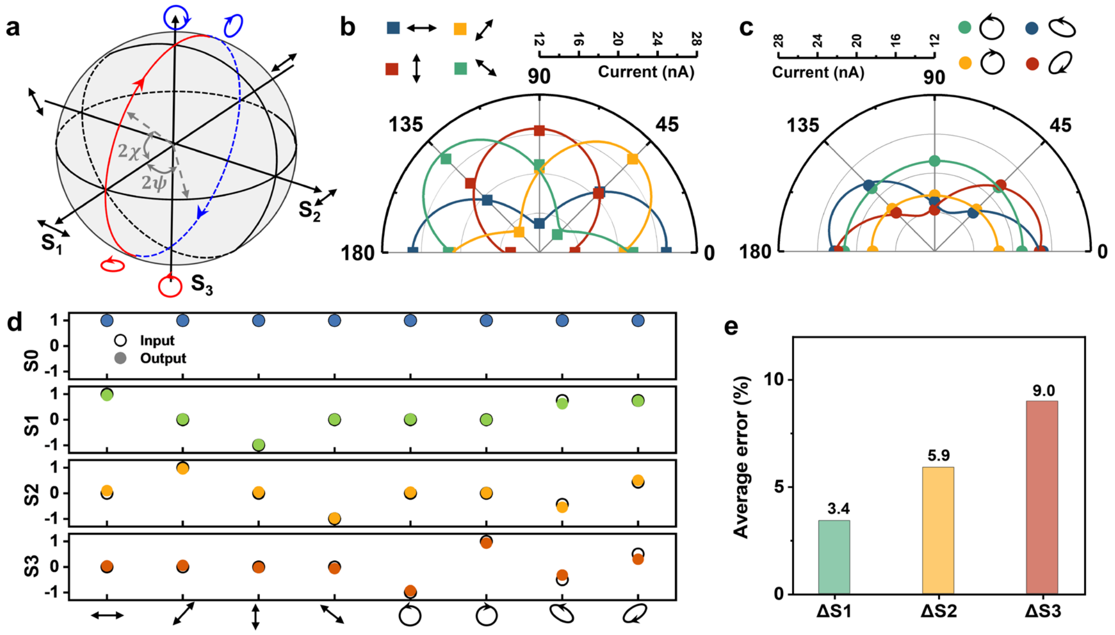

Figure 4.9 Full-Stokes polarization-resolved photodetection. (a) Poincaré sphere and related polarization states. (b) Linear-polarization and (c) ellipticity-dependent photocurrent of PAS device at different device rotation angles. (d) Input (hollow circles) and output (solid circles) Stokes parameters (S_0, S_1, S_2, and S_3) measured under different polarized light. (e) Average recognition errors for S_1, S_2 and S_3.

4.3.5 Polarization-dependent synaptic imitation

The axon terminal of the pre-neuron comes into close contact with the cell membrane of the post-neuron, forming the synapse (**Figure 4.10a**). The synapse exhibits typical behaviors, including STP and LTP, when exposed to stimuli with different coding modes. In this respect, the PAS devices have effective temporal information encoding and in-sensor computing capabilities. The polarization modulation strategies for tuning the PAS device are outlined in **Figure 4.10b**. Using the polarized light as an excitation source, our single-NW full-Stokes polarization photodetectors are used as PAS devices to mimic and verify the polarization-resolved synaptic behaviors.

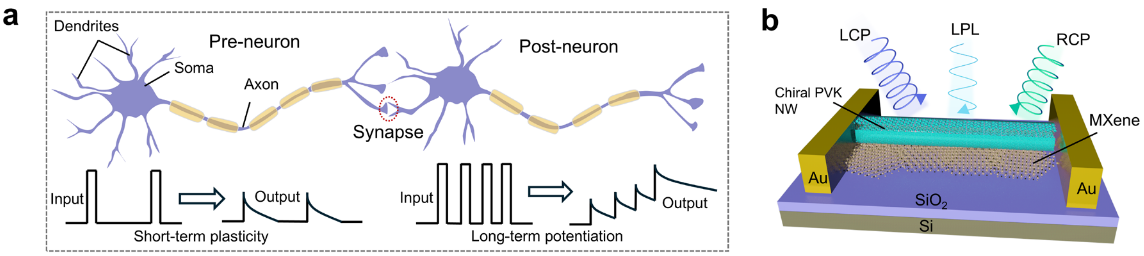

Figure 4.10 Bio-inspired synaptic device. (a) Sketch of biological synapse and typical synaptic behaviors (e.g., STP and LTP) induced by light pulses with different encoding ways. (b) Structure of bio-inspired PVK NW PAS device.

Figure 4.11a plots the EPSC triggered by a single LCP/RCP spike on 1D-R NW device. A higher EPSC peak is observed under the LCP-light stimulation, and the response gap indicates that our PAS device is able to discriminate the circular polarization states. One important feature of the synaptic behavior is low power consumption, and the energy consumption per synaptic event of the PAS device is estimated by $dE = P \times S \times dt$, where P is the power intensity of stimuli optical spike, S is the active area of device and dt is the pulse width of the optical signal. The calculated power consumption per synaptic event is approximately 0.5 pJ at the illumination of LCP/RCP spike (505 nm, 50 μW cm^{-2}, 1 Hz), which is comparable to the power consumption of the biological synapse in the human brain, demonstrating the energy-efficient nature of our NW-PAS device. Furthermore, paired-pulse facilitation (PPF), which reflects the ability to encode/decode temporal information, is mimicked by the PAS device through applying two consecutive CPL spikes with a time interval Δt (**Figure 4.11b** inset). The PPF index, calculated as A_2 (postsynaptic EPSC elicited by the second stimuli)/A_1 (EPSC excited by the first stimuli), is defined to describe the effect of Δt on the plasticity. As shown in Figure 4d, the index decays with the increasing Δt, and the LCP-induced PPF in 1D-R NW device has a longer lifetime (270 ms) than that of RCP (156 ms), suggesting a higher resolution for preprocessing temporal information with CPL resolve ability. By increasing the stimulus spikes, STP can also be converted to LTP as shown in **Figure 4.11c**. Since the EPSC response of the PAS device depends on both the current input stimuli and the historical state, it generally shows an ascending trend with increasing CPL spikes. **Figure 4.11d** shows the EPSC response under multiple CPL spikes with various wavelengths with LTP behaviors, and the 505 nm CPL stimulus signal exhibits relatively more efficient modulation due to the higher absorption of the chiral PVK NW. **Figure 4.11e** demonstrates the typical spike-frequency-dependent plasticity (SFDP) of the PAS device, which shows that with increasing the frequency of LCP spikes, EPSC increases more rapidly with a longer decay time. Furthermore, the EPSC modulation of the chiral PAS device by the CPL light intensities and handedness is also achieved under other wavelengths. Considering the linear dichroism property of the NW, linearly polarized light is also utilized to study the associated LTP behavior of the PAS device. The polarization angle-dependent characteristic is demonstrated in **Figure 4.11f**, and polarization modulated memory behaviors are plotted in the inset picture. It shows that LPL with an orientation direction parallel to NW can more effectively stimulate the PAS device and contribute to long-term memory. EPSC signals can thus be tuned by the light wavelength, intensity, frequency, and polarization states of the incident spikes, enabling a multimode PAS device with flexible learnability. These results parallel the observation that multiple stimuli delivered in a short period can enhance the memory process in organisms, suggesting that our single chiral NW-based PAS device has not only strong biological plausibility but also the full-Stokes CPL and LPL tunability. Moreover, the full-Stokes perception capabilities of our PAS devices show great potential in processing high-dimensional information compared with the monotone modulation mode (e.g., electric or light stimulus) of artificial synapse devices.

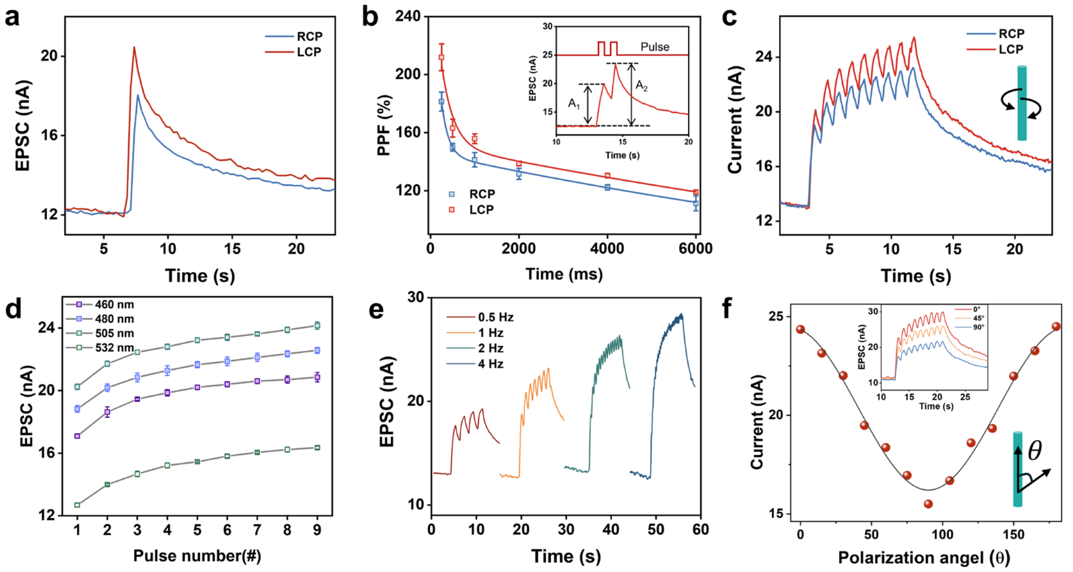

Figure 4.11 (a) Transient EPSC of 1D-R NW based PAS induced by single LCP/RCP spike (505 nm, 50 μW cm^{-2}). (b) PPF index of the PAS device with increasing excitatory stimuli interval. The inset shows the response triggered by two consecutive CPL spikes with an interval of 1s. (c) EPSC excited by multiple CPL spikes. (d) EPSCs in response to multiple CPL spikes at wavelengths of 460 nm, 480 nm, 505 nm and 532 nm, respectively. The power intensity is 50 μW cm^{-2}. (e) Frequency-dependent EPSC induced by multiple spikes in 7 s.

(f) Photoresponse of the PAS device under incident light with different linear polarization states (505 nm, 50 μW cm^{-2}). Inset shows EPSCs triggered by multiple LPL spikes with polarization angles of 0°, 45°, and 90°.

4.3.6 Polarization-dependent reservoir computing systems

Biological neural network in the human brain (**Figure 4.12a**) effectively projects the input signals to high-dimension space where the features are linearly separable, achieving the cognition of sophisticated intelligence. The PAS device possesses a unique temporal summation function, enabling its response to depend on both the current state and historical input, which proves advantageous in imitating human cognition by the construction of physical RC systems.[124] These RC systems find applications in various domains such as waveform classification, speech recognition, and time series prediction.[125-126] Here, our PAS devices are utilized as physical reservoirs in the RC neural networks with pre-processed input data by a mask. The Mackey–Glass (MG) time series is adopted to evaluate the capability of the RC system in analyzing temporal information. Mackey-Glass time series is generated according to a nonlinear time-delayed differential equation (4.1),

$$\frac{dx}{dt} = \beta \frac{x(t-\tau)}{1+(x(t-\tau))^n} - \gamma x(t) \tag{4.2}$$

Different behaviors can be induced by setting the values of the parameters. By changing the value of τ, fixed-point attractor ($\tau < 4.43$), limit cycle attractor ($4.43 < \tau < 13.3$), double limit cycle attractor ($13.3 < \tau < 16.8$), and chaotic behaviors ($\tau > 16.8$) can be obtained, respectively. Here, the parameters are set as $\tau=23$, n=10, $\beta = 0.2$, $\gamma = 0.1$. **Figure 4.12b** describes the basic rules of MG sequence prediction, and the output value could be deduced by analyzing the temporal correlation between input datasets. Two thousand data points are generated using the MG equation. The first half is designated as the training dataset, while the remaining parts are reserved for testing purposes.

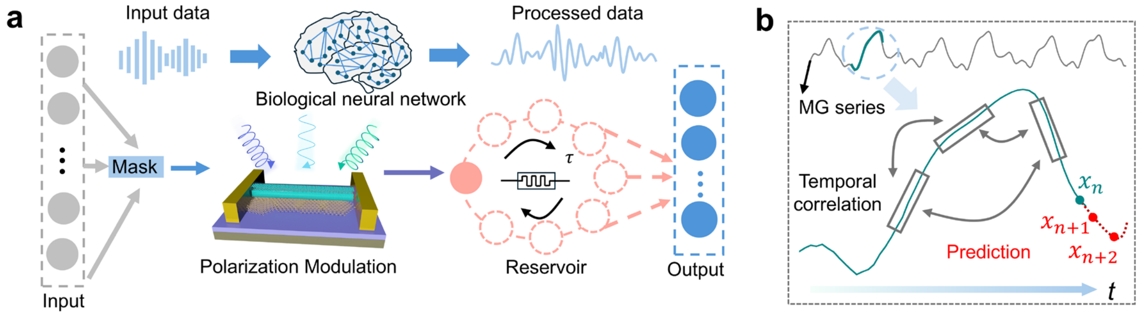

Figure 4.12 RC systems based on PAS device. (a) Sketch of the RC system in which the PAS serves as the physical reservoir. (b) Sketch diagram of MG data processing.

The reservoir states modulated by different states of linear polarization (**Figure 4.13a**) and circular polarization (**Figure 4.13b)** are compared, and these diverse temporal dynamics demonstrate the polarization-enriched reservoir states, underlying the high performance of the RC system. **Figure 4.13c** summarizes the NRMSE at various reservoir numbers *(N*) and SoP. The prediction capability is enhanced with the increasing reservoir number and exhibits a balanced performance in the training process when *N* reaches 50. The SoP shows different effects on the training results, providing a flexible modulation way for the RC systems. **Figure 4.13d** shows the training results with the lowest NRMSE, and the predicted results are almost consistent with the input, indicating an excellent predictive ability of the RC system. The test results achieve an NRMSE value of approximately 0.023. Furthermore, the test traces are replotted in phase space (**Figure 4.13e**), and the output line overlaps well with the target, which demonstrates the reliable prediction behavior of the RC system. The designed PAS device thus exhibits great biological plausibility in mimicking polarization-resolved synaptic behavior, and the constructed single-NW-PAS-based RC system introduces a new computing paradigm for processing temporal and sequential data.

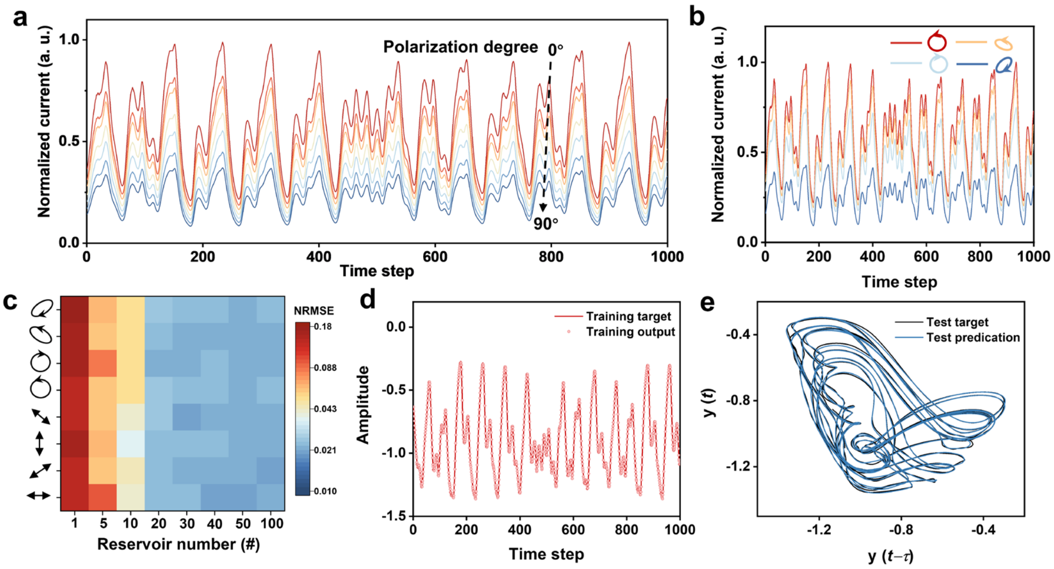

Figure 4.13 RC computing. (a) Dynamic responses of the reservoir induced by the LPL-enriched reservoir states (0°-90° at an interval of 15°). (b) Elliptical polarization-enriched reservoir states. (c) Prediction errors correspond to different numbers of reservoirs and SoP. (d) Training results obtained from the PAS-based RC system. The line indicates the target, and the dots are the experiment output. (e) RC system output results plotted in phase space.

4.4 Summary

In summary, we successfully synthesized chiral PVK NWs with a high CD and intrinsic LD, underlying the construction of the full-Stokes polarimeter based on a single NW. By combining the chiral PVK NW with MXene, the heterostructure demonstrates remarkable photoresponsivity (2.3 A W^{-1} at 505 nm) and excellent polarization-resolved capabilities. This polarization-dependent PAS device can faithfully mimic typical synaptic activities such as EPSC, PPF, SFDP, and LTP with low power consumption (approximately 0.5 pJ per synaptic stimuli) when exposed to polarized beams with diverse spatiotemporal encodings. Furthermore, the full-Stokes polarization PAS device can serve as a physical reservoir of the RC system, enabling outstanding performance (NRMSE = 0.023) in the prediction of chaotic time series. Our proposed PAS device, which serves as a prototype for identifying full-Stokes polarization, shows immense potential for the development of polarization-dependent nanoscale neuromorphic vision systems.

Chapter 5 Quantum-Well Structured Chiral Halide Perovskite for Spintronics

5.1 Introduction

The burgeoning field of spintronics, which exploits the quantum spin state of electrons alongside their charge, promises transformative advancements in electronic devices, offering benefits such as non-volatile memory, reduced power consumption, and enhanced processing speeds.[127] However, the realization of efficient spintronic technologies hinges on the development of materials capable of generating, manipulating, and sustaining spin-polarized currents. Traditional materials, such as ferromagnetic metals and diluted magnetic semiconductors, face challenges including limited compatibility with semiconductor technologies and inefficient spin injections.

Recent attention has turned to CHPs, where the incorporation of chiral organic cations introduces structural asymmetry, endowing these materials with unique spin-dependent properties. Chirality of ligands endows CHP the CISS, a phenomenon where electron transmission through a chiral structure depends on its spin state, effectively acting as a spin filter.[128-129] Moreover, the electronic features of perovskites (i.e., spin-orbit coupling) strengthen this effect and positions CHP as a compelling platform for spintronics. The synergy between chirality-driven spin control and perovskite semiconductors could enable multifunctional devices that seamlessly integrate charge and spin manipulation. Emerging studies reveal that CHPs exhibit long spin lifetimes, critical for maintaining spin coherence and enabling precise spin manipulation.[130-131] The compositional flexibility of CHPs allows for tailoring optical, electronic, and spin-related properties, further enhancing their appeal in potential applications including spin valves, spin transistors, and quantum computing.[132-134]

In this work, we synthesized QW-structured CHP with an ultra-high CD value (> 4000 mdeg) and transferred it to different substrates for study. Edge state, which remarkably enlarges the vertical carrier transport ability of CHP, is verified by the PL mapping. High mobility of the vertical structure is observed with the assistance of the SCLC method. Moreover, a high spin polarization degree of up to 90% is achieved, underlying the foundation for high-performance spintronics. Circularly polarized TA measurement is performed to study the spin carrier dynamics, and a long spin lifetime (> 500 ps) is obnserved in QW-structured CHP, which is far higher than the CHP film (< 10 ps). The built devices exhibit distinguishable states by modulating the magnetized polarization of the NiFe electrode, which exhibits great poetential in spin memory applications. This work designs a unique QW-structured CHP crystal, paving the way for high-performance spintronics.

5.2 Physical origin of chirality-induced spin selectivity

The CISS effect in CHPs stems from the intricate interplay between chiral structural motifs and SOC, establishing a unique mechanism for spin-selective charge transport. The concept of CISS was first introduced in the field of spintronics research. It was proposed as a novel phenomenon where the chirality of molecular species could impart significant spin selectivity to various electron processes. This concept has since been the subject of extensive research, aiming to understand the underlying mechanisms and explore potential applications in areas such as spintronic devices.[135]

In CHPs, the helical arrangement of chiral organic cations (**Figure 5.1a**)—such as *R/S*-α-methylbenzylamine (*R/S*-MBA) or 1-(1-naphthyl)ethylamine (NEA)—within the inorganic metal halide framework gives rise to an asymmetric electrostatic potential, forming a chiral electric field ($\vec{E}_{\text{chiral}}$). As an electron traverses this field, its motion induces a relativistic effective magnetic field ($\vec{B}$) in the electron's rest frame, described by the following fundamental relation:

$$\vec{B} = \frac{1}{c^2}\vec{v} \times \vec{E}_{\text{chiral}} \tag{5.1}$$

where $\vec{v}$ represents the electron velocity vector, and c is the speed of light in the vacuum. This magnetic field breaks the spin degeneracy of electrons, creating an energy splitting that favors the transmission of specific spin states.[136] For instance, in $(R/S\text{-MBA})_2\text{Pb}_{2.8}\text{Br}_{1.2}$ (**Figure 5.1b**), the chiral electric field generated by the helical organic cation layers produces a magnetic field that aligns electron spins parallel to the helical axis, enabling preferential transport of spin-polarized carriers (**Figure 5.1c**).[137]

In achiral halide perovskite, the dispersion relations of electrons and holes preserve both time-reversal symmetry and spatial inversion symmetry. These symmetries enforce a double degeneracy in the electronic (hole) sub-bands (**Figure 5.1d**).[110] The non-centrosymmetric crystal structure of CHPs disrupts inversion symmetry, thereby enhancing SOC and inducing spin-dependent band structure modifications. The spin-orbit coupling term in the Hamiltonian is given by:

$$\mathrm{H}_{\mathrm{SO}} = \lambda\vec{\sigma}(\vec{\mathrm{p}} \times \vec{\mathrm{E}}_{\text{chiral}}) \tag{5.2}$$

where λ is the spin-orbit coupling parameter, $\vec{\sigma} = (\sigma_x, \sigma_y, \sigma_z)$ are the Pauli matrices acting on the electron spin space, and $\vec{p}$ is the electron momentum vector.[138] This interaction results in spin-split energy sub-bands, described by the dispersion relation:

$$E^{\pm}(k) = \frac{\hbar^2 k^2}{2m} \pm \alpha_{\text{eff}} k \qquad 5.3$$

Here, $\hbar$ is the reduced Planck's constant, m is the effective mass of the electron, $k = |\vec{k}|$ is the magnitude of the electron wave vector, $\alpha_{\text{eff}} = \frac{\Delta E^{\pm}}{2k_0}$ is the spin splitting coefficient (with k_0 as a characteristic momentum), and $\Delta E^{\pm}$ denotes the energy difference between the spin-up (E^+) in **Figure 5.1e** and spin-down (E^-) in **Figure 5.1f** sub-bands at $k = k_0$. In materials like (R/S-NEA)$_2$PbBr$_4$, this SOC-induced band splitting enables selective transport of spin-up or spin-down electrons, with the preferential spin state dictated by the chiral configuration of the framework.

Chiral organic cations induce pronounced helical deformations in the inorganic lattice—for example, distorting the [PbBr$_4$]$^{2-}$ octahedra in(R/S-NEA)$_2$PbBr$_4$—leading to asymmetric bond angles ($\Delta\beta$) and lattice strain. This structural distortion enhances SOC and generates a chiral lattice potential that couples strongly with electron spin, giving rise to a spin polarization degree:

$$P_{\text{s}} = \frac{I_{+} - I_{-}}{I_{+} + I_{-}} \qquad 5.4$$

where I_+ and I_- are the electrical currents carried by spin-up and spin-down electrons, respectively. Notably, lead-free CHPs such as (R/S-MBA)$_2$SnI$_4$ exhibit spin polarization degrees exceeding 90%, attributed to the stronger lattice deformation and enhanced SOC from the heavier Sn^{2+} cation versus Pb^{2+} in traditional CHPs.[139]

In device applications, the CISS effect enables multifaceted spin filtering mechanisms. In spin-LEDs, CHPs function as spin filters, injecting spin-polarized holes into the emission layer. In spin valves, CHPs sandwiched between ferromagnetic electrodes could exhibit magnetoresistance responses with the response sign reversing upon inversion of the chiral configuration. The CISS effect also suppresses elastic backscattering of electrons, as spin-flip processes are energetically unfavourable, enhancing charge transport efficiency in spin transistors. This efficiency could be optimized by heterostructure design, such as coupling CHPs with topological insulators to extend spin diffusion lengths.

Theoretical models, including tight-binding and scattering calculations, reveal that CISS in CHPs is governed by structural parameters (helical pitch, radius) and SOC intensity.[140-141] Shorter pitches and larger radii in chiral lattices enhance spin polarization, while heavier metal ions or lattice distortions increase α_{eff}. This spin filtering capability, rooted in chiral electric fields, enhanced SOC, and helical lattice deformations, positions CHPs as promising materials for next-generation spintronic devices, including spin-based quantum computing and energy-efficient memory technologies.

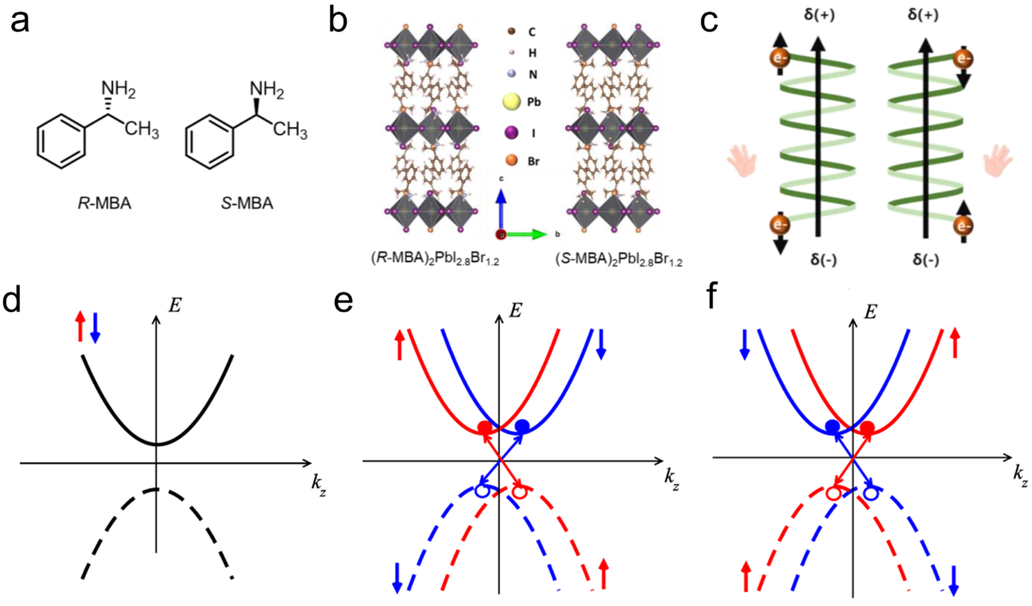

Figure 5.1 CISS in CHPs. (a) R-type and S-type chiral ligands. (b) Crystal structure of (R-

/S-MBA)$_2$PbI$_{2.8}$Br$_{1.2}$. (c) Sketch diagram of CISS effect.[137] (d) Band for achiral perovskite. (e) Spin-polarized sub-bands split in k-space with E^+. (f) Spin-polarized sub-bands split in k-space with E^-.[110]

5.3 Experimental section

Initially, an inverse temperature crystallization method was utilized to obtain MAPbBr$_3$ single crystal. MABr and PbBr$_2$ were dissolved into DMF, which was then filtered by polytetrafluoroethylene filter with pore size of 0.1 µm. The as-prepared solution was put in an oven, and the MAPbBr$_3$ crystals with different sizes were obtained as the temperature slowly cooled down. A clean process was performed by washing the surface of the crystal. After the drying, the MAPbBr$_3$ single crystal was encapsulated by the PDMS, which was prepared by a mixture of PDMS prepolymer and curing agent with a weight ratio of 10:1. In detail, the PDMS was dropped into the mold, followed by a baking process (50 °C, 12h). A cured PDMS protects the crystal in the next QW growth procedure. Quasi-2D (PEA)$_{1.2}$(S/RMBA)$_{0.8}$(MA)Pb$_3$I$_{10}$ ($n = 3$) was dissolved into the solvent as the precursor solution for the epitaxial growth. The Precursor was spin-coated on the MAPbBr$_3$, and then an annealing process in N$_2$ was implemented. After the annealing, the QW-structured CHP was obtained.

5.4 Result and discussion

Figure 5.2a shows the transfer process of the QW. Thermal release tape (TRT) is attached to the QW growth area, and then the TRT is detached from the surface of the MAPbBr$_3$ crystal. **Figure 5.2b** plots the XRD of the crystal, and the peaks are consistent with typical characteristics of $MAPbBr_3$, suggesting that high-quality $MAPbBr_3$ serves an important role in synthesizing QW. After the exfoliation of the QW, the TRT is stuck on the target substrate. To remove the TRT, the as-prepared sample is baked in the glove box at 100 °C, over the threshold temperature of the tape. After a change of tape color, the TRT possesses low adhesion and can be easily removed by the tweezer, leaving the QW on the substrate. Chiral ligands (**Figure 5.2c**) including R-MBA and S-MBA are utilized to synthesize the chiral QW. In the cross structure, the side along the vertical direction features an edge state with a high carrier mobility, while the planar direction shows a weak conduction ability owing to the insulating ligands. To characterize the surface morphology, we conduct the AFM measurement (**Figure 5.2d**), and the obtained QW exhibits crisscross network structure. The cross-sectional SEM image in **Figure 5.2e** demonstrates that the height of the transferred QW is approximately 1.5 μm.

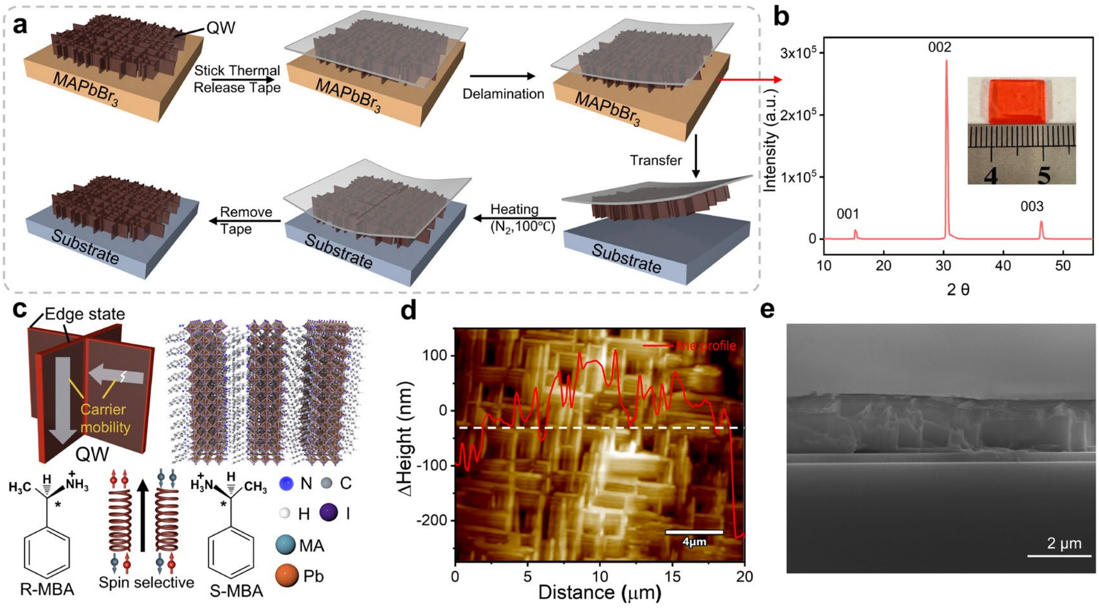

Figure 5.2 Characterization of QW structure. (a) Transfer process of QW. (b) XRD of the $MAPbBr_3$ single crystal. (c) Edge state of the cross QW. (d) AFM image and corresponding line profile extracted along the white dash line. (e) Cross-section SEM image of the

transferred QW on SiO_2/Si substrate.

Moreover, the chiroptical properties of R/S-QW are checked. In **Figure 5.3a**, the chiral QW shows a wide range of absorbance and PL peak around 715 nm, which conforms to the RP phase (n = 3). **Figure 5.3b** is the optical image of large area QW on the quartz, and the CD is measured with a transmission mode. **Figure 5.3c** and **5.3d** picture the transmitted intensity of CPL with different handedness through R/S-QW. The CD is calculated and plotted as shown in **Figure 5.3e**, and the QW exhibits an obvious cotton effect and a high CD value over 4000 mdeg. The g_{CD} (**Figure 5.3f**) is also calculated, and the QW attains a high factor of 0.2, indicating superior chiroptical properties.

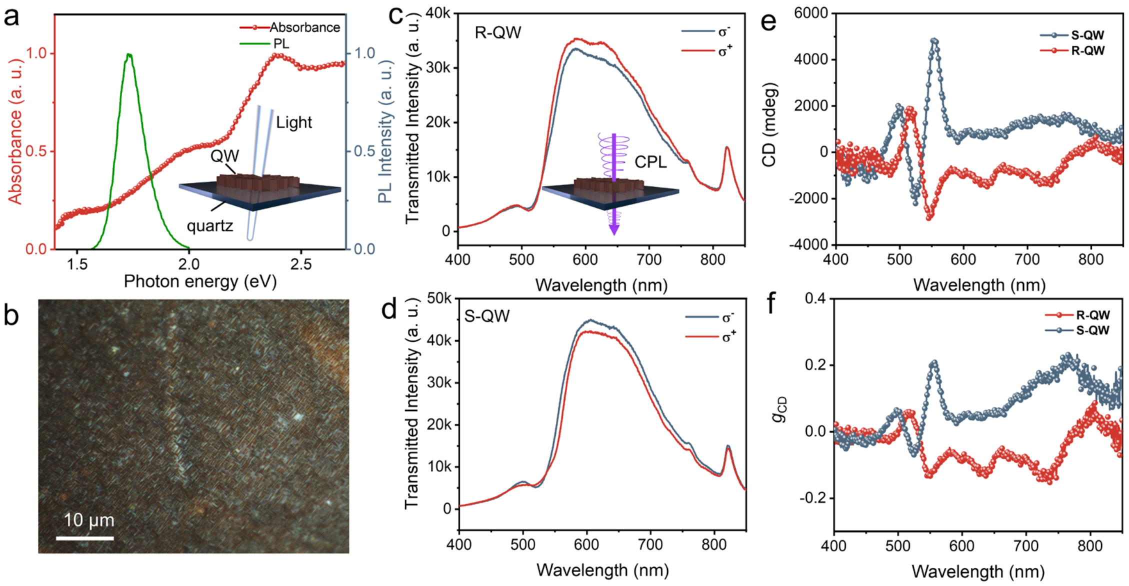

Figure 5.3 Chiroptical properties of CHP QW. (a) PL and absorbance of QW on quartz. (b) Optical image of large area QW. (c) CPL transmitted intensity through R-QW. (d) CPL transmitted intensity through S-QW. (e) CD spectra of CHP QW. (f) Calculated g_{CD} of CHP QW.

When carriers traverse helical potentials, they generate an effective magnetic field. The direction of this induced magnetic field depends on the chirality of the helix and plays a critical role in governing carrier transport dynamics. Specifically, carriers with spins aligned to the magnetic field experience preferential transport, while those with opposing spins are hindered. This spin-selective transport mechanism, termed the CISS effect, is explored using mc-AFM (**Figure 5.4a**). A HQ NSC18 tip (spring constant, 2.8 N/m) is utilized in contact mode and the Co-Cr tip is magnetized by a permanent magnet for more than 30 minutes and then is adopted for measurement. The $\mathrm{Tip_{up}}$ and $\mathrm{Tip_{down}}$ refer to the current with the magnetic north pole up and down, respectively. The voltage-current curves are collected with a frequency of 1 Hz and ramping the voltage from -2 V to 2 V. For S-QW, carriers with spin down state are easy to pass through as shown in **Figure 5.4b** while the R-QW shows an opposite preference (**Figure 5.4c**). The QW exhibits a bias-dependent spin polarization and achieves a high spin polarization (*P*) over 90% according to the calculation equation in **Figure 5.4d**, demonstrating great potential for high-performance spintronics.

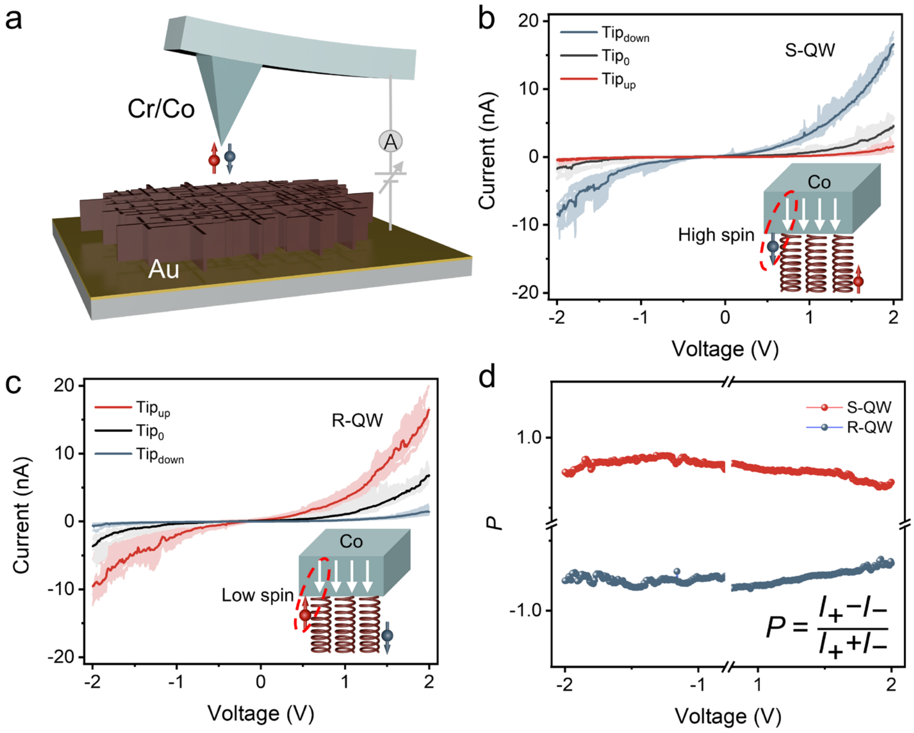

Figure 5.4 Chiral-induced spin selectivity. (a) Sketch diagram of mc-AFM measurement. (b) Current-voltage curves of S-QW/Au. (c) Current-voltage curves of R-QW/Au. (d) Bias-dependent spin-polarization for R-QW and S-QW.

To explore the underlying mechanisms for the excellent CISS behavior, we perform the CPL-pumped TA measurement. The S-QW is pumped by the LCP, and the photophysical process is probed by RCP (**Figure 5.5a**) and LCP (**Figure 5.5b**), respectively. The GSB signals are extracted and compared in **Figure 5.5c**, and the same pump-probe set exhibits a higher intensity than the counterpart configuration. The net spin is calculated and plotted in **Figure 5.5d**, and the QW shows a high spin lifetime of about 581 ps, which is much higher than conventional CHP.

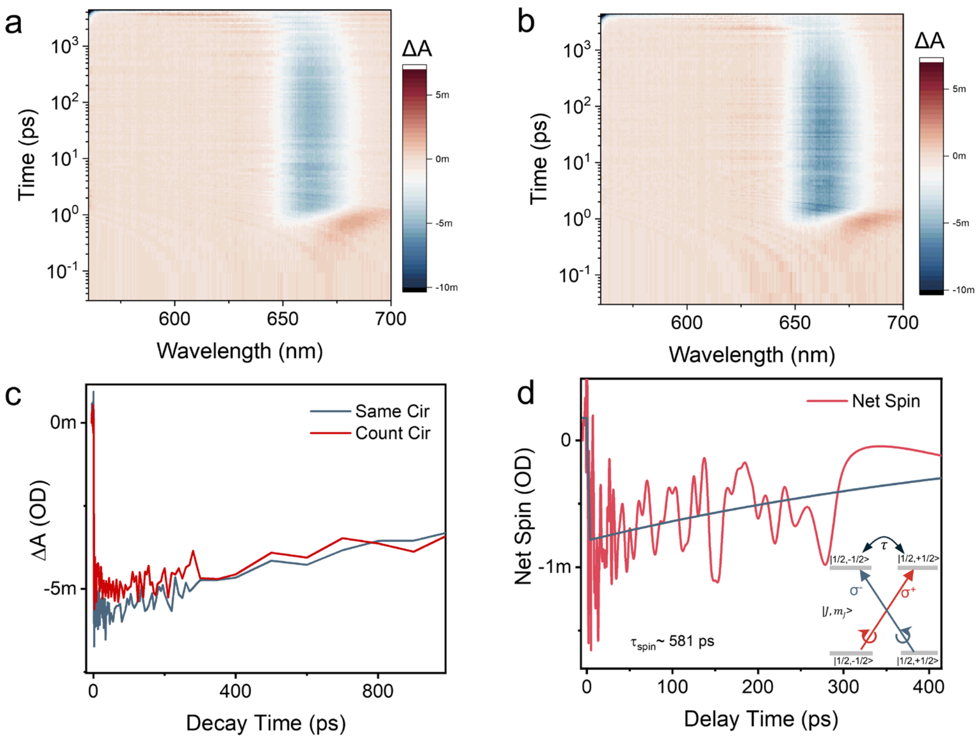

Figure 5.5 CPL-pumped TA. (a) LCP-pumped mapping spectra of S-QW. (b) RCP-pumped mapping spectra of S-QW. (c) GSB dynamics of S-QW under 550 nm CPL (50 nW) with

different handedness. (d) Spin-coherence dynamics in S-QW. The spin lifetime is calculated by $\frac{\sigma^{+}-\sigma^{-}}{\sigma^{+}+\sigma^{-}}$, where σ^{+} and σ^{-} are probe signals with different handedness under same CPL pump.

CHP films usually possess much defect, which induces a low carrier mobility. The edge state of the QW enables it to be a promising candidate for constructing vertical structure devices as shown in **Figure 5.6a**. We measure carrier mobility via the space-charge-limited current technique.

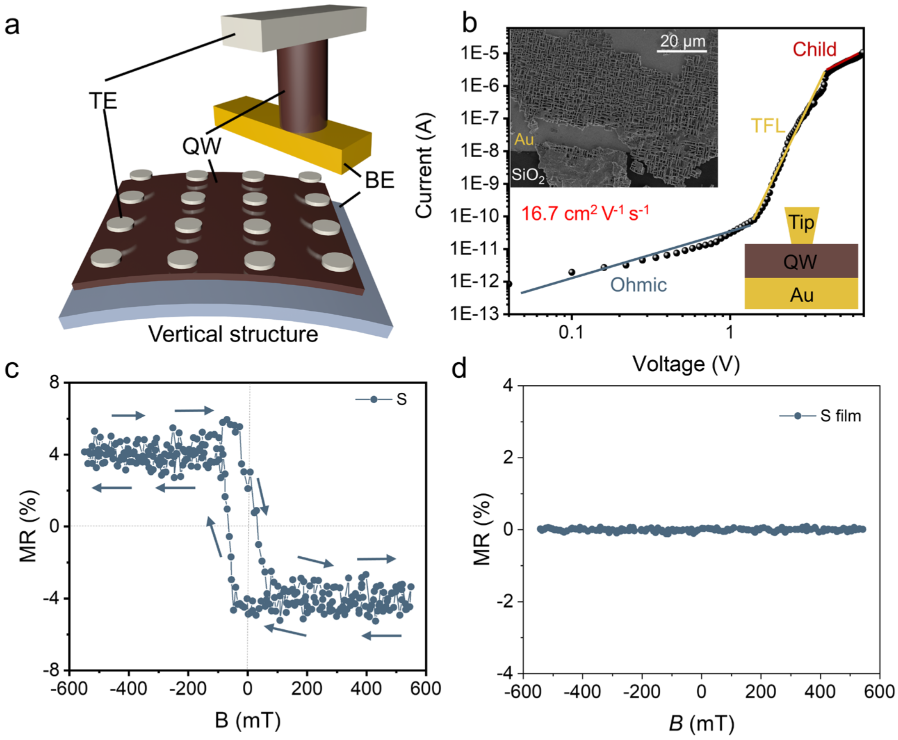

Figure 5.6 Electronic performance of QW-based crosspoint device. (a) Typical vertical structures for memory devices. (b) Carrier mobility measured by SCLC method. (c) MR response of FeNi/R-QW/Au device under sweeping magnetic field. (d) MR response of FeNi/R-film/Au device under sweeping magnetic field.

Typically, a sandwiched structure of Au/QW/Au that forms hole-only device is fabricated and the dark current is measured under applied bias. Three regions could be obviously seen in the analysis (**Figure 5.6b**). In the first region, the device exhibits an ohmic conductive behavior at low bias. The second part is trap-filling region, and the current increases rapidly when the voltage exceeds over trap-filled limit voltage (V_{TFL}). The third region is a trap-free state at high bias, and the hole mobility is calculated according to Mott-Gurney's law,

$$\mu = \frac{8J_D L^3}{9\varepsilon\varepsilon_0 V^2} \qquad 5.5$$

where J_D is current density, L is thickness of QW, and V is the applied voltage. The QW shows a high mobility of 16.7cm^2 V^{-1} s^{-1}, which is much higher than conventional RP single crystal (n=3). Additionally, the ferromagnetic electrode is deposited onto the QW, and the constructed Au/QW/NiFe exhibits obvious MR response (**Figure 5.6c**) under an out-of-plane external magnetic field compared with the film-type device (**Figure 5.6d**). The spin polarization of the injected carriers is related to the magnetization of the ferromagnetic electrode, and the MR response follows the hysteresis loop of the FeNi electrode. This high MR value at RT paves the way for constructing high-performance spintronic devices.

5.5 Summary

In this work, QW-structured CHP with a high CD (> 4000 mdeg) was prepared and transferred to different substrates for study. The edge state exhibited by the QW supports remarkable conductive performance along the vertical direction of the QW. Further, the SCLC method demonstrates a high mobility of the QW about 16.7cm^2 V^{-1} s^{-1}, which is much higher than RP single crystal (n=3) with an average mobility less than 1 cm^2 V^{-1} s^{-1}. In mc-AFM measurement, the QW exhibits high spin polarization over 90%. Circularly polarized TA further verifies the long spin lifetime (> 500 ps), which contributes to high-performance spin-dependent applications. The CHP QW is expected to promote the development of chiral perovskite in advanced technologies including spin valve, nonvolatile memory, logic operation and in-sensor computing.

Chapter 6 Conclusions and Future work

6.1 Conclusions

Chiral perovskites have been a captivating area of research due to their remarkable optoelectronic properties and unique chiroptical features, holding immense promises for advancements across diverse technological domains. In this thesis, we achieved three kinds of CHP-based devices with different architecture and their applications in terms of exhibiting chiroptical properties. CPL-resolved PAS device with R-/S-$MBAPbI_3$, full-Stokes PAS device with (R-/S-$MBA)_2PbI_4$ NW, and spin devices with quantum-wall structured CHP are proposed and studied. Those works provide prototypes for the development of high-performance chiroptical devices.

Firstly, we demonstrated a circular polarization-sensitive heterostructure with excellent CPL-modulated neuromorphic behavior. The heterostructure was composed of H-PVK with a high CD and SNWTs with good conductivity, achieving high photoresponsivity above 240 mA/W at 395 nm. Moreover, this heterostructure could serve as PAS and imitate biological synaptic activities, enabling typical synaptic characteristics such as EPSC, PPF, SFDP, STP, and LTP. Specifically, the PAS device was assembled as an array, and achieves CPL-dependent image perception, learning, and recognition, exhibiting great advantages in polarized imaging and encrypted communication. Additionally, this PAS could be utilized to simulate the SNNs that are capable of vision perception and recognition owing to its excellent temporal information encoding features. This work provides a CPL-sensitive heterojunction device with great potential in a broad spectrum of advanced technologies, such as CPL-modulated storage, sensor, neuromorphic computing as well as detector technologies.

Secondly, we, for the first time, achieved full-Stokes polarization sensing, memory, and computing based on the chiral PVK NW with high circular dichroism (> 400 mdeg) and intrinsic linear dichroism. The chiral PVK NW/MXene heterostructure exhibits long-term charge storage as verified via ultrafast transient absorption measurements and highly sensitive polarization-dependent photodetection, thereby enabling energy-efficient and highly sensitive full-Stokes polarization-resolved neuromorphic behaviors (~0.5 pJ per synaptic event, 2.3 A/W responsivity). Significantly, the polarization-dependent reservoir computing is developed based on the PAS device, and achieves a low normalized root mean square error of 0.023 in the chaotic forecasting task. These findings underscore the pivotal role of chiral perovskites in advancing PAS technology and their potential to contribute to polarization-dependent nanoscale neuromorphic vision systems.

Thirdly, quantum well-structured CHP was prepared and studied in detail. A transfer of the synthesized quantum well was achieved, which contributed to multifunctional applications. Ultra-large CD (>4000 mdeg) was demonstrated by the designed micro-region absorbance measurement system. Additionally, high mobility was verified by the SCLC method, and the quantum well-structured CHP exhibits vertical conductivity preference, which shows great potential in constructing high-density crossbar array without a selector. More importantly, the CHP achieves high spin polarization degree (~90%) and the constructed CHP-based devices exhibits tunable states by controlling the magnetization of top electrode, paving the way for the development of next-generation spintronics.

6.2 Future work

We demonstrate CHPs-based sensing detectors and full-Stokes polarimeters with excellent responsivity and superior detectivity, and QW structured CHP with superior spin-dependent behavior. However, there are several problems that should be addressed in the future study.

(1) The tunable bandgap of perovskites (visible to near-infrared) caters to the demands of broad wavelength detection and solution-based methods can be employed to produce flexible chiral detectors for wearable devices. Despite their promise, CHP films face challenges including high dark currents, requiring improved defect passivation techniques. Scalable fabrication of polarization-sensitive arrays remains immature. Additionally, their performance degrades under moisture, necessitating robust encapsulation strategies. Future efforts should pay much attention to structure-optimized intelligent CPL detectors that integrate sensing of polarization, wavelength, and spin information.

(2) In addition to the CPL sensing detector, CHPs also show tremendous advantages in constructing CPL sensing PAS. Dynamically adjusting synaptic connection strength can be achieved through variations in the frequency, intensity, and polarization of light pulses, supporting learning rules such as spike-timing-dependent plasticity (STDP). By combining multi-parameter optical inputs such as wavelength, polarization, and intensity, advanced PAS can be constructed, imitating the diverse regulatory mechanisms of biological synapses and achieving energy-efficient neuromorphic computing. However, current works of CHPs-based PAS focus on a single device, and PAS arrays that serve as hardware for accelerating computation in AI are lacked. Future work should focus on the large-scale array fabrication and CMOS compatibility.

(3) For spintronics, CHPs with high spin polarization degrees enable the development of RT magnetic-free spin transistors and spin memory devices. By utilizing spin currents instead of traditional charge currents, these materials hold immense promise for reducing energy consumption, as demonstrated in innovative spin logic gates. However, several challenges remain in CHPs for spintronics. A key hurdle is the short spin lifetime. Additionally, the microscopic mechanisms of CISS, including the roles of spin-orbit coupling and chiral field effects, are not yet clear. CISS-induced electric behavior measured by mc-AFM or four-probe configuration has been widely reported while further device-level applications such as spin-transistors and spin logic gates are insufficient. Designing systems with SOC, combined with topological insulators or 2D materials, for extending spin diffusion lengths of CHPs is necessary. Meanwhile, more exploration should be focused on the applications of CHPs-based devices in spin memory, computing, and quantum fields.

References

[1] X. Zhang, Y. Xu, C. Valenzuela, X. Zhang, L. Wang, W. Feng, Q. Li, *Light: Science & Applications* **2022**, 11, 223.
[2] I. C. Seo, Y. Lim, S.-C. An, B. H. Woo, S. Kim, J. G. Son, S. Yoo, Q. H. Park, J. Y. Kim, Y. C. Jun, *ACS Nano* **2021**, 15, 13781.
[3] N. Fiuza-Maneiro, J. Mendoza-Carreño, S. Gómez-Graña, M. I. Alonso, L. Polavarapu, A. Mihi, *Advanced Materials* **2024**, 36, 2413967.
[4] X. Zhang, L. Li, Y. Chen, C. Valenzuela, Y. Liu, Y. Yang, Y. Feng, L. Wang, W. Feng, *Angewandte Chemie* **2024**, 136, e202404202.
[5] T. Duan, Y. Zhou, *Advanced Energy Materials* **2023**, 13, 2200792.
[6] M. W. Heindl, T. Kodalle, N. Fehn, L. K. Reb, S. Liu, C. Harder, M. Abdelsamie, L. Eyre, I. D. Sharp, S. V. Roth, *Advanced Optical Materials* **2022**, 10, 2200204.
[7] B. Shen, Y. Kim, M. Lee, *Advanced Materials* **2020**, 32, 1905669.
[8] Y.-H. Kim, R. Song, J. Hao, Y. Zhai, L. Yan, T. Moot, A. F. Palmstrom, R. Brunecky, W. You, J. J. Berry, J. L. Blackburn, M. C. Beard, V. Blum, J. M. Luther, *Advanced Functional Materials* **2022**, 32, 2200454.
[9] S. Li, D. Chen, B. Li, H. Yan, B. J. Lawrie, B. Choi, D. Rhee, Y. Li, H. Zhao, L. Chen, *Journal of the American Chemical Society* **2025**.
[10] H. Y. Hou, S. Tian, H. R. Ge, J. D. Chen, Y. Q. Li, J. X. Tang, *Advanced Functional Materials* **2022**, 32, 2209324.
[11] H. Lu, Z. V. Vardeny, M. C. Beard, *Nature Reviews Chemistry* **2022**, 6, 470.
[12] Q. Wei, Z. Ning, *ACS Materials Letters* **2021**, 3, 1266.
[13] S. Ma, J. Ahn, J. Moon, *Advanced Materials* **2021**, 33, 2005760.
[14] Y. Xu, W. Mi, *Materials Horizons* **2023**, 10, 1924.
[15] M. Wang, Z. Yang, C. Zhang, *Advanced Optical Materials* **2021**, 9, 2002236.
[16] B. Tang, S. Wang, H. Liu, N. Mou, A. S. Portniagin, P. Chen, Y. Wu, X. Gao, D. Lei, A. L. Rogach, *Advanced Optical Materials* **2024**, 12, 2301524.
[17] M. Li, F. Fang, X. Huang, G. Liu, Z. Lai, Z. Chen, J. Hong, Y. Chen, R.-j. Wei, G.-H. Ning, *Chemistry of Materials* **2022**, 34, 2955.
[18] Z. Zhang, W. Liang, J. Xue, X. Li, K. Wu, H. Lu, *ACS Nano* **2024**, 18, 5890.
[19] J.-T. Lin, D.-G. Chen, L.-S. Yang, T.-C. Lin, Y.-H. Liu, Y.-C. Chao, P.-T. Chou, C.-W. Chiu, *Angewandte Chemie International Edition* **2021**, 60, 21434.
[20] S. Yang, G. Jang, C. U. Lee, J. Son, J. Lee, W. Jeong, D. G. Roe, J. H. Cho, J. Moon, *Advanced Functional Materials* **2024**, 34, 2310917.
[21] L. Yao, K.-H. Xue, H. Tong, C. Chen, G. Niu, W. Yang, J. Tang, *Crystal Growth & Design* **2022**, 22, 5552.
[22] G. Park, D. Y. Jeong, S. Y. Yu, J. J. Park, J. H. Kim, H. Yang, Y. You, *Angewandte Chemie International Edition* **2023**, 62, e202309762.
[23] G. Park, D. Y. Jeong, S. Y. Yu, J. J. Park, J. H. Kim, H. Yang, Y. You, *Angewandte Chemie International Edition* **2023**, 62, e202309762.
[24] C. Wang, L. Ma, S. Wang, G. Zhao, *The Journal of Physical Chemistry Letters* **2021**, 12, 12129.
[25] Y. Liu, Y. Jiang, Z. Xu, L. Li, D. Zhang, W. Zheng, D. Liang, B. Zheng, H. Liu, X. Sun, *Advanced Optical Materials* **2022**, 10, 2200183.
[26] W. Choi, M. Kwak, J. Park, H. Kim, J. Kim, Y. Seo, D. Yoo, J. H. Oh, *Chemical Engineering Journal*

2024, 498, 155504.

[27] A. Ishii, T. Miyasaka, *Science Advances* **2020**, 6, eabd3274.

[28] T. Tong, Y. Gan, W. Li, W. Zhang, H. Song, H. Zhang, K. Liao, J. Deng, S. Li, Z. Xing, *ACS Nano* **2022**, 17, 530.

[29] C. Fang, H. Wang, Z. Shen, H. Shen, S. Wang, J. Ma, J. Wang, H. Luo, D. Li, *ACS Applied Materials & Interfaces* **2019**, 11, 8419.

[30] Q. Liu, S. Gao, Y. Li, W. Yue, C. Zhang, H. Kan, G. Shen, *Advanced Materials Technologies* **2023**, 8, 2201143.

[31] J. T. DuBose, P. V. Kamat, *Journal of the American Chemical Society* **2020**, 142, 5362.

[32] M. Abdi-Jalebi, M. Ibrahim Dar, S. P. Senanayak, A. Sadhanala, Z. Andaji-Garmaroudi, L. M. Pazos-Outón, J. M. Richter, A. J. Pearson, H. Sirringhaus, M. Grätzel, *Science Advances* **2019**, 5, eaav2012.

[33] G. Ren, W. Han, Y. Deng, W. Wu, Z. Li, J. Guo, H. Bao, C. Liu, W. Guo, *Journal of Materials Chemistry A* **2021**, 9, 4589.

[34] W. Yu, F. Li, L. Yu, M. R. Niazi, Y. Zou, D. Corzo, A. Basu, C. Ma, S. Dey, M. L. Tietze, U. Buttner, X. Wang, Z. Wang, M. N. Hedhili, C. Guo, T. Wu, A. Amassian, *Nature Communications* **2018**, 9, 5354.

[35] M. Vasilopoulou, A. R. b. Mohd Yusoff, Y. Chai, M.-A. Kourtis, T. Matsushima, N. Gasparini, R. Du, F. Gao, M. K. Nazeeruddin, T. D. Anthopoulos, Y.-Y. Noh, *Nature Electronics* **2023**, 6, 949.

[36] Q. Qian, H. Ren, J. Zhou, Z. Wan, J. Zhou, X. Yan, J. Cai, P. Wang, B. Li, Z. Sofer, B. Li, X. Duan, X. Pan, Y. Huang, X. Duan, *Nature* **2022**, 606, 902.

[37] J. Wang, C. Zhang, H. Liu, R. McLaughlin, Y. Zhai, S. R. Vardeny, X. Liu, S. McGill, D. Semenov, H. Guo, R. Tsuchikawa, V. V. Deshpande, D. Sun, Z. V. Vardeny, *Nature Communications* **2019**, 10, 129.

[38] C. Kulkarni, A. K. Mondal, T. K. Das, G. Grinbom, F. Tassinari, M. F. J. Mabesoone, E. W. Meijer, R. Naaman, *Advanced Materials* **2020**, 32, 1904965.

[39] N. Giaconi, M. Lupi, T. K. Das, A. Kumar, L. Poggini, C. Viglianisi, L. Sorace, S. Menichetti, R. Naaman, R. Sessoli, *Journal of Materials Chemistry C* **2024**, 12, 10029.

[40] R. Malatong, T. Sato, J. Kumsampao, T. Minato, M. Suda, V. Promarak, H. M. Yamamoto, *Small* **2023**, 19, 2302714.

[41] M. Suda, Y. Thathong, V. Promarak, H. Kojima, M. Nakamura, T. Shiraogawa, M. Ehara, H. M. Yamamoto, *Nature Communications* **2019**, 10, 2455.

[42] J. Ma, C. Fang, C. Chen, L. Jin, J. Wang, S. Wang, J. Tang, D. Li, *Acs Nano* **2019**, 13, 3659.

[43] S. Shrestha, M. Li, S. Park, X. Tong, D. DiMarzio, M. Cotlet, *Nature Communications* **2023**, 14, 5234.

[44] Z. Liu, C. Zhang, X. Liu, A. Ren, Z. Zhou, C. Qiao, Y. Guan, Y. Fan, F. Hu, Y. S. Zhao, *Advanced Science* **2021**, 8, 2102065.

[45] C. Wang, Q. Wei, H. Ren, K. L. Wong, Q. Liu, L. Zhou, P. Wang, S. Cai, J. Yin, M. Li, *Advanced Materials* **2025**, 37, 2413839.

[46] Y. Liu, X. Duan, H.-J. Shin, S. Park, Y. Huang, X. Duan, *Nature* **2021**, 591, 43.

[47] L. Yu, M. Gao, Q. Lv, H. Ma, J. Shang, Z.-H. Huang, Z. Sun, T. Yu, F. Kang, R. Lv, *ACS Nano* **2024**, 18, 33131.

[48] H. Min, N. Wang, N. Chen, Y. Tong, Y. Wang, J. Wang, J. Liu, S. Wang, X. Wu, P. Yang, H. Shi, C. Zhuo, Q. Chen, J. Li, D. Zhang, X. Lu, C. Zhu, Q. Peng, L. Zhu, J. Chang, W. Huang, J. Wang, *Nature Nanotechnology* **2024**, 19, 632.

[49] N.-G. Park, K. Zhu, *Nature Reviews Materials* **2020**, 5, 333.

[50] W. Kim, H. Kim, T. J. Yoo, J. Y. Lee, J. Y. Jo, B. H. Lee, A. A. Sasikala, G. Y. Jung, Y. Pak, *Nature Communications* **2022**, 13, 720.

[51] Y. Han, J. Fu, Z. Ren, J. Yu, Q. Liang, Z. Xu, X. Xie, D. Li, R. Ma, M. Cao, Y. Sun, C. Yang, J. He, X.

Chang, K. Liu, P. W. K. Fong, J. Huang, H. Liu, Z. Liu, D. Xu, L. Cheng, J. Zhang, G. Yang, X. Lu, Y. Zhu, Q. Tai, Q. Lin, H. Hu, Y. Yang, G. Li, *Nature Energy* **2025**.

[52] C. Chen, L. Gao, W. Gao, C. Ge, X. Du, Z. Li, Y. Yang, G. Niu, J. Tang, *Nature Communications* **2019**, 10, 1927.

[53] S. Dan, S. Paramanik, A. J. Pal, *ACS Nano* **2024**, 18, 14457.

[54] H. Shim, F. Ershad, S. Patel, Y. Zhang, B. Wang, Z. Chen, T. J. Marks, A. Facchetti, C. Yu, *Nature Electronics* **2022**, 5, 660.

[55] W. Huang, X. Xia, C. Zhu, P. Steichen, W. Quan, W. Mao, J. Yang, L. Chu, X. a. Li, *Nano-Micro Letters* **2021**, 13, 1.

[56] Y. Wang, M.-S. Song, J. Zhao, Z. Li, T. Wang, H. Wang, H.-Y. Wang, Y. Wang, *ACS Nano* **2024**, 18, 22334.

[57] Y.-H. Kim, Y. Zhai, H. Lu, X. Pan, C. Xiao, E. A. Gaulding, S. P. Harvey, J. J. Berry, Z. V. Vardeny, J. M. Luther, *Science* **2021**, 371, 1129.

[58] H. Gu, H. Xu, C. Yang, Y. Feng, G. Gao, R. L. Z. Hoye, X. Hu, L. Polavarapu, G. Zhou, X.-F. Jiang, *Nano Letters* **2024**, 24, 13333.

[59] P. Li, Z. Zhou, G. Ran, T. Zhang, Z. Jiang, H. Liu, W. Zhang, Y. Yan, J. Yao, H. Dong, Y. S. Zhao, *Nature Communications* **2024**, 15, 10880.

[60] Y. Chen, J. Feng, Y. Huang, W. Chen, R. Su, S. Ghosh, Y. Hou, Q. Xiong, C.-W. Qiu, *Nature Materials* **2023**, 22, 1065.

[61] W. Lin, C. Yang, Y. Miao, S. Li, L. Zhang, X. F. Jiang, Y. Lv, B. Poudel, K. Wang, L. Polavarapu, *Advanced Materials* **2023**, 35, 2301573.

[62] X. Liu, K. Wang, T. Zhang, H. Liu, A. Ren, S. Ren, P. Li, C. Zhang, J. Yao, Y. S. Zhao, *Advanced Materials* **2023**, 35, 2305260.

[63] K. Łempicka-Mirek, M. Król, L. De Marco, A. Coriolano, L. Polimeno, I. Viola, M. Kędziora, M. Muszyński, P. Morawiak, R. Mazur, *Nanophotonics* **2024**, 13, 2659.

[64] Z. Wang, X. Qiu, H. Wang, W. Zhao, S. Gull, H. Lu, Z. Hao, B. Sun, X. Zeng, X. Liu, *Angewandte Chemie* **2025**, 137, e202420249.

[65] A. Maiti, A. J. Pal, *Angewandte Chemie* **2022**, 134, e202214161.

[66] S. Chen, M. R. Mahmoodi, Y. Shi, C. Mahata, B. Yuan, X. Liang, C. Wen, F. Hui, D. Akinwande, D. B. Strukov, *Nature Electronics* **2020**, 3, 638.

[67] J.-K. Han, D.-M. Geum, M.-W. Lee, J.-M. Yu, S. K. Kim, S. Kim, Y.-K. Choi, *Nano Letters* **2020**, 20, 8781.

[68] F. Zhou, Z. Zhou, J. Chen, T. H. Choy, J. Wang, N. Zhang, Z. Lin, S. Yu, J. Kang, H.-S. P. Wong, *Nature Nanotechnology* **2019**, 14, 776.

[69] K. Roy, A. Jaiswal, P. Panda, *Nature* **2019**, 575, 607.

[70] Q. Yu, H. Tang, K. C. Tan, H. Yu, *Neurocomputing* **2014**, 138, 3.

[71] Z. Wang, S. Joshi, S. E. Savel'ev, H. Jiang, R. Midya, P. Lin, M. Hu, N. Ge, J. P. Strachan, Z. Li, Q. Wu, M. Barnell, G.-L. Li, H. L. Xin, R. S. Williams, Q. Xia, J. J. Yang, *Nature Materials* **2017**, 16, 101.

[72] Q. Liu, S. Gao, L. Xu, W. Yue, C. Zhang, H. Kan, Y. Li, G. Shen, *Chemical Society Reviews* **2022**, 51, 3341.

[73] M. Lee, S. Nam, B. Cho, O. Kwon, H. U. Lee, M. G. Hahm, U. J. Kim, H. Son, *Nano Letters* **2021**, 21, 7879.

[74] Z. Cheng, C. Ríos, W. H. Pernice, C. D. Wright, H. Bhaskaran, *Science Advances* **2017**, 3, e1700160.

[75] A. Altaqui, P. Sen, H. Schrickx, J. Rech, J.-W. Lee, M. Escuti, W. You, B. J. Kim, R. Kolbas, B. T. O'Connor, *Science Advances* **2021**, 7, eabe3196.

[76] W. Ma, L. Xu, A. F. de Moura, X. Wu, H. Kuang, C. Xu, N. A. Kotov, *Chemical Reviews* **2017**, 117, 8041.

[77] Y. Dang, X. Liu, B. Cao, X. Tao, *Matter* **2021**, 4, 794.

[78] J. Ma, H. Wang, D. Li, *Advanced Materials* **2021**, 33, 2008785.

[79] F. Pop, N. Zigon, N. Avarvari, *Chemical reviews* **2019**, 119, 8435.

[80] S. D. Namgung, R. M. Kim, Y.-C. Lim, J. W. Lee, N. H. Cho, H. Kim, J.-S. Huh, H. Rhee, S. Nah, M.-K. Song, *Nature Communications* **2022**, 13, 5081.

[81] X. Fu, Z. Zeng, S. Jiao, X. Wang, J. Wang, Y. Jiang, W. Zheng, D. Zhang, Z. Tian, Q. Li, *Nano Letters* **2023**, 23, 606.

[82] D. Han, C. Li, C. Jiang, X. Jin, X. Wang, R. Chen, J. Cheng, P. Duan, *Aggregate* **2022**, 3, e148.

[83] S. Liu, M. W. Heindl, N. Fehn, S. Caicedo-Dávila, L. Eyre, S. M. Kronawitter, J. Zerhoch, S. Bodnar, A. Shcherbakov, A. Stadlbauer, *Journal of the American Chemical Society* **2022**, 144, 14079.

[84] D. Fu, J. Xin, Y. He, S. Wu, X. Zhang, X. M. Zhang, J. Luo, *Angewandte Chemie International Edition* **2021**, 60, 20021.

[85] T. Liu, W. Shi, W. Tang, Z. Liu, B. C. Schroeder, O. Fenwick, M. J. Fuchter, *ACS Nano* **2022**, 16, 2682.

[86] J. Hao, H. Lu, L. Mao, X. Chen, M. C. Beard, J. L. Blackburn, *ACS Nano* **2021**, 15, 7608.

[87] S. N. Habisreutinger, R. J. Nicholas, H. J. Snaith, *Advanced Energy Materials* **2017**, 7, 1601839.

[88] J. Wei, C. Xu, B. Dong, C.-W. Qiu, C. Lee, *Nature Photonics* **2021**, 15, 614.

[89] A. Basiri, X. Chen, J. Bai, P. Amrollahi, J. Carpenter, Z. Holman, C. Wang, Y. Yao, *Light: Science & Applications* **2019**, 8, 78.

[90] N. A. Rubin, G. D'Aversa, P. Chevalier, Z. Shi, W. T. Chen, F. Capasso, *Science* **2019**, 365, eaax1839.

[91] T. W. Cronin, *Current Zoology* **2018**, 64, 513.

[92] M. Garcia, C. Edmiston, R. Marinov, A. Vail, V. Gruev, *Optica* **2017**, 4, 1263.

[93] X. Wang, Y. Wang, W. Gao, L. Song, C. Ran, Y. Chen, W. Huang, *Advanced Materials* **2021**, 33, 2003615.

[94] J. Pan, Y. Wu, X. Zhang, J. Chen, J. Wang, S. Cheng, X. Wu, X. Zhang, J. Jie, *Nature Communications* **2022**, 13, 6629.

[95] D. Xie, G. Gao, B. Tian, Z. Shu, H. Duan, W. W. Zhao, J. He, J. Jiang, *Advanced Materials* **2023**, 35, 2212118.

[96] Q. Liu, Q. Wei, H. Ren, L. Zhou, Y. Zhou, P. Wang, C. Wang, J. Yin, M. Li, *Nature Communications* **2023**, 14, 7179.

[97] X. Duan, Z. Cao, K. Gao, W. Yan, S. Sun, G. Zhou, Z. Wu, F. Ren, B. Sun, *Advanced Materials* **2024**, 36, 2310704.

[98] H.-S. Zhang, X.-M. Dong, Z.-C. Zhang, Z.-P. Zhang, C.-Y. Ban, Z. Zhou, C. Song, S.-Q. Yan, Q. Xin, J.-Q. Liu, Y.-X. Li, W. Huang, *Nature Communications* **2022**, 13, 4996.

[99] Z. Lv, Y. Wang, J. Chen, J. Wang, Y. Zhou, S.-T. Han, *Chemical reviews* **2020**, 120, 3941.

[100] X.-Q. Sun, W.-J. Zhang, C.-J. Zhang, L.-X. You, G.-Z. Xu, J. Huang, H. Zhou, H. Li, Z. Wang, X.-M. Xie, *Optic Express* **2021**, 29, 11021.

[101] J. Zuo, J. Bai, S. Choi, A. Basiri, X. Chen, C. Wang, Y. Yao, *Light: Science & Applications* **2023**, 12, 218.

[102] W. Luo, Q. Weng, M. Long, P. Wang, F. Gong, H. Fang, M. Luo, W. Wang, Z. Wang, D. Zheng, W. Hu, X. Chen, W. Lu, *Nano Letters* **2018**, 18, 5439.

[103] J. Wang, M. S. Gudiksen, X. Duan, Y. Cui, C. M. Lieber, *Science* **2001**, 293, 1455.

[104] J. Ahn, K. Ko, J.-h. Kyhm, H.-S. Ra, H. Bae, S. Hong, D.-Y. Kim, J. Jang, T. W. Kim, S. Choi, J.-H. Kang, N. Kwon, S. Park, B.-K. Ju, T.-C. Poon, M.-C. Park, S. Im, D. K. Hwang, *ACS Nano* **2021**, 15, 17917.

[105] B. Zhang, Z. Ao, X. Lan, J. Zhong, F. Zhang, S. Zhang, R. Yang, L. Wang, P. Chen, G. Wang, *Nano Letters* **2024**.

[106] G. Long, R. Sabatini, M. I. Saidaminov, G. Lakhwani, A. Rasmita, X. Liu, E. H. Sargent, W. Gao, *Nature Reviews Materials* **2020**, 5, 423.

[107] J. Crassous, M. J. Fuchter, D. E. Freedman, N. A. Kotov, J. Moon, M. C. Beard, S. Feldmann, *Nature Reviews Materials* **2023**, 8, 365.

[108] J. Wang, H. Lu, X. Pan, J. Xu, H. Liu, X. Liu, D. R. Khanal, M. F. Toney, M. C. Beard, Z. V. Vardeny, *ACS Nano* **2021**, 15, 588.

[109] P. J. Huang, K. Taniguchi, M. Shigefuji, T. Kobayashi, M. Matsubara, T. Sasagawa, H. Sato, H. Miyasaka, *Advanced Materials* **2021**, 33, 2008611.

[110] Z.-G. Yu, *The Journal of Physical Chemistry Letters* **2020**, 11, 8638.

[111]J. Ahn, S. Ma, J.-Y. Kim, J. Kyhm, W. Yang, J. A. Lim, N. A. Kotov, J. Moon, *Journal of the American Chemical Society* **2020**, 142, 4206.

[112] D. Giovanni, W. K. Chong, H. A. Dewi, K. Thirumal, I. Neogi, R. Ramesh, S. Mhaisalkar, N. Mathews, T. C. Sum, *Science Advances* **2016**, 2, e1600477.

[113] P. Spaeth, S. Adhikari, L. Le, T. Jollans, S. Pud, W. Albrecht, T. Bauer, M. Caldarola, L. Kuipers, M. Orrit, *Nano Letters* **2019**, 19, 8934.

[114] T.-L. Chen, A. Salij, K. A. Parrish, J. K. Rasch, F. Zinna, P. J. Brown, G. Pescitelli, F. Urraci, L. A. Aronica, A. Dhavamani, *Nature Communications* **2024**, 15, 3072.

[115] H. Lu, J. Wang, C. Xiao, X. Pan, X. Chen, R. Brunecky, J. J. Berry, K. Zhu, M. C. Beard, Z. V. Vardeny, *Science Advances* **2019**, 5, eaay0571.

[116] A. D. Dillon, M. J. Ghidiu, A. L. Krick, J. Griggs, S. J. May, Y. Gogotsi, M. W. Barsoum, A. T. Fafarman, *Advanced Functional Materials* **2016**, 26, 4162.

[117] S. Aftab, A. Abbas, M. Z. Iqbal, S. Hussain, F. Kabir, H. H. Hegazy, F. Xu, J. H. Kim, B. S. Goud, *Materials Today Energy* **2023**, 36, 101366.

[118] C. Hou, H. Yu, C. Huang, *Journal of Materials Chemistry C* **2019**, 7, 11549.

[119] H. Chen, L. Gao, O. A. Al-Hartomy, F. Zhang, A. Al-Ghamdi, J. Guo, Y. Song, Z. Wang, H. Algarni, C. Wang, S. Wageh, S. Xu, H. Zhang, *Nanoscale* **2021**, 13, 15891.

[120] Q. Zhang, L. Yan, M. Yang, G. Wu, M. Hu, J. Li, K. Yuan, X. Yang, *The Journal of Physical Chemistry C* **2020**, 124, 6441.

[121] L. Li, J. Wang, L. Kang, W. Liu, L. Yu, B. Zheng, M. L. Brongersma, D. H. Werner, S. Lan, Y. Shi, Y. Xu, X. Wang, *ACS Nano* **2020**, 14, 16634.

[122] Q. Chen, Z. Ding, L. Zhang, D. Wang, C. Geng, Y. Feng, J. Zhang, M. Ren, S. Li, S. M. Qaid, *Advanced Materials* **2024**, 2400493.

[123] C. Fang, J. Li, B. Zhou, D. Li, *Nano Letters* **2021**, 21, 6156.

[124] X. Liang, Y. Luo, Y. Pei, M. Wang, C. Liu, *Nature Electronics* **2022**, 5, 859.

[125] J. Moon, W. Ma, J. H. Shin, F. Cai, C. Du, S. H. Lee, W. D. Lu, *Nature Electronics* **2019**, 2, 480.

[126] K. Liu, T. Zhang, B. Dang, L. Bao, L. Xu, C. Cheng, Z. Yang, R. Huang, Y. Yang, *Nature Electronics* **2022**, 5, 761.

[127] S.-H. Yang, R. Naaman, Y. Paltiel, S. S. P. Parkin, *Nature Reviews Physics* **2021**, 3, 328.

[128] B. P. Bloom, Y. Paltiel, R. Naaman, D. H. Waldeck, *Chemical Reviews* **2024**, 124, 1950.

[129] T. Liu, P. S. Weiss, *ACS Nano* **2023**, 17, 19502.

[130] R. Naaman, Y. Paltiel, D. H. Waldeck, *Nature Reviews Chemistry* **2019**, 3, 250.

[131] Z. Xu, X. Xue, Z. Zhang, B. Mao, R. Li, W. Gao, H. Guo, H. Lu, H. Li, J. Wang, *ACS Nano* **2025**, 19, 12033.

[132] X. Li, C. Wan, R. Zhang, M. Zhao, S. Xiong, D. Kong, X. Luo, B. He, S. Liu, J. Xia, G. Yu, X. Han, *Nano Letters* **2024**, 24, 5420.

[133] Y. Adhikari, T. Liu, H. Wang, Z. Hua, H. Liu, E. Lochner, P. Schlottmann, B. Yan, J. Zhao, P. Xiong, *Nature Communications* **2023**, 14, 5163.

[134] J. T. Gish, D. Lebedev, T. W. Song, V. K. Sangwan, M. C. Hersam, *Nature Electronics* **2024**, 7, 336.

[135] F. Evers, A. Aharony, N. Bar-Gill, O. Entin-Wohlman, P. Hedegård, O. Hod, P. Jelinek, G. Kamieniarz, M. Lemeshko, K. Michaeli, V. Mujica, R. Naaman, Y. Paltiel, S. Refaely-Abramson, O. Tal, J. Thijssen, M. Thoss, J. M. van Ruitenbeek, L. Venkataraman, D. H. Waldeck, B. Yan, L. Kronik, *Advanced Materials* **2022**, 34, 2106629.

[136] R. Naaman, D. H. Waldeck, *The Journal of Physical Chemistry Letters* **2012**, 3, 2178.

[137] M.-G. Kang, I.-K. Hwang, H.-C. Kyung, J. Kang, D. Han, S. Lee, J. Kwon, K.-J. Lee, J. Yeom, B.-G. Park, *APL Materials* **2024**, 12.

[138] J. Xiao, H. Zheng, R. Wang, Y. Wang, S. Hou, *Journal of Materials Chemistry A* **2022**, 10, 19367.

[139] H. Lu, C. Xiao, R. Song, T. Li, A. E. Maughan, A. Levin, R. Brunecky, J. J. Berry, D. B. Mitzi, V. Blum, M. C. Beard, *Journal of the American Chemical Society* **2020**, 142, 13030.

[140] R. Gutierrez, E. Díaz, R. Naaman, G. Cuniberti, *Physical Review B* **2012**, 85, 081404.

[141] E. Medina, F. López, M. A. Ratner, V. Mujica, *Europhysics Letters* **2012**, 99, 17006.